Bucknell University
Bucknell Digital Commons

Faculty Journal Articles

Faculty Scholarship

2010

Discovery of a young L dwarf binary, SDSS224953.47+004404.6AB

Katelyn N. Allers
Bucknell University, kna003@bucknell.edu

Michael C. Liu

Trent J. Dupuy

Michael C. Cushing

Follow this and additional works at: https://digitalcommons.bucknell.edu/fac_journ

Part of the Physics Commons

Infrared Spectral Energy Distributions of Seyfert Galaxies: Spitzer Space Telescope Observations of the 12 μm Sample of Active Galaxies

J. F. Gallimore[1,2], A. Yzaguirre[1,3], J. Jakoboski[1,4], M. J. Stevenosky[1,5], D. J. Axon[6,7], S. A. Baum[8], C. L. Buchanan[9], M. Elitzur[10], M. Elvis[11], C. P. O'Dea[6], A. Robinson[6]

draft:January 27, 2010

ABSTRACT

The mid-infrared spectral energy distributions (SEDs) of 83 active galaxies, mostly Seyfert galaxies, selected from the extended 12 μm sample are presented. The data were collected using all three instruments, IRAC, IRS, and MIPS, aboard the *Spitzer Space Telescope*. The IRS data were obtained in spectral mapping mode, and the photometric data from IRAC and IRS were extracted from matched, $20''$ diameter circular apertures. The MIPS data were obtained in SED mode, providing very low resolution spectroscopy ($R \sim 20$) between ~ 55 and 90 μm in a larger, $20'' \times 30''$ synthetic aperture. We further present the data from a spectral decomposition of the SEDs, including equivalent widths and fluxes of key emission lines; silicate 10 μm and 18 μm emission and absorption strengths; IRAC magnitudes; and mid-far infrared spectral indices. Finally, we examine the SEDs averaged within optical classifications of activity. We find that the infrared SEDs of Seyfert 1s and Seyfert 2s with hidden broad line regions (HBLR, as revealed by spectropolarimetry or other technique) are qualitatively similar, except that Seyfert 1s show silicate emission and HBLR Seyfert 2s show silicate absorption. The infrared SEDs of other classes within the 12 μm sample, including Seyfert 1.8-1.9, non-HBLR Seyfert 2 (not yet shown to hide a type 1 nucleus), LINER, and HII galaxies, appear

[1]Department of Physics and Astronomy, Bucknell University, Lewisburg, PA 17837

[2]Currently on leave at NRAO, 520 Edgemont Rd., Charlottesville, VA 22903

[3]Department of Physics, California State University, Fullerton, P.O. Box 6866, Fullerton, CA 92834-6866

[4]Jet Propulsion Laboratory, 4800 Oak Grove Drive, Pasadena, CA 91190

[5]Franklin Pierce Law Center, Two White Street, Concord, NH 03301

[6]Department of Physics, Rochester Institute of Technology, 84 Lomb Memorial Drive, Rochester, NY 14623

[7]School of Mathematical and Physical Sciences, University of Sussex, Falmer, Brighton, BN1 9QH, UK

[8]Chester F. Carlson Center for Imaging Science, Rochester Institute of Technology, 54 Lomb Memorial Drive, Rochester, NY 14623

[9]School of Physics, University of Melbourne, Parkville, Victoria, 3010 Australia

[10]Department of Physics and Astronomy, University of Kentucky, Lexington, KY 40506

[11]Harvard-Smithsonian Center for Astrophysics, 60 Garden Street, Cambridge, MA 02138

to be dominated by star-formation, as evidenced by blue IRAC colors, strong PAH emission, and strong far-infrared continuum emission, measured relative to mid-infrared continuum emission.

Subject headings: galaxies: active — galaxies: Seyfert — galaxies: spiral — infrared: galaxies

1. Introduction

Three components dominate the mid-infrared spectrum of an active galaxy (Genzel & Cesarsky 2000): (1) thermal radiation from a dusty, compact medium that surrounds the active nucleus (AGN) and can obscure direct sight-lines to it; (2) PAH features and thermal dust continuum associated with star-formation or perhaps a powerful starburst; and (3) line features arising from molecular, atomic, and ionic species.

The dusty medium surrounding the AGN is commonly referred to as "the dusty torus." Its presence is inferred for many AGNs based, for example, on spectropolarimetry (Antonucci & Miller 1985; Antonucci 1993; Urry & Padovani 1995; Smith et al. 2004), X-ray spectroscopy (Risaliti et al. 2007, 2002), and infrared aperture synthesis measurements (Jaffe et al. 2004; Tristram et al. 2007). Observations further indicate that the dusty medium must be axisymmetric, permitting low extinction sight-lines to type 1 AGNs, where the broad-line region (BLR) is apparent in total intensity (Stokes I) spectra (the "pole-on" view), but high-extinction sight-lines to type 2 AGNs, which show suppressed broad line emission and AGN continuum (the "edge-on" view).

Since the dusty torus re-radiates incident AGN continuum in the mid-infrared, its SED provides an indirect measure of the AGN luminosity (Nenkova et al. 2008b), important especially for heavily obscured AGNs where other indirect diagnostics may not be available. Mid-infrared fine-structure lines can also constrain the intrinsic shape of the AGN SED, because particular line ratios are sensitive to the shape of the SED but less sensitive to extinction compared to optical/UV lines of species with similar ionization energies (Alexander et al. 2000).

The torus SED depends on the geometry and clumpiness of the torus, among other properties (Nenkova et al. 2002, 2008b). For example, smooth, cylindrical tori produce very strong 10 μm silicate (Sil) features, whether in emission when viewed more nearly pole-on, or deep absorption when viewed edge-on (Pier & Krolik 1992). Clumpy tori, somewhat independent of the assumed geometry, instead produce much weaker Sil features, because inter-clump sight-lines can provide a view of hotter dust on the far side of the torus; our view of clumpy tori includes a mix of cold and hot clump surfaces that dilutes the Sil features (Nenkova et al. 2008b). Individual clumps are heated from outside and cannot produce the strong absorption that a centrally heated dust shell can have (Sirocky et al. 2008; Nenkova et al. 2008a; Levenson et al. 2007).

The mid-infrared SED is also an important diagnostic of star-formation. Young star clusters

embedded in GMCs are predicted to produce weaker PAH equivalent width in comparison to older clusters, owing to photodestruction and continuum dilution by hot dust grains (Efstathiou et al. 2000). In global models, PAH features are sensitive to the fractional luminosity of OB associations and the gas density of their surrounding ISM (Siebenmorgen & Krügel 2007). Since the dusty medium re-radiates incident stellar radiation, the mid-far infrared luminosity constrains the luminous contribution of star-formation.

The mid-infrared SED of active galaxies therefore contains diagnostics of the AGN, its surrounding dusty torus, and any surrounding star-formation. The described tracers can, in principle, be disentangled by spectral decomposition of the global SED (Farrah et al. 2003; Marshall et al. 2007). At the present, available infrared instruments, at least in their default mode of use, suffer from mismatched apertures leading to discontinuities in the observed SEDs or mismatched coverage of spectral lines that bias line ratios.

To remedy this problem of aperture matching, we have used the *Spitzer Space Telescope* to observe a sample of active galaxies, mostly Seyferts, in synthetically matched, $20''$ diameter apertures spanning $\lambda 3.6$-36 μm and a larger aperture, $\sim 20'' \times 30''$, covering $\lambda 55$-90 μm. These moderate to low resolution SEDs are well-suited for spectral decomposition, studies of the PAH and Sil features, as well as global constraints on the AGN and star-formation contributions to the luminosity.

The observations and data obtained for this survey are presented in this work. Section 2 describes the sample selection. Section 3 provides a detailed account of the observations and data reduction, with attention to artifact correction, synthetic aperture matching, and corrections for extended emission. Section 4 summarizes the extraction of spectral features using a modified version of the PAHFIT tool (Smith et al. 2007b) and measurements based on the line-subtracted SEDs. We conclude in Section 5 with a summary of the properties of the sample and avenues for future analysis.

2. Sample Selection

The sample, listed in Table 1, comprises a subset of the extended 12 μm sample of AGNs (Rush et al. 1993). This parent sample was defined by an IRAS detection at 12 μm, $F_{12}(\mathrm{IRAS}) > 0.22$ Jy, and color selection $F_{60}(\mathrm{IRAS}) > 0.5 F_{12}(\mathrm{IRAS})$ or $F_{100}(\mathrm{IRAS}) > F_{12}(\mathrm{IRAS})$ to remove stars but few galaxies. AGNs were identified based on prior (usually optical) classification. We restricted the sample to include (1) only those objects categorized by Rush et al. (1993) as Seyferts or LINERs, and (2) only those sources with $cz < 10,000$ km s^{-1}. Three sources were removed subsequent to observations owing either to pointing errors or saturation in the Spitzer observations: NGC 1068, M-3-34-64, and NGC 4922. Our sample ultimately includes 83 Seyfert and LINER nuclei.

The main advantage of this sample over other AGN catalogs is its large collection of published and archival multiwavelength observations (Rush et al. 1996; Hunt & Malkan 1999; Hunt et al. 1999; Thean et al. 2001, 2000; Gallimore et al. 2006; Spinoglio et al. 2002). In addition, there are

comparable numbers of Seyfert 1 (S1) and Seyfert 2 (S2) nuclei, and their redshift distributions are statistically indistinguishable (Thean et al. 2001, 2000).

The original survey paper of Rush et al. (1993) broadly assigned optical classifications of type 1 (broad-line AGN) and type 2 (narrow-line AGN), but Tran (2003) pointed out that, even given such coarse binning of activity type, there were many misclassifications. To aid in a more sophisticated comparison of infrared properties to optical classifications, we endeavored to collect updated and more precise classifications from the literature. The revised classifications are included in Table 1 and illustrated in Figure 1. We find that 20% (7 / 35) of the Rush et al. Type 1s are re-classified as hidden broad line region (HBLR) Seyfert 2s (S1h or S1i), LINER, or HII (star-forming galaxy), and 28% (13 / 46) of the Rush et al. Type 2s are re-classified as S1.n, LINER, or HII. Note that HBLRs have been sought in all but three of the 20 S2s in our survey: NGC 1125, E33-G2, and NGC 4968 (Tran 2003).

3.   Observations and Data Reduction

The sample galaxies were observed using all of the instruments of the *Spitzer Space Telescope* (Program ID 3269, Gallimore, P.I.): the four broadband channels (3.6 μm, 4.5 μm, 5.8 μm, and 8.0 μm) of the Infrared Array Camera (IRAC; Fazio et al. 2004); the low resolution gratings of the Infrared Spectrograph (IRS; Houck et al. 2004), operating in spectral mapping mode; and the Multiband Imaging Photometer for Spitzer (MIPS; Rieke et al. 2004), operating in SED mode. The resulting SEDs are provided in Figure 2.

Several sample galaxies were observed as part of other *Spitzer* programs that made use of different observing strategies; for example, in some cases only single-pointing ("Staring Mode") IRS spectra are available. We summarize the observations and data reduction techniques both for our observing program and archival *Spitzer* data.

3.1.   Spitzer IRAC Observations

IRAC observations were centered on the NED coordinates of the sample galaxies based on catalog names listed in Rush et al. (1993). A beamsplitter and supporting optics centers the target on two detectors simultaneously (Fazio et al. 2004), either at 3.6 and 5.8 μm or 4.5 and 8.0 μm, and so each observation consisted of two pointings at a common orientation of the focal plane relative to sky. These observations were taken as snapshots with no attempt to mosaic or dither. To guard against saturation, we used the high-dynamic range (HDR) mode which provides 0.6 s and 12 s integrations at each pointing.

The data were initially processed and calibrated by the IRAC basic calibration data (BCD) pipeline, version S14.0. The pipeline performs basic processing tasks, including bias and dark

current subtraction; response linearization for pixels near saturation; flat-fielding based on observations of high-zodiacal background regions; saturation and cosmic-ray flagging, the latter indicated by signal detections more compact than the PSF; and finally flux calibration based on observations of standard stars[1]. The nominal photometric stability for compact sources is better than 3% in all detectors (Reach et al. 2005). Corrections for extended sources[2] are accurate to $\sim 10\%$, but the contribution of extended emission and the resulting correction is small for most of the sample galaxies. Color-corrections are typically much greater, especially in the 8.0 μm channel where in-band PAH emission can result in factors of two or greater corrections.

The data were further processed for remaining artifacts, including cosmic-rays and detector artifacts not corrected by the BCD pipeline. The steps performed for artifact removal and photometric extraction are detailed below in Sections 3.1.1–3.1.4. Figure 3 illustrates the effect of our artifact removal techniques.

The IRAC photometry is listed in Table 2. Detailed below, the photometry is presented in the IRAC magnitude system with zero-point flux densities 280.9, 179.7, 115.0, and 64.13 Jy for the 3.6, 4.5, 5.8, and 8.0 μm channels, respectively (Reach et al. 2005). The photometry includes corrections for extended emission and color-corrections.

3.1.1. Cosmic-ray and bandwidth-effect mitigation

All of the images were affected to varying degrees by cosmic-ray and solar proton hits. Moreover, 5.8 and 8.0 μm images near saturation suffered from the bandwidth effect, which manifests as a row-wise trail of fading source images repeating every four pixels from the affected source. These multiple images do not conserve flux but artificially add signal to the sources; for our purposes, these bandwidth effect artifacts behave like cosmic ray hits near our target galaxies.

The BCD pipeline attempts to identify cosmic-ray hits by locating detections that are narrower than the PSF. Extended cosmic ray tracks are however missed by this procedure. The v. S14.0 BCD pipeline further has no means of mitigating the bandwidth effect.

We corrected these artifacts in three, post-BCD steps. Firstly, we generated difference maps between the long and short exposure images. Difference signal that exceeded 5σ on the long exposure images was flagged as an artifact, and these artifacts were replaced with signal from the short exposure image. The matching mask and uncertainty images were updated accordingly. This technique was particularly successful at removing bandwidth artifacts with little image degradation; the affected image regions are at relatively high signal-to-noise on the short exposure images.

We next applied van Dokkum's (2001) algorithm to flag cosmic rays not picked up on difference

---

[1]Details are provided in the IRAC Data Handbook, available at http://ssc.spitzer.caltech.edu/irac/dh/.

[2]http://ssc.spitzer.caltech.edu/irac/calib

images. Images are convolved with a Laplacian filter, which enhances sharp edges on image features and effectively identifies cosmic ray tracks. The IRAC point response function (PRF) is however undersampled in all four detectors, and real, compact sources such as field stars or the AGN appear as false positives. These false positives can be filtered by measuring the asymmetry of the detected source, parameter f_{lim} in van Dokkum's notation. Cosmic ray hits tend to be more asymmetric than the PRF, corresponding to a larger value of f_{lim}. Using a few sample images and trial-and-error, we determined lower threshold values for f_{lim} that flag obvious cosmic rays but pass field stars and galaxy images; specifically, we found $f_{lim} = 8$ worked well for the 4.5, 5.8, and 8.0 μm images, and $f_{lim} = 10$ for the 3.6 μm images.

Finally, the few remaining cosmic rays were flagged interactively by inspection of four-color images. Residual cosmic rays appear as color-saturated pixels in this representation and so were easily identified, flagged, and replaced by bilinear interpolation of neighboring pixels.

3.1.2. Bias artifacts

Residual bias artifacts affect the pipeline-processed data. Software is currently available at the Spitzer Science Center to mitigate these artifacts where the image comprises mainly compact sources, but the algorithm breaks down in the presence of extended or diffuse emission. The host galaxy is detected for many of the sample AGNs, and so we had to develop new techniques to eliminate these bias artifacts.

The 3.6 and 4.5 μm images show the effects of column pull-down and multiplexer bleed ("muxbleed"). Column pull-down is evident as a depressed bias level along columns that run through pixels near saturation. The bias adjustment is nearly constant along a column, but there may be slightly different bias offsets above and below saturated pixels.

One approach is to evaluate the bias depression in source-free regions, but, for some sources, the presence of extended emission over a majority fraction of the array reduces or eliminates valid background regions. We suppressed the diffuse emission by performing row-wise median filtering across pull-down columns and used the median difference to determine the bias correction.

Muxbleed also affects rows containing pixels near saturation, most evident as a row pull-up, but also impacting the bias level on neighboring rows. The images are read as four separate readout channels that are interlaced every four columns. The bias on each readout channel is affected differently, resulting in a vertical pinstripe pattern over some region of the array near saturated pixels.

To mitigate the muxbleed artifact in the presence of extended emission, we first median-filtered the image using an 8×8 kernel to smooth out the pinstripe pattern over two readout cycles, subtracted the median-filtered image to remove diffuse emission, and generated residual images of each readout channel. Muxbleed appears on each channel readout image as decaying, horizontal

stripes along rows containing pixels near saturation with surrounding bands of weaker, constant bias offset. We determined a final muxbleed model by fitting the brighter muxbleed stripes with a cubic polynomial and determining the median DC-level offset in the surrounding bands.

The 5.8 μm images were affected by residual dark current, appearing as a slowly varying surface brightness gradient of the background. This "first frame" artifact results from the sensitivity of the dark current to properties of the previous observation and the time elapsed since that observation. To remove this dark current gradient, we first masked bright stars and diffuse emission from galaxies and then fit a bilinear surface brightness model to the background.

Several 5.8 and 8.0 μm images were also affected by banding, which is a decaying signal along rows or columns containing saturated pixels. These bands were reduced by fitting separate row-wise and column-wise polynomials to the surface brightness of off-source regions of the array.

3.1.3. Saturation and Distortion

Final corrections were performed using custom IDL scripts and the *MOPEX* software package[3] (Makovoz & Khan 2005; Makovoz et al. 2006). The short exposure images were used to replace saturated pixels on the long-exposure images. The images were then corrected for distortion and registered to a $1''.22 \times 1''.22$ grid. The resulting data products are the science image, calibrated in surface brightness units MJy sr^{-1}; an uncertainty image based on the propagation of statistical uncertainties through the pipeline and post-BCD processing, but which does not include systematic uncertainties associated with calibration; and a coverage image, which, for these snapshot exposures, marks good pixels as "1," bad pixels (i.e., known bad pixels or cosmic ray hits) as "0," and intermediate values indicating that good and bad pixels were used in the distortion correction for that pixel.

3.1.4. Photometric extraction

We extracted flux density measurements using a synthetic, $20''$ diameter circular aperture centered on the brightest infrared source associated with the active galaxy. The exception is NGC 1097, which has an off-nucleus star-forming region that is brighter than the central point source; in that case, the aperture was centered on the central point source. To determine the point-source contribution to the aperture, each image was convolved with a 2-D, rotationally symmetric Ricker wavelet (González-Nuevo et al. 2006). The width of the central peak of the wavelet was tuned to match the width of the nominal IRAC PRF, effectively subtracting extended emission and enhancing point sources. We used field stars to calibrate the point source response of the

---

[3]http://ssc.spitzer.caltech.edu/postbcd/mopex.html

wavelet-convolved image; this calibration includes a correction for aperture losses. We next applied extended source corrections[4] to the residual signal (total − point source).

Finally, the resulting photometry was color-corrected following the prescription described in the IRAC Data Handbook. The uncorrected calibration provides a flux density measurement at a nominal wavelength assuming a nominal spectral shape $\nu F_\nu = $ constant over the broadband response. The color-correction adjusts the calibration based on the true shape of the spectrum. The result is the true flux density at a nominal wavelength rather than a broadband average; for example, the color-corrected flux reported for the 8 μm camera will be closer to peak of the 7.7 μm PAH feature plus any underlying continuum at that wavelength rather than bandpass-weighted average. For reference, the nominal wavelengths for the IRAC cameras are 3.550, 4.493, 5.731, and 7.872 μm.

Color-correction involves integrating the infrared spectrum weighted by the IRAC filter bandpasses. To perform this integration, we used our IRS spectra (Section 3.3, below) with extrapolation to shorter wavelengths assuming a power law slope matching the observed, uncorrected 3.6 μm flux density. Note that this color-correction technique does not force a match between the IRS and IRAC photometry; the flux scale of the spectrum is normalized so that only the shape of the IRS spectrum influences the color correction. Photometric corrections for extended sources are not accurately known for the IRS spectra, and so the accuracy of the IRS spectral extractions precluded separating the color corrections for extended and point source contributions for a given source; rather, the color correction was determined based on the integrated signal in the aperture.

3.2. Archival Spitzer IRAC Observations

IRAC observations of 16 sample galaxies were obtained through public release to the *Spitzer* archive. Data processing largely followed the techniques described above for our observations, except that, where our observations comprise snapshots, the archival observations all employed dithering or mosaicking techniques. The archival data were initially mosaicked using standard procedures with *MOPEX*, including background matching based on overlaps.

Artifacts, particularly banding, seriously affected the matching of mosaic overlap regions and so we developed a modified mosaicking procedure building on the algorithm of Regan & Gruendl (1995). We modified their least-squares approach to employ least absolute deviations as a more robust measure of the quality of overlap matching, and we further masked bright source and artifact regions prior to overlap matching. The final images were assembled using a median stack of astrometrically aligned images, background subtracted, and finally sub-imaged to roughly 5′ square to match our survey observations.

---

[4]http://ssc.spitzer.caltech.edu/irac/calib/

Residual bias artifacts were removed by computing column or row biases where sufficient background was available for bias determination. Cosmic rays were largely mitigated by the median stack, but residual bad pixels were identified and flagged interactively, as described in Section 3.1.1.

3.3. Spitzer IRS Spectral Mapping

We observed the sample galaxies using the *Spitzer* IRS in spectral mapping mode and using the Short-Low (SL) and Long-Low (LL) modules. The modules cover a wavelength range of ~ 5 – 36 μm with resolution $R = \lambda/\Delta\lambda$ ranging from 64 to 128. The integration times were 6 seconds per slit pointing.

The spectral maps were constructed to span $> 20''$ in the cross-slit direction and centered on the target source. The observations were stepped perpendicular to the slit by half slit-width spacings. For the SL data, the mapping involved 13 observations stepped by $1{.}''8$ perpendicular to the slit, and, for the LL data, 5 observations stepped by $5{.}''25$ perpendicular to the slit. The resulting spectral cubes span roughly $25{.}''2 \times 54{.}''6 \times (5.3 – 14.2 \ \mu\mathrm{m})$ for the SL data and $29{.}''1 \times 151'' \times (14.2 – 36 \ \mu\mathrm{m})$ for the LL data.

The raw data were processed through the *Spitzer* BCD pipeline, version S15.3.0. The pipeline handled primary processing tasks including identification of saturated pixels; detection of cosmic ray hits; correction for "droop," in which charge stored in an individual pixel is affected by the total flux received by the detector array; dark current subtraction; and flat-fielding and response linearization. Details are provided in the IRS Data Handbook[5].

Sky subtraction used off-source orders. In SL and LL observations, the source is centered in the first or second order separately, with the "off-order" observing the sky at a position offset parallel to the slit: $79''$ away for SL and $192''$ away for LL. Sky frames were constructed using median combinations of the off-source data and subtracted from the on-source data of matching order. No detectable contamination of the sky frame appeared in our observations based on inspection of the sky frame data. In addition, a portion of the first order slit spectrum appears on the second order observation and is used as an additional check of spectral features that appear near the first / second order spectral boundary.

Data cubes were constructed by first registering the individual, single-slit spectra onto a uniform grid (slit-position vs. wavelength). The IRS slits do not align with the detector grid, and the detector pixels undersample the spatial resolution. Interpolating the undersampled slit onto a uniform grid produces resampling noise (Allington-Smith et al. 1989), which significantly impacts the spectra of unresolved sources. We instead used the pixel re-gridding algorithm described by Smith et al. (2007a) that minimizes resampling noise. Pixels from the original image are effectively

---

[5]http://ssc.spitzer.caltech.edu/mips/dh

placed atop the new, registered pixel grid. Uniform surface brightness is assumed across the original pixel, and that original signal is weighted and distributed based on the fractional overlap with pixels on the new grid. After registering the single-slit frames, the data were re-gridded by bilinear interpolation, one wavelength plane at a time, into the final data cube. Flux uncertainty images were similarly processed, with modifications to accommodate variance propagation, to produce an uncertainty cube.

The spectra were extracted from synthetic, $20''$ diameter circular apertures centered on the brightest, compact IR source nearest the target coordinates. Fractional pixels at the edge of the aperture were accounted for by assuming uniform surface brightness across the pixel and weighting by the area of intersection between the pixel and aperture mask.

The cube-extracted spectra were optimally weighted based on a three-dimensional modification of Horne's (1986) two-dimensional slit extraction algorithm. Successful application of this algorithm requires estimation of spatial profiles $P_{x\lambda}$, the probability that a detected photon falls in a given pixel x rather than some other pixel on the spectral map at wavelength λ. Optimal extraction requires that the fractional uncertainty of the estimator for $P_{x\lambda}$ is less than the fractional uncertainty of original spectral image. Generation of $P_{x\lambda}$ therefore requires some smoothing along the wavelength axis. To help preserve real variations of $P_{x\lambda}$ with wavelength, we employed Savitzky-Golay (1964) polynomial smoothing. In this smoothing scheme, $P_{x\lambda}$ is calculated by a polynomial fit to the spectrum at pixel x over the fitting window $\delta\lambda$ either centered on λ or limited by the ends of the spectrum. We performed trial-and-error smoothing experiments on CGCG381-051, which shows relatively weak continuum at short wavelengths but high eqw PAH features, to decide on the polynomial order and window smoothing parameters; ultimately we selected quadratic polynomials and 5-pixel smoothing windows to balance improved signal-to-noise and the tracking of real variations of $P_{x\lambda}$ with wavelength.

The effect of optimal extraction is illustrated in Figures 4 and 5, which compare the optimally-extracted and non-weighted extraction of the IRS SL spectrum of NGC 3079 and F01475-0740, and Table 3, which compares the measurements derived from these extractions (see Section 4.1 for a description of the measurement technique). NGC 3079 presents a challenging case because it is edge-on and shows bright, extended PAH emission. The spatial profile is therefore a complex function of wavelength, and coarse smoothing in the wavelength direction could potentially affect the measurement of the PAH fluxes and equivalent widths. We find however that the fractional difference between the optimally-weighted spectrum and the unweighted spectrum is typically only a few %, comparable to the statistical uncertainties in the unweighted spectrum. Furthermore, the measured fluxes and equivalent widths agree to within the measurement uncertainties; in fact, the measurement uncertainties are dominated by the systematics of the measurement technique.

Compared to NGC 3079, F01475-0740 is a compact source at relatively low signal-to-noise. Figure 5 clearly illustrates the advantage of optimum weighting. The continuum shape and PAH spectral features are preserved, but the formal statistical uncertainties are reduced by factor of

2–3 over the SL spectral range. Again, the fluxes and equivalent widths of lines agree to within the measurement uncertainties, but the optimally weighted spectrum produced signficant ($> 3\sigma$) detections of PAH 6.2 μm, Ne V 14.3 μm, and S III 18.7 μm that are too faint for the unweighted spectrum.

Fringing at the 5% – 10% level was apparent in the LL observations, particularly those of sample objects with a strong point source contribution. The spectra undersample the fringing, and so the fringe pattern could not be removed using a conventional filtering in Fourier space. We employed instead the technique described by Kester et al. (2003), which involves fitting sinusoids in wavenumber to line-free sections of the spectrum. Successive fringe components are added to the model until the next model fringe amplitude falls below the noise level of the spectrum. The effect of this technique is illustrated in Figure 6.

The flux scale was calibrated against archival staring and spectral mapping observations of the stars HR7341 (SL) and HR6606 (LL). The staring mode spectra were extracted using SPICE[6], and the spectral mapping observations were processed into cubes as described above for our sample galaxies. The flux calibration curve was determined by the ratio of the flux-calibrated staring mode spectra to the uncalibrated, cube-extracted spectra and smoothed by a polynomial fit.

No correction was produced for resolved, extended emission. The flux calibration includes an aperture loss correction factor appropriate for compact sources, but extended sources do not suffer as much aperture loss. Therefore, wavelength bands containing extended emission relative to the PRF will be calibrated systematically high. Discussed below in Section 3.6, the systematic error introduced is of order 10%, particularly near the 8 μm PAH features.

We note that these IRS observations have been independently and differently processed and recently presented in Wu et al. (2009). The main differences in data processing are: (1) Wu et al. used the CUBISM tool and its calibrations for spectral cube construction (Smith et al. 2007a); (2) it is not clear that Wu et al. extracted the spectra optimally; (3) a rectangular aperture, which covers a similar solid angle to our extraction aperture, was commonly used ($20\rlap{.}''4 \times 15\rlap{.}''3$; larger for SINGS galaxies); (4) there appears to have been no attempt to de-fringe the long wavelength (LL) data; (5) for an unknown number of sources, Wu et al. had to scale the SL data to match up with the flux calibration of the LL data. We address these differences in turn, excepting (3), the minor difference of extraction aperture geometry.

We found that (1) CUBISM forced the data onto a new grid in which the original pointing center was shifted, commonly resulting in nuclei that were centered between pixels rather than on a pixel. This shift apparently introduced a systematic error in the resampling of the surface brightness, because we noticed artifacts and a few percent reduced signal in the spectrum extracted from cubes produced by CUBISM. Our cubing technique was designed to require minimal resampling of the observational grid and mitigated these artifacts.

---

[6]http://ssc.spitzer.caltech.edu/postbcd/spice.html.

We also found that (2) non-optimal extractions decreased the signal-to-noise of the extracted spectra of fainter sources by factors of $\sim 50\%$ or more (see Figure 5 and the discussion above). Although it varies source to source, (4) fringing can produce $\sim 10\%$ artifacts between 14 and 36 μm (cf. their extraction of MRK 1239 and M-6-30-15, among others). Finally, (5) we did not need to apply any additional scaling to the spectra extracted from SL cubes; rather our calibrations of the SL module show excellent agreement with both the IRAC measurements and LL measurements, even though the calibrations for each respective *Spitzer* module were based on different calibration stars; this result suggests that the calibration against spectrally mapped stars, as presented here, was more robust for calibration and systematic corrections, accepting the $\sim 10\%$ calibration uncertainty for sources dominated by extended emission.

3.4. Archival IRS Data

Archival data of our sample galaxies, such as obtained by the SINGS collaboration, were processed in the same manner as for our program data. Spectral mapping data were available in LL for all sources, but there are however a few sources for which only SL staring mode observations are available: NGC 526A, NGC 4941, NGC 3227, IC 5063, NGC 7172, and NGC 7314. The staring mode spectra were extracted using SPICE and subjectively scaled to achieve the best match to align with LL measurements and, where possible, IRAC 5.8 and 8.0 μm measurements. Not surprisingly, there result disagreements between the IRAC measurements and scaled, IRS staring observations owing to the contribution of the host galaxy in the $20''$ aperture.

3.5. Spitzer MIPS-SED Observations

The sample galaxies were observed using the 70 μm low-resolution spectrometer (SED mode) of the MIPS instrument. The spectrometer provides spectral resolution $R \sim 15$–25 between $\lambda 55$ and 95 μm. The slit dimensions are $20'' \times 120''$.

Each observation consisted of three pairs of on-source and off-source measurements, where the off-position was located $1' - 3'$ from the on-source position. Integration times were 3 or 10 seconds depending on the IRAS 60 μm flux density of the source. The observations include measurements of built-in calibration light sources, called stimulators, for flux calibration.

We used post-BCD products of the S14.4.0 pipeline; the pipeline processing includes flux calibration, background subtraction, co-addition of the on-source pointings, and uncertainty images. Details are provided in the MIPS data handbook [7].

The MIPS spectra were extracted by summing across a $29''$-wide synthetic aperture centered

---

[7]http://ssc.spitzer.caltech.edu/mips/dh

on the target source (three-column extraction). The spectra were further corrected for aperture losses assuming a point source model; the present extractions include no corrections for spatially extended emission. The photometric accuracy is expected to be 10% for compact sources and $\sim 15\%$ for extended sources (Lu et al. 2008).

Note that the MIPS aperture covers a solid angle $\sim 1.8\times$ larger than the IRAC and IRS apertures. Modeling SEDs of sources with extended $(> 20'')$ far-infrared emission will therefore require an (unknown) aperture correction that is potentially much greater than the reported calibration uncertainty. Candidates for MIPS aperture corrections will show a jump in the MIPS flux relative to a suitable extrapolation of the IRS spectrum, although a real spectral peak in the 40–50 μm range might similarly result in an observed MIPS SED that appears too blue even in the absence of aperture effects.

3.6. Comparison of IRS and IRAC Photometry

The IRS spectra overlap with the 5.8 and 8.0 μm IRAC channels. To compare the relative spectrophotometry, we interpolated the IRS spectra to find the flux densities at the effective wavelengths of the color-corrected IRAC data, 5.731 μm and 7.872 μm, respectively. The average relative difference of the overlapping flux densities, $F_\nu(\mathrm{IRS})/F_\nu(\mathrm{IRAC}) - 1$, are $4 \pm 1\%$ at 5.8 μm and $6 \pm 1\%$ at 8.0 μm. The frequency distributions are shown in Figure 7. For comparison, the average standard scores, $(F_\nu[\mathrm{IRS}] - F_\nu[\mathrm{IRAC}])/\sigma$, are 0.00 ± 0.03 and 0.18 ± 0.05.

These results indicate that the IRS flux densities are, on average, systematically higher than the IRAC measurements by a few percent. However, the excess at 5.8 μm is dominated by statistical uncertainties, as the average standard score is consistent with zero.

Strong, extended PAH emission however contributes significantly to the 8.0 μm IRAC channel. This spectral feature is difficult to color-correct accurately owing to numerical integration errors that arise at sharp spectral features. In addition, PAH emission is often spatially resolved in this sample, and the present IRS calibration includes no correction for extended emission. The systematic offset of 6% may result from the overcorrection of aperture losses for extended PAH sources. The IRAC photometry of extended sources is moreover accurate to only $\sim 10\%$.

Figure 8 shows the 8 μm IRS / IRAC flux ratio as a function of the fractional contribution of the central point source to the 20$''$ nuclear aperture. The fainter sources provide appreciable scatter, but the brighter sources reveal a trend in which point-source dominated objects show better agreement, but more extended objects present $\sim 10\%$ IRS excesses. This trend supports the interpretation that residual extended source calibration uncertainties are the primary cause for the IRS – IRAC discrepancies at 8 μm.

4. Analysis

4.1. Spectrum Decomposition

In addition to continuum radiation from dust grains and associated Sil emission and absorption bands, the infrared spectrum of Seyfert galaxies includes diagnostics such as fine structure lines tracing a range of ionization states, H_2 lines, and PAH emission. We used the spectrum fitting tool PAHFIT (Smith et al. 2007b), which is tailored to low resolution IRS spectroscopy. The fits to the SEDs of NGC 4151 and NGC 7213 are provided in Figure 9 as examples of the decomposition. The results are summarized in the following tables: integrated PAH fluxes are given in Table 4; PAH equivalent widths (EQWs) in Table 5; H_2 line fluxes (mostly upper limits) in Table 6 and EQWs in Table 7; ionic fine structure line fluxes in Table 8, and their EQWs in Table 9. The line measurements are not corrected for model extinction, but for completeness we list the best-fit model dust opacity (normalized to 10 μm) in Table 10.

As provided, PAHFIT is best suited for nearly normal or star-forming galaxies; its model includes thermal continuum radiation from dust grains, PAH features, fine-structure lines from lower ionization state species, H_2, and Sil absorption, whether by assumed mixed or foreground screen extinction. We added two components to the PAHFIT model to fit the Seyfert SEDs: (1) fine-structure lines from high ionization states, such as [Ne V] and [Ne VI]; and (2), to fit silicate emission features, a simple model for warm dust clouds that are optically thin at infrared wavelengths.

By default, PAHFIT models extinction based on the dust opacity law of Kemper et al. (2004). Sirocky et al. (2008) found that the cold dust model of Ossenkopf et al. (1992) better matches the high 18 μm Sil / 10 μm Sil absorption found in active ultraluminous infrared galaxies. From inspection, the present spectra similarly show relatively strong 18 μm features, whether in emission or absorption, and so we further modifed PAHFIT to use the cold dust model of Ossenkopf et al. (1992).

The thin, warm dust model assumes clouds with simple, slab geometry and opacity at 10 μm, $\tau_{10} < 1$. These warm clouds are further assumed to be partially covered by cold, absorbing dust clouds. The model spectrum is then,

$$F_\nu = (1 - C_f) B_\nu(T_W) \left(1 - e^{-\tau_W(\nu)}\right) + C_f B_\nu(T_W) \left(1 - e^{-\tau_W(\nu)}\right) e^{-\tau_C(\nu)}, \qquad (1)$$

where C_f is the covering fraction of cold, foreground clouds, modeled independent of the galaxy extinction; τ_W is the opacity through the warm clouds; τ_C is the opacity through the cold, foreground clouds, and $B_\nu(T_w)$ is the source function, for which we adopt a scaled Planck spectrum at (fitted) temperature T_W for simplicity. Note that the cold dust opacities described by Eq. 1 are taken to be independent of the global PAHFIT dust opacity model; the opacity values listed in Table 10 are determined by the global dust opacity fit. The intention of including this additional model component is to provide a realistic continuum baseline for emission line fits and Sil strength

determination rather than an interpretable, radiative transfer model, and details of the opacity law or more realistic source functions are beyond the scope of the present spectral decomposition.

We further modified PAHFIT better to accommodate the IRAC broadband and MIPS-SED measurements. Both instruments provide much lower sampling density in wavelength than IRS data, and consequently they receive lower weight in the χ^2 minimization procedure. We therefore employed the sampling weight correction described by Marshall et al. (2007), which effectively re-weights individual data points based on the sampling density local to that data point; regions of low sampling density receive increased weight. The weighting is normalized so that each data point carries, on average, unity sampling weight. We also introduced as a fitted parameter an aperture correction factor for the MIPS-SED wavelength range that boosts the model SED by a factor up to 1.81, which is the areal aperture ratio of the MIPS-SED extraction to the nominal $20''$ diameter extraction aperture. Table 10 includes the best-fit aperture corrections.

There are a few caveats to the results of this decomposition. These low spectral resolution data are not best suited for measuring line fluxes, particularly in spectrally crowded regions. PAHFIT takes a conservative approach, severely restricting the centroid wavelengths and widths of the fitted lines; for example, the fine-structure lines are assumed to be unresolved and their widths are fixed at the instrumental resolution. Even so, the fine-structure lines near 35 μm are crowded, and furthermore the IRS measurements are very noisy at that region of the spectrum, with sensitivity $\sim 10\times$ poorer than at 25 μm, depending on background ([http://ssc.spitzer.caltech.edu/documents/som/]Spitzer Observer's Manual). These limitations are reflected in the uncertainties and upper limits reported in Tables 4–9.

Extracted line fluxes were however affected by occasional, residually poor fits to the local continuum or PAH features. For example, if the PAHFIT model placed the continuum too low locally to an emission line, PAHFIT would grow the emission line to meet the data and therefore produce a line flux greater than observed. Similarly, the PAHFIT model might produce a local continuum that is too high and the line flux is reported too low. A good illustration of this problem is the too-high continuum model surrounding the [Ne V] $\lambda 14.3$ μm line of NGC 4151 (Figure 9). To compensate for locally poor continuum models, the mean and rms of the model-subtracted spectrum was evaluated in spectral regions surrounding each line. Each fitted line peak was accordingly adjusted by subtracting the local, mean residual continuum. Line fluxes were similarly adjusted; line widths are unaffected as they were held fixed to the instrumental resolution during the fit.

There is a weak PAH feature near 14.3 μm that potentially contaminates the [Ne V] $\lambda 14.3$ μm fine structure line (Sturm et al. 2000). Deblending these features uses the fact that the PAH feature is somewhat broader (FWHM ~ 0.4 μm) than the unresolved (FWHM < 0.1 μm) [Ne V] line (Smith et al. 2007b). In the worst-case scenario, the code may fail to fit a weak but present PAH 14.3 feature resulting in an artificially enhanced [Ne V] line strength. This effect is at least partially ameliorated by the residuals analysis and is reflected in the large uncertainties of Table 8. The [Ne V] 14 /

24 ratio provides however a good check for contamination. This ratio is a density diagnostic with lower limit ~ 0.9 (e.g., Alexander et al. 1999). We demonstrate in a companion paper (Baum et al. 2009, submitted) that for all of the sources where there is a [Ne V] 14.3 μm detection, the line ratio is consistent with the low density limit (cf. Sturm et al. 2002); contamination from PAH 14.3 would push the ratio to a (forbidden) value below the low density limit. We conclude that the PAH 14.3 μm feature does not significantly contaminate the [Ne V] λ14.3 μm line strengths in this study or that any contamination is within the uncertainties of the line strength.

4.1.1. Silicate Strengths

This spectrum decomposition technique provides a reasonable model for the $9 - 20$ μm continuum, suitable to measure the relative strength of Sil features. Spoon et al. (2007) defined the Sil strength as the log ratio of the observed flux density at the center of the Sil feature, 10 μm or 18 μm, and the local continuum; e.g.,

$$S_{10} = \ln\left(\frac{F_{10\mu m}[\text{observed}]}{F_{10\mu m}[\text{continuum}]}\right). \tag{2}$$

To measure the Sil strength for the 12 μm sample, we first subtracted PAH and other emission line features as determined by PAHFIT to obtain $S_{10\mu m}[\text{observed}]$. The continuum was derived from the spectrum decomposition as the sum of the (optically thick) dust components, stars, and the continuous part of the warm, thin dust component; the Sil emission features of the warm, thin dust component were replaced by quadratic interpolation between bracketing spectral regions. We used Monte Carlo variation of the PAHFIT model parameters and the data uncertainties to determine the Sil strength uncertainties.

The measured Sil strengths are provided in Table 11.

4.1.2. Continuum Spectral Indices

We further used the PAHFIT spectral decomposition to produce line-free continuum spectra over λ20–30 μm. The MIPS SED data are similarly line-free, except for a few possible detections of O I (λ63 μm); see, e.g., Figure 9.

The data show a range of continuum slopes, and we characterized the spectral shape by fitting a powerlaw model, $F_\lambda \propto \lambda^\alpha$ where α is the spectral index, to the rest wavelength ranges 20–30 μm and 55–90 μm. The results are listed in Table 12. Note that in this convention for α, the Rayleigh-Jeans tail of the Planck spectrum would give $\alpha = -4$.

4.1.3. Comparison with Measurements Employing Spline Approximations for the IR Continuum

Wu et al. (2009) adopt a different but conventional approach to the measurement of the PAH 6.2 μm and 11.2 μm features and the 10 μm Sil strength, and we next consider systematic differences with our measurements. Rather than decompose the spectrum with a dust and lines model as PAHFIT does, their approach was to define a local continuum level based on a spline fit to wavelength ranges narrowly bracketing PAH features. To measure Sil strengths, they adopted the technique of Spoon et al. (2007), which requires the identification of apparently feature-free continuum points to anchor a broader spline interpolation across the Sil features.

Smith et al. (2007b) demonstrated that, for the nearly normal galaxies in the SINGS sample, the PAH line strengths measured by PAHFIT are systematically greater, by factors of 2–3, than line strengths that are based on a spline fit to the neighboring pseudo-continuum. The reason is qualitatively illustrated in the PAHFIT decomposition of NGC 7213 (Figure 9). Both the 6.2 μm and 11.3 μm features blend with weaker, overlapping PAH features. By defining the continuum level based on neighboring spectral points without accounting for PAH blending, the continuum level is overestimated, and the line strength and eqw are underestimated. It is further evident from this decomposition that Sil strengths will be systematically affected if the influence of PAH blends and the underlying continuum shape are not reasonably accounted for; it would not be surprising that the spline technique of produced very different Sil strengths particularly for this source.

We illustrate the systematic differences between the present analysis and that of Wu et al. (2009) in Figs. 10 and 11. As expected, PAHFIT measures, on average, systematically higher values of PAH fluxes and eqws, because PAHFIT removes the contamination of neighboring PAH features to measurement of the local continuum. The measurements of Wu et al. (2009) fall somewhat below the average ratio (PAHFIT / spline continuum) reported by Smith et al. (2007b), but the spline measurements will be sensitive to systematic differences in how the local continuum anchor points were defined in the analysis; such a detailed reconciliation is beyond the scope of the present work.

Similarly, our PAHFIT-derived Sil strengths are systematically more positive, by $\sim$ 0.1–0.3 dex, indicating weaker Sil absorption or stronger Sil emission depending on the sign of the Sil strength. Again, this result is unsurprising, because PAH blends that are not accounted for by decomposition can falsely mimic enhanced continuum surrounding the Sil 10 μm feature, pushing the Sil strength to lower (more negative) values. Recall that we also use an interpolation technique similar to that of Spoon et al. (2007) to measure the strength of the Sil features; the difference is that we perform the analysis on the line-subtracted continuum model produced by PAHFIT.

4.2. SEDs Averaged by Optical Classification

A key goal of this project is to identify and compare the infrared characteristics of AGNs segregated by optical classification. Toward a qualitative first look, we calculated average SEDs

within the following classification bins: (1) S1.0-1.5 & S1n; (2) S1.8-1.9; (3) HBLR Seyfert 2s (S1h & S1i); (4) non-HBLR Seyfert 2s (S2); (5) LINERs; and (6) HII. The results are presented in Figure 12. The separation of the non-HBLR and HBLR S2s was motivated by inspection of Figure 2; non-HBLR S2s appear to have higher-eqw PAH features, for example. Recall that the non-HBLR S2s may in fact harbor a BLR that has not appeared in spectropolarimetric or infrared measurements. All but three of the 20 non-HBLR S2s have been searched for an HBLR, but the inclusion of these three sources in the non-HBLR subsample does not appear to dilute the striking differences between the averaged spectra of non-HBLR S2s and HBLR S2s.

To perform the averaging, all of the data were corrected for redshift and interpolated to a common wavelength grid. The SEDs were converted to λF_λ and normalized to the flux density integrated between 5 and 35 μm, $F(5$–35μm). Objects within a given classification bin were averaged, and the median absolute deviation was computed as a robust estimator of the characteristic spread of SEDs within a classification bin.

Tran (2003) demonstrated that S1s and HBLR S2s show similar IRAS broadband colors, but non-HBLR S2s tend to show cooler IRAS colors (cf. Heisler et al. 1997). The present study confirms this result in some finer detail based on the averaged SEDs. From inspection of Figure 12, S1s (group 1) and HBLR S2s (group 3) show the flattest infrared SEDs. They both present fine-structure emission lines of high-ionization state species, such as [O IV], [Ne IV], and [S IV], with similar equivalent width. Hidden S1s have a slightly redder SED, on average, and also show evidence for Sil 10μm absorption.

Similarly, the average SEDs of S1.8-1.9s (group 2) and non-HBLR S2s (group 4) are essentially indistinguishable. Both groups show strong PAH features, red continuum, and blue IRAC colors suggesting significant contribution of stellar photospheric emission at the short wavelength end. The SEDs of these groups most closely resemble optically classified star-forming galaxies, or starbursts (HII; group 6), except that the average HII SED for this sample shows PAH features with somewhat greater equivalent widths. The [S III] and [Si II] average equivalent widths appear comparable between S1.8-1.9, non-HBLR S2, and HII galaxies.

The average LINER SED stands out by showing a bowl-shaped infrared SED. The SEDs appear to be more strongly dominated by stellar photospheres, or perhaps very hot dust, at shorter wavelengths compared to the other groups, including HII galaxies where starlight appears to dominate the IRAC bands. In this way, the LINERs in our survey are similar to the IR-faint LINERs in the larger sample studied by Sturm et al. (2006). This result is somewhat tempered by the broad range of IRAC colors observed among the LINERs in this survey; from inspection of the six individual LINER SEDs, four show bowl-like SEDs resembling the average (NGC 2639, NGC 4579, NGC 4594, & NGC 5005), and two show HII-like SEDs (NGC 1097 & NGC 3079).

PAH features are commonly detected in this sample, and, even though such features appear at reduced equivalent width in S1 and HBLR S2 objects (cf. Clavel et al. 2000), they are sufficiently strong to obscure Sil features, especially Sil emission. We therefore repeated the SED averaging after

subtracting PAH, H_2, and fine-structure lines based on the results of the PAHFIT decomposition (Section 4.1); the results are provided in Figure 13. Here the average SED of S1 and HBLR S2 distinguish more clearly, with S1 showing clear 10 μm and 18 μm Sil emission features, similar to that observed in QSOs (Hao et al. 2005a). In contrast, the averaged SED of known HBLR S2s show Sil 10 μm in absorption.

The other classes again show broadly similar SEDs after line subtraction. The notable exception is the non-HBLR S2 average, where weak 10 μm Sil absorption appears underneath the subtraction of very strong PAH features. Sil features are essentially absent among intermediate Seyferts (S1.8-1.9), LINERs, and HII galaxies. It is further interesting to note that the IRAC color [3.6] − [4.5] of the averaged S2, LINER, and HII SEDs is consistent with an undiluted Rayleigh-Jeans continuum. The averaged SEDs of the other classes present redder [3.6] − [4.5], indicating dilution from warm dust or some flat-spectrum component.

5. Discussion

We have presented the data reduction and decomposition of *Spitzer* Space Telescope 3.6 – 90 μm spectrophotometry of active galaxies from the extended 12 μm survey. Careful attention was provided to matching 20″, circular diameter apertures across the IRAC and IRS bands (3.6 – 36 μm) with appropriate color and extended source corrections where possible or with an evaluation of the systematic error where such corrections were not available.

We further present SEDs averaged within groups defined by optical AGN classification. We demonstrate that, within this sample, Seyfert 1s show Sil emission on average, known HBLR Seyfert 2s show Sil absorption. This result is broadly compatible with the obscuring torus interpretation, in which case Seyfert 1s are viewed more nearly pole-on, affording a more direct view of hot, Sil emitting dust. HBLR S2s are viewed more nearly edge-on, preferentially through colder, Sil absorbing dust. That the Sil features are, on average, weak is further compatible with the clumpy torus model (Nenkova et al. 2008b; Sirocky et al. 2008; Nenkova et al. 2008a; Levenson et al. 2007).

The other classes, Seyfert 1.8-1.9, non-HBLR S2, LINER, and HII galaxies, produce very weak or absent Sil features. They further show stronger PAH features, bluer IRAC colors, and stronger far-infrared emission (relative to $F[5$–$35\mu m]$). Such SEDs appear to be more commonly dominated by stellar photospheres and star-forming processes. Based on the present analysis, however, we are unable to conclude whether Seyfert 1.8-1.9 and non-HBLR S2 galaxies are in fact more commonly dominated by star formation or whether this result is peculiar to the 12 μm sample owing to selection effects; for example, they may harbor less luminous AGNs, or more heavily absorbed AGNs, but the contribution from star-formation enhanced the 12 μm flux density sufficiently to be included in the 12 μm sample. On the other hand, our results are consistent with the interpretation that the host galaxy dominates the emission of non-HBLR S2s, diminishing our ability to detect the HBLR (Alexander 2001).

In companion work, we present a statistical analysis of the present measurements with attention to differences and similarities between sources grouped by optical classification (Baum et al. 2009, submitted). We are also investigating a decomposition of the SEDs using gridded radiative transfer models with the goal of measuring bolometric contributions of the AGN vs. star-formation as well as constraints on clumpy torus parameters (Gallimore et al. in prep.).

Facility: Spitzer

REFERENCES

Agüero, E. L., Díaz, R. J., & Bajaja, E. 2004, A&A, 414, 453

Alexander, D. M. 2001, MNRAS, 320, L15

Alexander, T., Lutz, D., Sturm, E., Genzel, R., Sternberg, A., & Netzer, H. 2000, ApJ, 536, 710

Alexander, T., Sturm, E., Lutz, D., Sternberg, A., Netzer, H., & Genzel, R. 1999, ApJ, 512, 204

Allington-Smith, J. R., et al. 1989, MNRAS, 238, 603

Alloin, D., Edmunds, M. G., Lindblad, P. O., & Pagel, B. E. J. 1981, A&A, 101, 377

Alloin, D., Pelat, D., Phillips, M., & Whittle, M. 1985, ApJ, 288, 205

Alonso-Herrero, A., Rieke, M. J., Rieke, G. H., & Shields, J. C. 2000, ApJ, 530, 688

Antonucci, R. 1993, ARA&A, 31, 473

Antonucci, R. R. J., & Miller, J. S. 1985, ApJ, 297, 621

Aretxaga, I., Joguet, B., Kunth, D., Melnick, J., & Terlevich, R. J. 1999, ApJ, 519, L123

Clavel, J., & Joly, M. 1984, A&A, 131, 87

Clavel, J., et al. 2000, A&A, 357, 839

Coziol, R., Ribeiro, A. L. B., de Carvalho, R. R., & Capelato, H. V. 1998, ApJ, 493, 563

Dahari, O., & De Robertis, M. M. 1988, ApJS, 67, 249

de Grijp, M. H. K., Keel, W. C., Miley, G. K., Goudfrooij, P., & Lub, J. 1992, A&AS, 96, 389

De Robertis, M. M., & Osterbrock, D. E. 1986, ApJ, 301, 98

Dewangan, G. C., & Griffiths, R. E. 2005, ApJ, 625, L31

Efstathiou, A., Rowan-Robinson, M., & Siebenmorgen, R. 2000, MNRAS, 313, 734

Farrah, D., Afonso, J., Efstathiou, A., Rowan-Robinson, M., Fox, M., & Clements, D. 2003, MN-RAS, 343, 585

Fazio, G. G., et al. 2004, ApJS, 154, 10

Feldmeier, J. J., Brandt, W. N., Elvis, M., Fabian, A. C., Iwasawa, K., & Mathur, S. 1999, ApJ, 510, 167

Filippenko, A. V., & Halpern, J. P. 1984, ApJ, 285, 458

Filippenko, A. V., & Sargent, W. L. W. 1985, ApJS, 57, 503

Gallimore, J. F., Axon, D. J., O'Dea, C. P., Baum, S. A., & Pedlar, A. 2006, AJ, 132, 546

Genzel, R., & Cesarsky, C. J. 2000, ARA&A, 38, 761

Giannuzzo, E. M., & Stirpe, G. M. 1996, A&A, 314, 419

González Delgado, R. M., Heckman, T., Leitherer, C., Meurer, G., Krolik, J., Wilson, A. S., Kinney, A., & Koratkar, A. 1998, ApJ, 505, 174

González Delgado, R. M., & Perez, E. 1996, MNRAS, 280, 53

González-Nuevo, J., Argüeso, F., López-Caniego, M., Toffolatti, L., Sanz, J. L., Vielva, P., & Herranz, D. 2006, MNRAS, 369, 1603

Goodrich, R. W. 1989, ApJ, 340, 190

Goodrich, R. W., Veilleux, S., & Hill, G. J. 1994, ApJ, 422, 521

Hao, L., et al. 2005a, ApJ, 625, L75

—. 2005b, AJ, 129, 1783

Heckman, T. M. 1980, A&A, 87, 152

Heisler, C. A., Lumsden, S. L., & Bailey, J. A. 1997, Nature, 385, 700

Heisler, C. A., Vader, J. P., & Frogel, J. A. 1989, AJ, 97, 986

Ho, L. C., Filippenko, A. V., & Sargent, W. L. W. 1997, ApJS, 112, 315

Horne, K. 1986, PASP, 98, 609

Houck, J. R., et al. 2004, ApJS, 154, 18

Hunt, L. K., & Malkan, M. A. 1999, ApJ, 516, 660

Hunt, L. K., Malkan, M. A., Moriondo, G., & Salvati, M. 1999, ApJ, 510, 637

Inglis, M. D., Brindle, C., Hough, J. H., Young, S., Axon, D. J., Bailey, J. A., & Ward, M. J. 1993, MNRAS, 263, 895

Jaffe, W., et al. 2004, Nature, 429, 47

Kay, L. E. 1994, ApJ, 430, 196

Keel, W. C. 1983, ApJ, 269, 466

Kemper, F., Vriend, W. J., & Tielens, A. G. G. M. 2004, ApJ, 609, 826

Kester, D. J. M., Beintema, D. A., & Lutz, D. 2003, in ESA Special Publication, Vol. 481, The Calibration Legacy of the ISO Mission, ed. L. Metcalfe, A. Salama, S. B. Peschke, & M. F. Kessler, 375

Kewley, L. J., Heisler, C. A., Dopita, M. A., & Lumsden, S. 2001, ApJS, 132, 37

Kim, D.-C., Sanders, D. B., Veilleux, S., Mazzarella, J. M., & Soifer, B. T. 1995, ApJS, 98, 129

Kirhakos, S. D., & Steiner, J. E. 1990, AJ, 99, 1722

Kollatschny, W., Biermann, P., Fricke, K. J., Huchtmeier, W., & Witzel, A. 1983, A&A, 119, 80

Kollatschny, W., & Fricke, K. J. 1985, A&A, 143, 393

Levenson, N. A., Sirocky, M. M., Hao, L., Spoon, H. W. W., Marshall, J. A., Elitzur, M., & Houck, J. R. 2007, ApJ, 654, L45

Lu, N., et al. 2008, PASP, 120, 328

Lumsden, S. L., Heisler, C. A., Bailey, J. A., Hough, J. H., & Young, S. 2001, MNRAS, 327, 459

Madore, B. F., & Steer, I. P. 2008, Master List of Galaxy Distances, `http://nedwww.ipac.caltech.edu/level5/NED1D/intro.html`

Makovoz, D., & Khan, I. 2005, in Astronomical Society of the Pacific Conference Series, Vol. 347, Astronomical Data Analysis Software and Systems XIV, ed. P. Shopbell, M. Britton, & R. Ebert, 81

Makovoz, D., Roby, T., Khan, I., & Booth, H. 2006, in Society of Photo-Optical Instrumentation Engineers (SPIE) Conference Series, Vol. 6274, Society of Photo-Optical Instrumentation Engineers (SPIE) Conference Series

Márquez, I., et al. 2004, A&A, 416, 475

Marshall, J. A., Herter, T. L., Armus, L., Charmandaris, V., Spoon, H. W. W., Bernard-Salas, J., & Houck, J. R. 2007, ApJ, 670, 129

Mazzarella, J. M., & Balzano, V. A. 1986, ApJS, 62, 751

Miller, J. S., & Goodrich, R. W. 1990, ApJ, 355, 456

Moran, E. C., Barth, A. J., Kay, L. E., & Filippenko, A. V. 2000, ApJ, 540, L73

Moustakas, J., & Kennicutt, Jr., R. C. 2006, ApJS, 164, 81

Mulchaey, J. S., Wilson, A. S., & Tsvetanov, Z. 1996, ApJS, 102, 309

Nagar, N. M., Wilson, A. S., Mulchaey, J. S., & Gallimore, J. F. 1999, ApJS, 120, 209

Nenkova, M., Ivezić, Ž., & Elitzur, M. 2002, ApJ, 570, L9

Nenkova, M., Sirocky, M. M., Ivezić, Ž., & Elitzur, M. 2008a, ApJ, 685, 147

Nenkova, M., Sirocky, M. M., Nikutta, R., Ivezić, Ž., & Elitzur, M. 2008b, ApJ, 685, 160

Ossenkopf, V., Henning, T., & Mathis, J. S. 1992, A&A, 261, 567

Osterbrock, D. E. 1977, ApJ, 215, 733

Osterbrock, D. E., & Koski, A. T. 1976, MNRAS, 176, 61P

Osterbrock, D. E., & Pogge, R. W. 1985, ApJ, 297, 166

Peterson, B. M., et al. 2000, ApJ, 542, 161

Phillips, M. M., Pagel, B. E. J., Edmunds, M. G., & Diaz, A. 1984, MNRAS, 210, 701

Pier, E. A., & Krolik, J. H. 1992, ApJ, 401, 99

Rafanelli, P., Osterbrock, D. E., & Pogge, R. W. 1990, AJ, 99, 53

Reach, W. T., et al. 2005, PASP, 117, 978

Regan, M. W., & Gruendl, R. A. 1995, in Astronomical Society of the Pacific Conference Series, Vol. 77, Astronomical Data Analysis Software and Systems IV, ed. R. A. Shaw, H. E. Payne, & J. J. E. Hayes, 335

Reunanen, J., Kotilainen, J. K., & Prieto, M. A. 2002, MNRAS, 331, 154

Rieke, G. H., et al. 2004, ApJS, 154, 25

Risaliti, G., Elvis, M., Fabbiano, G., Baldi, A., Zezas, A., & Salvati, M. 2007, ApJ, 659, L111

Risaliti, G., Elvis, M., & Nicastro, F. 2002, ApJ, 571, 234

Rush, B., Malkan, M. A., & Edelson, R. A. 1996, ApJ, 473, 130

Rush, B., Malkan, M. A., & Spinoglio, L. 1993, ApJS, 89, 1

Savitzky, A., & Golay, M. J. E. 1964, Analytical Chemistry, 36, 1627

Shields, J. C., & Filippenko, A. V. 1990, AJ, 100, 1034

Siebenmorgen, R., & Krügel, E. 2007, A&A, 461, 445

Sirocky, M. M., Levenson, N. A., Elitzur, M., Spoon, H. W. W., & Armus, L. 2008, ApJ, 678, 729

Smith, J. D. T., et al. 2007a, PASP, 119, 1133

—. 2007b, ApJ, 656, 770

Smith, J. E., Robinson, A., Alexander, D. M., Young, S., Axon, D. J., & Corbett, E. A. 2004, MNRAS, 350, 140

Spinoglio, L., Andreani, P., & Malkan, M. A. 2002, ApJ, 572, 105

Spoon, H. W. W., Marshall, J. A., Houck, J. R., Elitzur, M., Hao, L., Armus, L., Brandl, B. R., & Charmandaris, V. 2007, ApJ, 654, L49

Storchi-Bergmann, T., Kinney, A. L., & Challis, P. 1995, ApJS, 98, 103

Sturm, E., Lutz, D., Tran, D., Feuchtgruber, H., Genzel, R., Kunze, D., Moorwood, A. F. M., & Thornley, M. D. 2000, A&A, 358, 481

Sturm, E., Lutz, D., Verma, A., Netzer, H., Sternberg, A., Moorwood, A. F. M., Oliva, E., & Genzel, R. 2002, A&A, 393, 821

Sturm, E., et al. 2006, ApJ, 653, L13

Taylor, D., Dyson, J. E., Axon, D. J., & Pedlar, A. 1989, MNRAS, 240, 487

Thean, A., Pedlar, A., Kukula, M. J., Baum, S. A., & O'Dea, C. P. 2000, MNRAS, 314, 573

—. 2001, MNRAS, 325, 737

Tran, H. D. 1995, ApJ, 440, 565

—. 2001, ApJ, 554, L19

—. 2003, ApJ, 583, 632

Tristram, K. R. W., et al. 2007, A&A, 474, 837

Tully, R. B., & Fisher, J. R. 1988, Catalog of Nearby Galaxies (Cambridge: Cambridge University Press)

Urry, C. M., & Padovani, P. 1995, PASP, 107, 803

Vaceli, M. S., Viegas, S. M., Gruenwald, R., & de Souza, R. E. 1997, AJ, 114, 1345

van Dokkum, P. G. 2001, PASP, 113, 1420

Veilleux, S. 1988, AJ, 95, 1695

Veilleux, S., Kim, D.-C., Sanders, D. B., Mazzarella, J. M., & Soifer, B. T. 1995, ApJS, 98, 171

Véron-Cetty, M.-P., & Véron, P. 2006, A&A, 455, 773

Véron-Cetty, M.-P., Véron, P., & Gonçalves, A. C. 2001, A&A, 372, 730

Whittle, M., Pedlar, A., Meurs, E. J. A., Unger, S. W., Axon, D. J., & Ward, M. J. 1988, ApJ, 326, 125

Winkler, H. 1988, MNRAS, 234, 703

—. 1992, MNRAS, 257, 677

Wu, Y., Charmandaris, V., Huang, J., Spinoglio, L., & Tommasin, S. 2009, ApJ, 701, 658

Young, S., Hough, J. H., Efstathiou, A., Wills, B. J., Bailey, J. A., Ward, M. J., & Axon, D. J. 1996, MNRAS, 281, 1206

Table 1.   AGNs from the extended 12 μm sample observed by the Spitzer Space Telescope

Source ID	Class	Ref	RA (J2000) (h:m:s)	Dec (J2000) ($^\circ:':''$)	cz (km s^{-1})	D (Mpc)	PID
MRK335	S1n	1	00:06:19.53	20:12:10.5	7730	110.4	3269
MRK938	HII	2	00:11:06.56	−12:06:27.3	5881	84.0	3269, 3672
E12-G21	S1n	3	00:40:45.93	−79:14:24.2	9000	128.6	3269
MRK348	S1h	4	00:48:47.16	31:57:25.2	4507	64.4	3269
NGC424	S1h	5	01:11:27.66	−38:05:00.0	3527	50.4	3269
NGC526A	S1.9	6	01:23:54.39	−35:03:55.4	5725	81.8	86, 3269
NGC513	S1h	7	01:24:26.78	33:47:58.4	5859	83.7	3269
F01475-0740	S1h	8	01:50:02.69	−07:25:48.4	5296	75.7	3269
NGC931	S1.0-1.5	9	02:28:14.49	31:18:41.7	4992	71.3	3269
NGC1056	HII	10	02:42:48.29	28:34:26.1	1545	22.1	3269
NGC1097	LINER	11, 12	02:46:18.91	−30:16:28.8	1271	*17.5	159, 3269
NGC1125	S2	13	02:51:40.44	−16:39:02.4	3277	46.8	3269
NGC1143-4	S2	8, 10	02:55:11.66	−00:11:03.4	8648	123.5	21, 3269
M-2-8-39	S1h	8, 14	03:00:30.62	−11:24:57.2	8962	128.0	3269
NGC1194	S1.8-1.9	15, 16	03:03:49.12	−01:06:13.2	4076	58.2	3269
NGC1241	S2	8, 17	03:11:14.63	−08:55:18.1	4052	57.9	3269
NGC1320	S2	8, 18	03:24:48.69	−03:02:32.0	2663	*37.7	3269
NGC1365	S1.8	19	03:33:36.39	−36:08:25.8	1636	*17.7	3269, 3672
NGC1386	S1i	20	03:36:46.20	−35:59:57.0	868	*16.2	3269
F03450+0055	S1n	1, 21	03:47:40.22	01:05:13.7	9294	132.8	3269
NGC1566	S1.5	22, 23, 24	04:20:00.41	−54:56:16.7	1504	*11.8	159, 3269
F04385-0828	S1h	8	04:40:54.96	−08:22:21.9	4527	64.7	3269
NGC1667	S2	8	04:48:37.15	−06:19:11.9	4547	65.0	3269
E33-G2	S2	25	04:55:58.88	−75:32:28.4	5426	77.5	3269
M-5-13-17	S1.5	23	05:19:35.84	−32:39:28.1	3790	54.1	3269
MRK6	S1.5	26, 27	06:52:12.35	74:25:37.2	5640	80.6	3269
MRK79	S1.2	28	07:42:32.84	49:48:34.5	6652	95.0	3269
NGC2639	LINER	29	08:43:38.06	50:12:20.4	3336	47.7	3269
MRK704	S1.5	30	09:18:25.98	16:18:20.0	8764	125.2	3269
NGC2992	S1i	31	09:45:41.93	−14:19:34.6	2311	*30.5	96, 3269
MRK1239	S1n	32	09:52:19.09	−01:36:43.5	5974	85.3	3269
NGC3079	LINER	33	10:01:57.85	55:40:46.9	1116	*19.7	59, 3269
NGC3227	S1.5	34	10:23:30.55	19:51:54.6	1157	*20.9	96, 3269
NGC3511	HII	25	11:03:23.81	−23:05:12.3	1109	*14.6	3269
NGC3516	S1.2	34	11:06:47.49	72:34:07.6	2649	*38.9	3269
M+0-29-23	HII	10	11:21:12.27	−02:59:02.5	7464	106.6	3269
NGC3660	S1.8	8, 35	11:23:32.27	−08:39:30.4	3679	52.6	3269
NGC3982	S1.9	34	11:56:28.12	55:07:31.3	1109	*21.8	3269
NGC4051	S1n	36	12:03:09.61	44:31:53.0	700	*17.0	3269
UGC7064	S1.9	37	12:04:43.32	31:10:38.1	7494	107.1	3269

Table 1—Continued

Source ID	Class	Ref	RA (J2000) (h:m:s)	Dec (J2000) (°:′:″)	cz (km s^{-1})	D (Mpc)	PID
NGC4151	S1.5	34	12:10:32.57	39:24:21.0	995	*20.3	3269
MRK766	S1n	32	12:18:26.51	29:48:46.9	3876	55.4	3269
NGC4388	S1h	38	12:25:46.81	12:39:43.3	2524	*18.1	3269, 20695
NGC4501	S2	8	12:31:59.18	14:25:13.3	2281	*20.7	3269
NGC4579	LINER	34, 39	12:37:43.52	11:49:05.4	1519	*16.8	159, 3269
NGC4593	S1	40	12:39:39.44	−05:20:39.0	2698	*44.0	3269
NGC4594	LINER	34	12:39:59.44	−11:37:22.9	1024	*10.9	159, 3269
NGC4602	HII	40	12:40:36.98	−05:07:58.5	2539	*34.4	3269
TOL1238-364	S1h	8	12:40:52.86	−36:45:21.2	3275	46.8	3269
M-2-33-34	S1n	37	12:52:12.49	−13:24:53.0	4386	62.7	3269
NGC4941	S2	5	13:04:13.13	−05:33:05.8	1108	*13.8	86, 3269
NGC4968	S2	34	13:07:05.96	−23:40:36.4	2957	42.2	3269
NGC5005	LINER	34	13:10:56.29	37:03:32.9	946	*17.5	3269
NGC5033	S1.8	34	13:13:27.49	36:35:37.6	875	*20.6	159, 3269
NGC5135	S2	41	13:25:44.04	−29:50:00.2	4105	58.6	3269
M-6-30-15	S1.5	23	13:35:53.78	−34:17:44.2	2323	33.2	3269
NGC5256	S2	42	13:38:17.25	48:16:32.4	8211	117.3	3269
IC4329A	S1.5	23	13:49:19.24	−30:18:34.4	4813	68.8	3269, 30318
NGC5347	S2	8, 43	13:53:17.80	33:29:27.3	2335	*36.7	3269
NGC5506	S1i	31	14:13:14.87	−03:12:27.6	1853	*28.7	3269
NGC5548	S1.5	34	14:17:59.52	25:08:12.6	5149	73.6	69, 86, 3269
MRK817	S1.5	44	14:36:22.08	58:47:39.6	9430	134.7	3269
NGC5929	S2	45, 47	15:26:06.20	41:40:14.5	2492	*38.5	3269
NGC5953	S2	47	15:34:32.39	15:11:37.2	1965	*33.0	59, 3269
M-2-40-4	S1.9	48, 49, 50	15:48:24.96	−13:45:26.9	7553	107.9	3269
F15480-0344	S1h	8, 38	15:50:41.48	−03:53:18.1	9084	129.8	3269
NGC6810	HII	25	19:43:34.42	−58:39:20.3	2031	*29.0	3269
NGC6860	S1.5	23	20:08:46.90	−61:05:59.6	4462	63.7	3269
NGC6890	S2	5, 51	20:18:18.02	−44:48:24.7	2419	*31.8	3269
IC5063	S1h	52	20:52:02.29	−57:04:07.5	3402	48.6	86, 3269
UGC11680	S2	49	21:07:41.35	03:52:17.9	7791	111.3	3269
NGC7130	S2	53, 54, 55, 56	21:48:19.52	−34:57:04.8	4842	69.2	3269, 3672
NGC7172	S2	41, 57	22:02:01.90	−31:52:10.4	2603	*33.9	86, 3269
NGC7213	S1	58	22:09:16.21	−47:09:59.7	1750	*22.0	3269
NGC7314	S1i	59	22:35:46.21	−26:03:01.5	1428	*19.0	86, 3269
M-3-58-7	S1h	8	22:49:37.17	−19:16:26.2	9432	134.7	3269
NGC7469	S1.5	44	23:03:15.61	08:52:26.3	4892	69.9	32, 3269
NGC7496	S2	38, 49, 60	23:09:47.29	−43:25:40.2	1649	*20.1	3269
NGC7582	S1i	61	23:18:23.63	−42:22:13.1	1575	*18.8	3269
NGC7590	S2	60	23:18:54.81	−42:14:20.0	1575	*23.7	3269

Table 1—Continued

Source ID	Class	Ref	RA (J2000) (h:m:s)	Dec (J2000) (°:′:″)	cz (km s^{-1})	D (Mpc)	PID
NGC7603	S1.5	44	23:18:56.67	00:14:38.1	8851	126.4	3269
NGC7674	S1h	4, 9	23:27:56.72	08:46:44.4	8671	123.9	3269, 3672
CGCG381-051	HII	8	23:48:41.74	02:14:23.5	9194	131.3	3269

Note. — The source ID is based on the primary source identification of Rush et al. (1993). AGN classifications are from (1) Véron-Cetty et al. (2001), (2) Mulchaey et al. (1996), (3) Clavel & Joly (1984), (4) Miller & Goodrich (1990), (5) Moran et al. (2000), (6) Nagar et al. (1999), (7) Tran (1995), (8) Tran (2003), (9) Veilleux (1988), (10) Veilleux et al. (1995), (11) Keel (1983), (12) Phillips et al. (1984), (13) Winkler (1988), (14) Heisler et al. (1989), (15) de Grijp et al. (1992), (16) Hao et al. (2005b), (17) Vaceli et al. (1997), (18) De Robertis & Osterbrock (1986), (19) Alloin et al. (1981), (20) Reunanen et al. (2002), (21) Giannuzzo & Stirpe (1996), (22) Alloin et al. (1985), (23) Winkler (1992), (24) Agüero et al. (2004), (25) Kirhakos & Steiner (1990), (26) Osterbrock & Koski (1976), (27) Feldmeier et al. (1999), (28) Osterbrock (1977), (29) Alonso-Herrero et al. (2000), (30) Mazzarella & Balzano (1986), (31) Goodrich et al. (1994), (32) Osterbrock & Pogge (1985), (33) Heckman (1980), (34) Ho et al. (1997), (35) Kollatschny et al. (1983), (36) Peterson et al. (2000), (37) Goodrich (1989), (38) Young et al. (1996), (39) Filippenko & Sargent (1985), (40) Kollatschny & Fricke (1985), (41) Heisler et al. (1997), (42) Kay (1994), (43) González Delgado & Perez (1996), (44) Dahari & De Robertis (1988), (45) Whittle et al. (1988), (46) Taylor et al. (1989), (47) Rafanelli et al. (1990), (48) Tran (2001), (49) Kewley et al. (2001), (50) Lumsden et al. (2001), (51) Márquez et al. (2004), (52) Inglis et al. (1993), (53) Shields & Filippenko (1990), (54) Kim et al. (1995), (55) González Delgado et al. (1998), (56) Moustakas & Kennicutt (2006), (57) Coziol et al. (1998), (58) Filippenko & Halpern (1984), (59) Dewangan & Griffiths (2005), (60) Storchi-Bergmann et al. (1995), and (61) Aretxaga et al. (1999). The classification naming convention broadly follows Véron-Cetty & Véron (2006): S1.n refers to Seyfert types 1.n (1.2, 1.5, 1.8, or 1.9); S1h = hidden Seyfert 1 revealed by spectropolarimetry; S1i = hidden Seyfert 1 revealed by broad Paschen or Brackett lines or via another, non-polarimetric technique; S1n = narrow-line Seyfert 1; S2 = Seyfert 2; HII = star-forming or starburst galaxy. For NGC 1194 and NGC 5033, the classifications were based on inspection of the spectra presented in the cited references and differ from from the classification assigned in those references. M-2-40-4 presents a S1.9 spectrum, although spectropolarimetry reveals broader Balmer lines; we retain the S1.9 classification. To the best of our knowledge, HBLRs have been searched in all but three of the 20 S2s in this list: NGC 1125, E33-G2, and NGC 4968 (Tran 2003). Source coordinates are based on the astrometry of the IRAC 8.0 μm image. Recessional velocities are from NED. The adopted distances either were calculated using the Hubble Law assuming $H_0 = 70$ km s^{-1} Mpc^{-1} or, where data were available in NED, taken from an average of redshift-independent distance indicators. Redshift-independent distances, compiled by Madore & Steer (2008), which, for this sample, commonly derive solely from Tully & Fisher (1988), are marked by (*). PID lists the Spitzer program codes that were used to construct the present data set. Spitzer PID 3269 indicates data from our original Cycle 1 proposal. The SINGS key project is PID 159.

Table 2.   IRAC Photometry of the 12 μm AGN sample

Object	[3.6]	unc	[4.5]	unc	[5.8]	unc	[8.0]	unc
MRK335	8.99	0.07	8.31	0.07	7.67	0.06	6.69	0.05
MRK938	9.55	0.05	9.24	0.04	7.74	0.05	5.09	0.02
E12-G21	9.63	0.09	9.14	0.10	8.31	0.08	6.22	0.07
MRK348	9.27	0.08	8.46	0.08	7.67	0.06	6.38	0.04
NGC424	7.83	0.05	6.94	0.04	6.11	0.03	4.95	0.02
NGC526A	9.00	0.07	8.33	0.07	7.66	0.07	6.67	0.06
NGC5135	8.95	0.10	8.60	0.09	7.35	0.08	4.82	0.07
F01475-0740	10.83	0.16	9.89	0.14	8.59	0.10	7.16	0.06
NGC931	8.38	0.05	7.75	0.05	6.87	0.04	5.78	0.03
NGC1056	9.26	0.11	9.32	0.12	8.23	0.12	5.50	0.10
NGC1097	7.73	0.10	7.75	0.11	6.54	0.10	3.98	0.10
NGC1125	10.05	0.11	9.67	0.11	8.45	0.10	6.51	0.05
NGC1143-4	9.68	0.09	9.44	0.08	8.37	0.09	5.66	0.09
M-2-8-39	10.86	0.14	10.25	0.15	9.27	0.13	7.35	0.07
NGC1194	9.29	0.08	8.38	0.07	7.31	0.05	6.10	0.04
NGC1241	9.87	0.11	9.86	0.12	9.56	0.16	7.11	0.09
NGC1320	9.10	0.08	8.47	0.07	7.48	0.06	5.96	0.04
NGC1365	7.23	0.07	6.85	0.06	5.70	0.08	3.25	0.09
NGC1386	8.64	0.08	8.15	0.07	7.16	0.05	5.56	0.03
F03450+0055	9.11	0.08	8.46	0.07	7.74	0.06	6.61	0.04
NGC1566	8.67	0.09	8.59	0.08	7.94	0.07	6.14	0.05
F04385-0828	9.09	0.08	8.04	0.06	7.04	0.05	5.64	0.03
NGC1667	9.60	0.11	9.65	0.12	8.41	0.14	5.96	0.11
E33-G2	9.40	0.09	8.69	0.08	7.91	0.07	6.65	0.05
M-5-13-17	9.74	0.10	9.38	0.10	8.26	0.09	6.65	0.07
MRK6	8.71	0.06	8.12	0.06	7.60	0.05	6.63	0.05
MRK79	8.73	0.06	8.05	0.06	7.24	0.05	6.05	0.04
NGC2639	9.17	0.11	9.25	0.12	8.67	0.15	7.27	0.12
MRK704	8.84	0.07	8.06	0.06	7.35	0.05	6.08	0.04
NGC2992	8.46	0.06	8.07	0.05	7.25	0.05	5.35	0.05
MRK1239	7.70	0.04	7.03	0.04	6.31	0.03	5.27	0.03
NGC3079	8.12	0.09	8.09	0.09	6.61	0.09	3.78	0.08
NGC3227	8.48	0.06	8.16	0.06	7.18	0.06	5.36	0.04
NGC3511	10.03	0.12	10.13	0.13	9.41	0.21	6.20	0.11
NGC3516	8.42	0.06	7.96	0.06	7.27	0.06	6.16	0.04
M+0-29-23	9.93	0.11	9.65	0.11	8.30	0.09	5.59	0.06
NGC3660	10.68	0.13	10.66	0.16	10.35	0.34	7.65	0.12
NGC3982	9.91	0.11	9.95	0.12	8.81	0.14	6.36	0.10
NGC4051	8.53	0.06	7.94	0.06	7.10	0.04	5.56	0.03
UGC7064	9.98	0.10	9.67	0.11	8.88	0.09	6.62	0.12
NGC4151	7.42	0.05	6.67	0.03	5.86	0.03	4.52	0.02

Table 2—Continued

Object	[3.6]	unc	[4.5]	unc	[5.8]	unc	[8.0]	unc
MRK766	9.06	0.07	8.32	0.07	7.60	0.06	5.99	0.04
NGC4388	8.79	0.07	8.35	0.06	7.11	0.05	5.49	0.08
NGC4501	8.53	0.10	8.61	0.11	8.42	0.14	6.98	0.11
NGC4579	8.25	0.09	8.23	0.09	7.87	0.08	7.12	0.06
NGC4593	8.38	0.07	7.82	0.06	7.12	0.05	5.86	0.03
NGC4594	7.04	0.10	7.16	0.11	6.93	0.10	6.95	0.09
NGC4602	10.23	0.12	10.26	0.13	9.38	0.19	7.37	0.10
TOL1238-364	9.36	0.09	8.88	0.08	7.77	0.07	5.47	0.10
M-2-33-34	10.12	0.11	9.87	0.12	9.06	0.13	7.39	0.08
NGC4941	9.65	0.10	9.58	0.11	9.02	0.28	8.01	0.13
NGC4968	9.66	0.09	9.04	0.09	8.02	0.07	6.20	0.04
NGC5005	7.81	0.10	7.85	0.10	7.35	0.10	5.63	0.09
NGC5033	8.26	0.10	8.30	0.10	7.59	0.10	5.45	0.10
NGC513	9.68	0.10	9.45	0.10	8.72	0.13	6.32	0.09
M-6-30-15	8.55	0.06	7.87	0.06	7.16	0.05	6.07	0.04
NGC5256	10.19	0.12	10.01	0.12	8.56	0.11	5.67	0.06
IC4329A	7.38	0.03	6.68	0.04	5.94	0.03	4.93	0.02
NGC5347	9.87	0.10	9.21	0.10	8.18	0.07	6.56	0.05
NGC5506	7.02	0.03	6.25	0.03	5.49	0.02	4.41	0.02
NGC5548	9.49	0.05	8.85	0.04	7.96	0.03	6.48	0.02
MRK817	9.10	0.07	8.45	0.07	7.61	0.06	6.33	0.04
NGC5929	10.33	0.12	10.36	0.14	9.59	0.20	8.52	0.14
NGC5953	9.13	0.10	9.24	0.10	7.70	0.11	4.85	0.10
M-2-40-4	8.51	0.06	7.86	0.06	7.12	0.04	5.58	0.04
F15480-0344	10.38	0.12	9.66	0.12	8.75	0.10	7.03	0.07
NGC6810	8.14	0.09	8.17	0.10	7.22	0.09	4.49	0.08
NGC6860	9.06	0.07	8.44	0.07	7.57	0.06	6.36	0.04
NGC6890	9.50	0.10	9.21	0.10	8.35	0.09	6.35	0.06
IC5063	8.79	0.07	7.90	0.06	6.80	0.05	5.14	0.03
UGC11680	10.02	0.10	9.64	0.11	9.09	0.11	7.28	0.10
NGC7130	9.43	0.08	9.16	0.07	7.92	0.07	5.15	0.06
NGC7172	8.36	0.07	7.88	0.06	7.00	0.07	5.31	0.06
NGC7213	8.02	0.08	7.79	0.08	7.31	0.07	6.43	0.06
NGC7314	9.94	0.10	9.53	0.11	8.87	0.19	7.37	0.08
M-3-58-7	8.94	0.07	8.25	0.07	7.49	0.05	6.04	0.04
NGC7469	8.18	0.05	7.69	0.04	6.57	0.05	4.33	0.04
NGC7496	9.99	0.11	9.83	0.11	8.46	0.10	5.93	0.06
NGC7582	7.57	0.05	7.00	0.04	5.87	0.05	3.73	0.05
NGC7590	9.44	0.11	9.55	0.12	8.85	0.16	6.37	0.11
NGC7603	8.23	0.05	7.65	0.05	7.02	0.04	5.83	0.03
NGC7674	8.99	0.04	8.20	0.03	7.23	0.03	5.40	0.02

Table 2—Continued

Object	[3.6]	unc	[4.5]	unc	[5.8]	unc	[8.0]	unc
CGCG381-051	11.14	0.15	10.83	0.17	9.67	0.20	6.91	0.07

Note. — IRAC photometry is presented in the *Spitzer* IRAC magnitude system. Zero point flux densities are 280.9, 179.7, 115.0, and 64.13 Jy for the 3.6, 4.5, 5.8, and 8.0 μm channels, respectively. Color corrections and corrections for extended emission have been applied. Uncertainties include contributions from detector noise and photon counting statistics, noise in the IRS spectra and numerical integration errors as they contribute to the color correction, and the (10% of extended flux) uncertainty of the extended emission correction.

Table 3.   Comparison of Line Measurements using Optimal and Non-optimal Weighting

Line (1)	$\lambda(\mu m)$ (2)	Non-opt. Flux (3)		Opt. Flux (4)		Non-opt. EQW (5)		Opt. EQW (6)	
		NGC 3079							
H$_2$S(1)	17.05	51	(5)	51	(4)	137	(14)	135	(10)
[NeII]	12.81	183	(11)	190	(12)	345	(22)	352	(22)
[NeIII]	15.56	22	(6)	23	(6)	41	(12)	44	(11)
[OIV]	25.91	30	(7)	31	(6)	38	(8)	39	(8)
[SIII]	18.71	18	(3)	16	(3)	51	(7)	44	(7)
[SIII]	33.50	63	(14)	61	(15)	43	(10)	42	(11)
[SiII]	34.82	260	(27)	262	(26)	165	(17)	166	(16)
PAH	6.22	2520	(110)	2570	(120)	3890	(170)	3950	(180)
PAH	11.33	1380	(50)	1370	(51)	5200	(190)	5170	(190)
		F01475-0740							
[NeII]	12.81	16	(1)	16	(1)	44	(4)	42	(2)
[NeIII]	15.56	11	(1)	10	(1)	28	(4)	25	(2)
[NeV]	14.32	< 4	$\cdots$	2	(1)	< 10	$\cdots$	6	(2)
[SIII]	18.71	< 4	$\cdots$	5	(1)	< 9	$\cdots$	11	(3)
PAH	6.22	< 56	$\cdots$	40	(9)	< 160	$\cdots$	113	(26)
PAH	11.33	70	(7)	69	(5)	165	(17)	161	(11)

Note. — Integrated fluxes are given in units of 10^{-17} W m^{-2}, and equivalent widths are given in units of nm. Uncertainties (1σ) are listed in parentheses. Upper limits are 3σ. Only lines with a detection in the optimal extraction are presented; all lines that are detected in the unweighted spectrum are also detected in the optimally extracted spectrum. Measurements from the unweighted spectrum are given in columns (3) and (5); measurements from the optimally weighted spectrum are given in the neighboring columns (4) and (6).

– 33 –

Table 4. PAH Fluxes

Source ID	6.2 μm	7.4 μm	7.6 μm	7.8 μm	8.3 μm	8.6 μm	11.2 μm	11.3 μm	12.0 μm	12.6 μm	17.0 μm
MRK335	< 29	< 105	< 29	58 (10)	37 (11)	28 (8)	< 7	22 (6)	27 (6)	31 (4)	< 18
MRK938	735 (34)	1470 (150)	789 (45)	943 (40)	415 (29)	451 (21)	152 (4)	378 (12)	223 (15)	487 (20)	225 (26)
E12-G21	208 (21)	< 201	258 (18)	263 (17)	57 (11)	148 (9)	33 (4)	190 (10)	67 (8)	142 (15)	96 (8)
MRK348	< 37	244 (31)	< 44	113 (16)	< 39	58 (9)	14 (3)	51 (6)	< 28	24 (7)	< 46
NGC424	41 (12)	509 (76)	137 (33)	189 (38)	145 (24)	88 (19)	< 21	55 (14)	57 (14)	< 56	< 60
NGC526A	22 (7)	207 (29)	35 (8)	37 (11)	43 (9)	26 (6)	< 7	30 (6)	45 (5)	26 (5)	< 31
NGC513	186 (20)	< 312	355 (31)	236 (31)	< 84	153 (19)	99 (3)	150 (10)	76 (12)	105 (12)	109 (11)
F01475-0740	40 (9)	90 (29)	103 (10)	< 33	< 23	30 (6)	13 (2)	69 (5)	60 (6)	66 (6)	< 27
NGC931	78 (10)	< 176	73 (22)	118 (26)	< 50	39 (12)	16 (4)	112 (7)	35 (9)	36 (9)	36 (12)
NGC1056	648 (33)	665 (88)	898 (42)	716 (48)	225 (34)	468 (12)	202 (11)	395 (30)	157 (11)	320 (16)	205 (18)
NGC1097	2219 (96)	2710 (240)	2850 (150)	3190 (180)	1050 (130)	1625 (36)	642 (30)	1703 (78)	868 (41)	1810 (140)	548 (42)
NGC1125	167 (15)	435 (82)	206 (26)	192 (21)	93 (8)	79 (6)	51 (3)	130 (7)	52 (7)	117 (8)	56 (8)
NGC1143-4	364 (24)	402 (48)	484 (14)	474 (12)	125 (7)	227 (6)	83 (4)	252 (11)	110 (4)	204 (10)	142 (9)
M-2-8-39	< 27	< 188	< 53	< 50	< 31	23 (7)	< 5	< 15	< 20	13 (4)	84 (14)
NGC1194	32 (8)	< 138	113 (17)	96 (18)	< 46	< 34	< 8	50 (7)	48 (12)	35 (7)	64 (10)
NGC1241	112 (16)	338 (93)	< 104	190 (38)	63 (18)	62 (12)	31 (3)	79 (8)	32 (10)	45 (5)	81 (9)
NGC1320	118 (10)	< 255	213 (29)	195 (32)	61 (17)	95 (13)	39 (4)	98 (8)	25 (7)	76 (10)	< 37
NGC1365	3730 (180)	4330 (580)	4890 (260)	5610 (310)	1720 (190)	2436 (84)	839 (42)	2510 (110)	1243 (64)	2590 (180)	1220 (82)
NGC1386	85 (15)	< 264	270 (28)	274 (30)	82 (16)	93 (10)	42 (4)	220 (9)	108 (14)	148 (14)	146 (21)
F03450+0055	32 (6)	249 (36)	< 24	69 (7)	76 (6)	28 (5)	< 6	< 16	33 (6)	36 (6)	< 30
NGC1566	160 (14)	286 (53)	218 (17)	303 (20)	106 (14)	122 (9)	79 (3)	227 (9)	85 (6)	142 (8)	159 (7)
F04385-0828	54 (11)	< 134	103 (18)	< 51	< 44	< 33	< 10	104 (9)	91 (12)	119 (11)	< 45
NGC1667	387 (29)	563 (85)	436 (35)	518 (40)	121 (29)	290 (20)	106 (5)	279 (14)	102 (12)	230 (11)	159 (17)
E33-G2	< 40	335 (54)	< 50	< 47	55 (8)	39 (7)	< 8	33 (8)	< 33	< 18	< 21
M-5-13-17	114 (9)	< 227	96 (23)	143 (24)	44 (12)	102 (9)	56 (3)	103 (7)	35 (6)	47 (6)	61 (9)
MRK6	30 (7)	< 132	51 (13)	< 24	< 30	< 28	12 (2)	< 16	< 15	< 22	73 (14)
MRK79	29 (6)	335 (74)	< 62	63 (14)	57 (9)	< 21	< 9	51 (7)	40 (7)	50 (10)	< 47
NGC2639	68 (17)	< 249	119 (28)	110 (27)	< 66	< 51	31 (3)	80 (9)	< 36	39 (8)	61 (10)
MRK704	< 29	< 92	< 39	62 (16)	< 36	< 24	< 6	< 18	< 22	< 23	< 30
NGC2992	352 (26)	706 (96)	434 (29)	521 (34)	193 (18)	258 (13)	119 (5)	330 (14)	142 (12)	187 (27)	274 (25)
MRK1239	45 (13)	246 (58)	133 (28)	134 (17)	90 (15)	74 (13)	24 (6)	54 (13)	59 (12)	78 (11)	< 42
NGC3079	2570 (120)	4140 (340)	3350 (150)	3960 (190)	1330 (140)	1233 (73)	361 (18)	1372 (51)	859 (45)	1804 (95)	949 (45)
NGC3227	329 (16)	572 (62)	370 (30)	506 (22)	164 (14)	239 (12)	120 (9)	391 (24)	171 (13)	216 (18)	328 (27)
NGC3511	321 (22)	315 (69)	420 (25)	407 (29)	143 (25)	230 (15)	103 (4)	213 (11)	78 (8)	170 (9)	144 (11)
NGC3516	< 38	< 256	75 (24)	< 67	58 (14)	< 28	11 (3)	31 (6)	< 28	< 27	< 37

Table 4—Continued

Source ID	6.2 μm	7.4 μm	7.6 μm	7.8 μm	8.3 μm	8.6 μm	11.2 μm	11.3 μm	12.0 μm	12.6 μm	17.0 μm
M+0-29-23	409 (23)	787 (69)	487 (22)	538 (25)	202 (14)	300 (12)	112 (4)	305 (8)	138 (6)	281 (14)	193 (13)
NGC3660	57 (15)	201 (47)	<64	175 (23)	45 (10)	36 (8)	23 (2)	27 (5)	21 (6)	43 (6)	<32
NGC3982	258 (32)	480 (110)	443 (46)	352 (52)	122 (33)	218 (12)	102 (4)	187 (10)	67 (10)	130 (13)	153 (11)
NGC4051	139 (10)	<176	260 (20)	214 (22)	77 (14)	96 (10)	66 (5)	171 (12)	75 (10)	143 (9)	133 (16)
UGC7064	122 (16)	<254	229 (26)	134 (21)	44 (11)	132 (9)	35 (4)	110 (12)	46 (10)	70 (6)	66 (10)
NGC4151	55 (14)	<465	287 (55)	472 (64)	276 (47)	235 (41)	45 (14)	<78	<77	168 (40)	<208
MRK766	102 (13)	594 (48)	56 (17)	192 (19)	99 (14)	118 (10)	35 (4)	103 (8)	56 (9)	<40	150 (22)
NGC4388	233 (9)	440 (140)	393 (53)	451 (53)	134 (16)	186 (14)	82 (7)	350 (19)	180 (24)	270 (29)	244 (24)
NGC4501	<75	<197	79 (25)	102 (22)	<52	<37	36 (4)	124 (9)	58 (12)	83 (10)	90 (7)
NGC4579	63 (11)	213 (41)	<43	55 (15)	<31	23 (6)	24 (2)	95 (4)	53 (7)	55 (10)	63 (5)
NGC4593	90 (10)	<171	145 (20)	170 (20)	76 (15)	72 (12)	30 (4)	94 (9)	27 (9)	58 (11)	<47
NGC4594	34 (10)	<172	<51	84 (20)	<33	<16	7 (2)	16 (3)	<10	<17	<7
TOL1238-364	335 (19)	550 (89)	399 (35)	394 (40)	94 (15)	221 (10)	97 (6)	324 (16)	168 (13)	253 (18)	<58
NGC4602	107 (11)	353 (64)	<74	145 (21)	<52	104 (14)	39 (3)	82 (6)	47 (8)	65 (8)	59 (6)
M-2-33-34	40 (7)	<229	76 (22)	56 (16)	<33	<33	24 (2)	67 (4)	25 (4)	55 (5)	57 (8)
NGC4941	36 (5)	173 (22)	35 (8)	<24	28 (4)	20 (2)	<9	40 (6)	30 (6)	26 (7)	<29
NGC4968	133 (9)	364 (41)	181 (17)	156 (11)	108 (16)	92 (12)	41 (4)	145 (9)	77 (9)	83 (9)	59 (16)
NGC5005	326 (22)	722 (76)	350 (29)	534 (34)	194 (29)	246 (17)	195 (10)	525 (27)	226 (13)	386 (28)	358 (13)
NGC5033	483 (28)	579 (94)	650 (39)	751 (44)	243 (27)	357 (12)	179 (6)	472 (16)	187 (12)	383 (18)	319 (15)
NGC5135	854 (26)	1150 (130)	1085 (38)	1205 (43)	387 (29)	645 (20)	276 (12)	691 (31)	349 (16)	638 (51)	368 (33)
M-6-30-15	30 (9)	223 (60)	<57	84 (15)	43 (9)	29 (6)	<10	61 (8)	44 (6)	25 (6)	<29
NGC5256	364 (23)	661 (62)	570 (18)	471 (22)	139 (11)	241 (8)	76 (4)	250 (12)	137 (13)	248 (24)	160 (16)
IC4329A	53 (14)	572 (70)	<92	141 (32)	168 (22)	98 (17)	<17	65 (14)	114 (15)	<66	<106
NGC5347	51 (10)	<180	<52	70 (15)	48 (9)	27 (7)	12 (3)	73 (6)	62 (7)	85 (11)	<34
NGC5506	161 (21)	<443	429 (50)	580 (41)	<92	82 (21)	<39	352 (38)	295 (49)	329 (42)	132 (34)
NGC5548	59 (8)	149 (39)	<41	65 (15)	<40	48 (12)	15 (3)	92 (6)	<26	68 (6)	<31
MRK817	71 (13)	234 (60)	97 (16)	147 (11)	<38	60 (10)	12 (3)	54 (7)	47 (8)	46 (8)	<37
NGC5929	41 (9)	<213	<77	<69	<33	<24	20 (3)	53 (7)	<17	25 (7)	<22
NGC5953	1030 (56)	1080 (200)	1437 (82)	1424 (96)	439 (56)	749 (22)	322 (17)	748 (44)	301 (21)	604 (48)	431 (36)
M-2-40-4	133 (12)	<291	282 (32)	193 (26)	37 (11)	121 (9)	50 (5)	186 (9)	69 (8)	145 (11)	57 (14)
F15480-0344	<37	<202	<67	75 (14)	<21	<17	22 (3)	47 (6)	38 (5)	30 (6)	<39
NGC6810	1238 (58)	1600 (170)	1600 (66)	1699 (80)	484 (37)	819 (25)	385 (19)	895 (49)	408 (20)	837 (55)	420 (64)
NGC6860	87 (11)	256 (62)	<63	134 (10)	56 (14)	63 (12)	16 (3)	100 (6)	36 (11)	62 (10)	57 (10)
NGC6890	134 (13)	<74	254 (27)	296 (30)	64 (12)	85 (10)	55 (4)	158 (11)	76 (6)	101 (8)	118 (12)
IC5063	<31	397 (73)	<114	129 (30)	<55	67 (15)	<17	106 (16)	118 (21)	85 (26)	<78

Table 4—Continued

Source ID	6.2 μm	7.4 μm	7.6 μm	7.8 μm	8.3 μm	8.6 μm	11.2 μm	11.3 μm	12.0 μm	12.6 μm	17.0 μm
UGC11680	59 (14)	< 252 ⋯	< 85 ⋯	125 (23)	66 (12)	< 28 ⋯	16 (3)	49 (7)	28 (6)	19 (5)	33 (8)
NGC7130	630 (20)	1070 (120)	752 (39)	907 (30)	319 (16)	486 (12)	188 (6)	500 (16)	248 (13)	445 (24)	258 (20)
NGC7172	262 (23)	898 (81)	210 (55)	452 (62)	< 153 ⋯	< 47 ⋯	27 (4)	175 (12)	127 (16)	211 (11)	217 (14)
NGC7213	76 (11)	299 (72)	< 76 ⋯	90 (24)	< 43 ⋯	78 (11)	30 (4)	159 (10)	103 (7)	72 (11)	< 37 ⋯
NGC7314	25 (6)	< 120 ⋯	< 72 ⋯	53 (10)	< 24 ⋯	< 19 ⋯	< 8 ⋯	31 (5)	< 14 ⋯	< 19 ⋯	57 (6)
M-3-58-7	87 (9)	283 (32)	122 (17)	197 (11)	124 (12)	53 (10)	28 (3)	99 (6)	42 (6)	66 (7)	56 (14)
NGC7469	1209 (39)	1780 (130)	1447 (44)	1565 (32)	471 (20)	806 (17)	316 (12)	858 (31)	382 (19)	675 (37)	383 (56)
NGC7496	329 (19)	335 (59)	434 (18)	361 (17)	136 (17)	182 (15)	81 (4)	230 (11)	89 (28)	195 (26)	146 (11)
NGC7582	2042 (88)	2900 (270)	2860 (110)	3300 (130)	1162 (84)	1390 (46)	517 (27)	1625 (74)	935 (48)	1780 (110)	730 (58)
NGC7590	252 (22)	380 (100)	343 (32)	293 (30)	91 (21)	191 (13)	85 (6)	191 (14)	61 (15)	125 (8)	129 (10)
NGC7603	123 (12)	< 186 ⋯	100 (20)	177 (11)	64 (11)	59 (8)	44 (3)	138 (7)	84 (8)	108 (8)	72 (9)
NGC7674	230 (13)	248 (69)	398 (22)	375 (20)	113 (20)	167 (14)	63 (5)	195 (11)	85 (10)	152 (13)	126 (25)
CGCG381-051	111 (15)	215 (57)	114 (15)	112 (10)	< 32 ⋯	110 (8)	29 (3)	66 (7)	34 (7)	64 (8)	< 22 ⋯

Note. — Integrated fluxes are given in units of 10^{-17} W m^{-2}. Uncertainties (1σ) are listed in parentheses. Upper limits are 3σ.

Table 5.   PAH Feature EQWs

Source ID	6.2 μm	7.4 μm	7.6 μm	7.8 μm	8.3 μm	8.6 μm	11.2 μm	11.3 μm	12.0 μm	12.6 μm	17.0 μm
MRK335	< 32	< 167	< 48	102 (18)	71 (21)	56 (16)	< 14	50 (13)	71 (15)	91 (11)	< 65
MRK938	2700 (130)	5880 (590)	3150 (180)	3730 (160)	1620 (110)	1797 (82)	596 (17)	1429 (44)	622 (41)	1133 (48)	388 (45)
E12-G21	500 (51)	< 554	723 (50)	757 (50)	174 (35)	465 (27)	139 (15)	803 (42)	303 (36)	682 (74)	640 (54)
MRK348	< 44	362 (46)	< 67	181 (25)	< 66	104 (16)	25 (5)	96 (12)	< 52	44 (13)	< 85
NGC424	12 (3)	191 (29)	53 (13)	76 (15)	63 (10)	38 (8)	< 10	26 (6)	30 (7)	< 31	< 41
NGC526A	33 (9)	381 (53)	66 (14)	72 (22)	87 (19)	51 (13)	< 13	57 (11)	96 (11)	58 (11)	< 87
NGC513	613 (67)	< 1145	1330 (120)	900 (120)	< 337	632 (79)	541 (18)	832 (55)	445 (72)	648 (71)	804 (80)
F01475-0740	113 (26)	251 (81)	287 (27)	< 92	< 65	84 (16)	30 (5)	161 (11)	153 (15)	173 (16)	< 62
NGC931	57 (7)	< 146	62 (19)	102 (23)	< 44	35 (11)	17 (4)	124 (8)	41 (10)	44 (10)	56 (18)
NGC1056	2340 (120)	2630 (350)	3580 (170)	2880 (190)	920 (140)	1943 (50)	998 (56)	1960 (150)	821 (56)	1745 (86)	1230 (110)
NGC1097	1734 (75)	2370 (210)	2530 (130)	2880 (160)	970 (120)	1490 (33)	668 (31)	1794 (82)	1010 (48)	2280 (180)	650 (50)
NGC1125	767 (71)	2620 (490)	1270 (160)	1220 (130)	615 (55)	541 (41)	296 (16)	733 (40)	231 (32)	448 (30)	167 (25)
NGC1143-4	1342 (88)	1600 (190)	1940 (57)	1924 (49)	530 (28)	1009 (27)	563 (28)	1688 (73)	642 (25)	1121 (58)	812 (49)
M-2-8-39	< 87	< 599	< 167	< 158	< 98	72 (21)	< 14	< 41	< 55	36 (11)	256 (42)
NGC1194	30 (7)	< 155	131 (20)	115 (21)	< 61	< 52	< 19	121 (16)	98 (26)	64 (13)	164 (25)
NGC1241	750 (100)	2910 (810)	< 919	1730 (340)	590 (170)	600 (120)	285 (26)	725 (72)	275 (82)	372 (38)	661 (70)
NGC1320	125 (11)	< 290	246 (33)	229 (37)	74 (20)	116 (16)	48 (4)	121 (10)	32 (9)	101 (13)	< 53
NGC1365	1235 (58)	1420 (190)	1600 (84)	1830 (160)	566 (63)	817 (28)	341 (17)	1016 (46)	482 (25)	985 (68)	446 (30)
NGC1386	68 (12)	< 216	223 (23)	230 (25)	73 (14)	91 (9)	50 (5)	264 (10)	115 (15)	149 (14)	185 (27)
F03450+0055	42 (8)	431 (63)	< 42	127 (13)	144 (12)	51 (10)	< 10	< 27	64 (12)	75 (12)	< 71
NGC1566	303 (26)	640 (120)	500 (40)	720 (47)	268 (35)	321 (24)	270 (12)	788 (31)	307 (21)	534 (30)	719 (33)
F04385-0828	33 (6)	< 84	66 (12)	< 33	< 32	< 26	< 13	137 (12)	105 (14)	128 (12)	< 55
NGC1667	2450 (180)	3890 (590)	3000 (240)	3550 (280)	820 (200)	1950 (130)	745 (37)	1975 (97)	731 (83)	1693 (81)	1300 (140)
E33-G2	< 55	550 (88)	< 84	< 82	102 (15)	72 (13)	< 16	68 (15)	< 71	...	< 59
M-5-13-17	327 (25)	< 718	309 (75)	466 (77)	148 (41)	352 (32)	182 (9)	337 (23)	120 (22)	163 (20)	199 (28)
MRK6	34 (8)	< 209	85 (22)	< 41	< 58	< 56	23 (4)	< 32	< 32	< 48	146 (27)
MRK79	24 (4)	363 (80)	< 69	74 (17)	71 (12)	< 26	< 12	72 (10)	60 (11)	81 (16)	< 89
NGC2639	470 (120)	< 2493	1220 (280)	1150 (280)	< 715	< 559	378 (39)	990 (110)	< 465	540 (120)	1220 (200)
MRK704	< 22	< 86	< 37	63 (16)	< 38	< 26	< 8	< 22	< 31	< 34	< 61
NGC2992	382 (28)	940 (130)	588 (39)	723 (47)	275 (26)	368 (19)	152 (7)	420 (18)	175 (15)	223 (32)	345 (32)
MRK1239	15 (4)	112 (26)	63 (13)	66 (8)	47 (7)	39 (6)	15 (3)	34 (8)	42 (8)	64 (9)	< 47
NGC3079	3950 (180)	9210 (750)	7650 (340)	9310 (450)	3330 (350)	3400 (200)	1417 (72)	5170 (190)	2180 (110)	3600 (190)	2540 (120)
NGC3227	294 (14)	562 (60)	370 (30)	517 (22)	174 (15)	259 (12)	137 (10)	447 (27)	195 (15)	245 (20)	340 (28)
NGC3511	2980 (210)	3040 (670)	4020 (240)	3850 (270)	1320 (230)	2100 (130)	1006 (41)	2070 (110)	769 (83)	1742 (94)	1940 (140)
NGC3516	< 29	< 243	73 (23)	< 68	64 (15)	< 32	15 (4)	43 (7)	< 43	< 42	< 63

Table 5—Continued

Source ID	6.2 μm	7.4 μm	7.6 μm	7.8 μm	8.3 μm	8.6 μm	11.2 μm	11.3 μm	12.0 μm	12.6 μm	17.0 μm
M+0-29-23	1314 (74)	2530 (220)	1569 (71)	1740 (81)	666 (48)	1023 (40)	465 (15)	1247 (33)	487 (22)	920 (44)	634 (43)
NGC3660	710 (190)	2800 (650)	< 893	2460 (320)	630 (140)	480 (110)	311 (26)	361 (73)	309 (90)	688 (96)	< 481
NGC3982	1850 (230)	3360 (770)	3020 (320)	2350 (350)	780 (210)	1382 (77)	636 (25)	1166 (65)	412 (62)	796 (81)	924 (67)
NGC4051	99 (7)	< 134	201 (15)	168 (17)	63 (12)	79 (8)	58 (4)	153 (11)	71 (9)	144 (8)	155 (19)
UGC7064	521 (68)	< 1222	1120 (120)	670 (100)	227 (56)	685 (48)	172 (21)	544 (58)	235 (52)	365 (34)	328 (48)
NGC4151	13 (3)	< 123	77 (15)	129 (17)	76 (13)	65 (11)	10 (3)	< 18	< 19	43 (10)	< 57
MRK766	114 (15)	855 (69)	83 (25)	294 (29)	157 (22)	187 (16)	46 (4)	137 (10)	75 (12)	< 52	178 (26)
NGC4388	184 (7)	360 (110)	330 (44)	388 (46)	125 (14)	188 (15)	109 (8)	458 (24)	201 (27)	272 (29)	217 (22)
NGC4501	< 225	< 856	360 (110)	490 (110)	< 273	< 205	335 (34)	1168 (87)	560 (120)	850 (110)	1580 (130)
NGC4579	124 (22)	630 (120)	< 131	179 (48)	111 (21)	83 (21)	104 (7)	429 (20)	293 (41)	338 (64)	455 (33)
NGC4593	69 (7)	< 152	132 (19)	157 (18)	72 (14)	69 (11)	32 (4)	101 (10)	33 (10)	75 (14)	< 82
NGC4594	26 (8)	< 240	< 76	139 (33)	< 64	< 33	26 (6)	65 (13)	< 48	< 100	< 71
TOL1238-364	453 (26)	750 (120)	548 (49)	545 (55)	133 (21)	316 (14)	115 (7)	384 (18)	191 (15)	276 (19)	< 50
NGC4602	1230 (130)	4570 (830)	< 955	1870 (280)	< 659	1310 (170)	506 (32)	1052 (71)	620 (110)	880 (110)	826 (80)
M-2-33-34	177 (31)	< 1134	380 (110)	291 (84)	< 180	< 183	151 (11)	422 (26)	156 (25)	345 (32)	334 (48)
NGC4941	158 (20)	930 (120)	190 (41)	< 134	168 (26)	120 (12)	< 55	256 (36)	185 (34)	160 (40)	< 153
NGC4968	220 (14)	648 (73)	325 (31)	283 (21)	199 (29)	170 (22)	64 (5)	226 (14)	117 (14)	123 (13)	81 (22)
NGC5005	373 (25)	1120 (120)	564 (46)	908 (57)	368 (55)	504 (34)	717 (36)	1928 (98)	809 (47)	1410 (100)	1860 (65)
NGC5033	844 (49)	1220 (200)	1402 (85)	1663 (98)	568 (62)	870 (30)	638 (21)	1693 (58)	680 (45)	1443 (69)	1684 (80)
NGC5135	1194 (37)	1690 (180)	1604 (56)	1802 (64)	593 (45)	1010 (31)	475 (20)	1177 (52)	549 (26)	946 (76)	437 (39)
M-6-30-15	25 (7)	237 (64)	< 62	95 (17)	51 (11)	35 (7)	< 12	78 (9)	61 (8)	37 (8)	< 49
NGC5256	2160 (140)	4000 (380)	3440 (110)	2830 (130)	841 (65)	1478 (49)	493 (28)	1587 (73)	730 (68)	1180 (110)	573 (59)
IC4329A	14 (4)	198 (24)	< 32	52 (12)	65 (8)	38 (6)	< 6	26 (6)	50 (6)	< 30	< 56
NGC5347	97 (19)	< 324	< 93	124 (27)	84 (16)	47 (12)	19 (4)	116 (10)	98 (11)	137 (18)	< 57
NGC5506	30 (3)	< 104	104 (12)	147 (10)	< 26	26 (6)	< 20	181 (20)	132 (22)	138 (18)	70 (18)
NGC5548	92 (12)	267 (70)	< 74	121 (27)	< 77	92 (23)	25 (5)	160 (11)	< 47	133 (12)	< 64
MRK817	96 (18)	400 (100)	167 (28)	259 (19)	< 67	103 (18)	17 (4)	82 (11)	77 (13)	78 (13)	< 59
NGC5929	480 (100)	< 2941	< 1085	< 995	< 500	< 371	417 (58)	1100 (150)	< 367	570 (150)	< 483
NGC5953	3170 (170)	3310 (610)	4370 (250)	4270 (290)	1290 (160)	2184 (65)	1000 (51)	2330 (140)	942 (67)	1920 (150)	1420 (120)
M-2-40-4	89 (8)	< 210	208 (23)	146 (20)	30 (9)	103 (7)	56 (5)	210 (11)	80 (9)	181 (14)	94 (22)
F15480-0344	< 90	< 521	< 175	200 (36)	< 57	< 48	50 (5)	110 (14)	95 (12)	75 (14)	< 89
NGC6810	1485 (70)	1960 (210)	1955 (81)	2063 (97)	580 (44)	974 (30)	408 (20)	944 (52)	425 (21)	861 (56)	310 (48)
NGC6860	98 (13)	374 (90)	< 95	213 (16)	96 (24)	112 (21)	34 (5)	214 (12)	84 (27)	154 (24)	169 (31)
NGC6890	280 (27)	< 164	588 (64)	701 (72)	159 (31)	215 (24)	164 (13)	474 (32)	231 (18)	312 (24)	381 (39)
IC5063	< 13	160 (30)	< 46	53 (12)	< 23	29 (6)	< 8	49 (7)	54 (9)	38 (12)	< 35

Table 5—Continued

Source ID	6.2 μm	7.4 μm	7.6 μm	7.8 μm	8.3 μm	8.6 μm	11.2 μm	11.3 μm	12.0 μm	12.6 μm	17.0 μm
UGC11680	219 (54)	< 1114 ⋯	< 386 ⋯	590 (110)	326 (59)	< 139 ⋯	83 (15)	258 (35)	157 (35)	113 (31)	207 (49)
NGC7130	1614 (52)	2740 (310)	1914 (99)	2285 (75)	784 (39)	1176 (30)	363 (12)	957 (30)	442 (22)	747 (40)	332 (26)
NGC7172	278 (24)	1210 (110)	290 (76)	642 (88)	< 238 ⋯	< 84 ⋯	126 (17)	780 (52)	350 (43)	470 (25)	853 (56)
NGC7213	87 (13)	510 (120)	< 134 ⋯	170 (45)	< 87 ⋯	156 (23)	44 (5)	242 (15)	193 (12)	151 (24)	< 77 ⋯
NGC7314	116 (25)	< 638 ⋯	< 387 ⋯	286 (57)	< 132 ⋯	< 105 ⋯	< 40 ⋯	159 (28)	< 68 ⋯	< 85 ⋯	285 (28)
M-3-58-7	92 (9)	387 (44)	171 (24)	284 (16)	184 (18)	78 (14)	43 (4)	153 (8)	68 (9)	112 (12)	99 (24)
NGC7469	733 (24)	1142 (83)	934 (29)	1019 (21)	309 (13)	526 (11)	178 (6)	483 (18)	214 (11)	370 (20)	160 (24)
NGC7496	1533 (87)	1270 (220)	1600 (68)	1282 (59)	455 (58)	597 (49)	241 (13)	679 (34)	249 (77)	516 (69)	281 (21)
NGC7582	757 (33)	1240 (120)	1248 (47)	1484 (57)	563 (41)	731 (24)	369 (20)	1137 (52)	549 (28)	943 (56)	345 (28)
NGC7590	1590 (140)	2910 (780)	2690 (250)	2320 (230)	730 (170)	1530 (100)	693 (47)	1580 (120)	530 (130)	1156 (69)	1490 (110)
NGC7603	83 (8)	< 166 ⋯	93 (18)	173 (11)	69 (12)	65 (9)	69 (5)	220 (11)	159 (14)	229 (17)	242 (30)
NGC7674	184 (10)	225 (63)	367 (20)	356 (19)	113 (20)	173 (15)	61 (4)	191 (11)	83 (9)	151 (13)	124 (25)
CGCG381-051	750 (100)	1330 (360)	698 (89)	674 (62)	< 178 ⋯	571 (43)	120 (11)	279 (29)	163 (32)	327 (42)	< 85 ⋯

Note. — PAH equivalent widths are given in units of nm. Uncertainties (1σ) are listed in parentheses. Upper limits are 3σ.

Table 6.   H$_2$ Line Fluxes

Source ID	S(7)		S(6)		S(5)		S(4)		S(3)		S(2)		S(1)		S(0)	
MRK335	< 72	⋯	< 88	⋯	< 64	⋯	< 55	⋯	53	(12)	21	(6)	17	(5)	< 18	⋯
MRK938	160	(32)	< 205	⋯	151	(22)	249	(57)	128	(13)	143	(22)	195	(22)	< 153	⋯
E12-G21	55	(15)	< 132	⋯	< 67	⋯	< 83	⋯	40	(11)	< 34	⋯	< 21	⋯	< 22	⋯
MRK348	< 79	⋯	< 85	⋯	62	(17)	< 74	⋯	< 26	⋯	< 28	⋯	< 39	⋯	23	(6)
NGC424	< 96	⋯	< 76	⋯	< 68	⋯	< 177	⋯	< 55	⋯	< 54	⋯	< 35	⋯	< 56	⋯
NGC526A	76	(19)	40	(11)	73	(10)	55	(11)	29	(9)	22	(4)	33	(9)	< 28	⋯
NGC513	< 94	⋯	< 135	⋯	< 75	⋯	< 137	⋯	81	(18)	< 47	⋯	41	(9)	< 26	⋯
F01475-0740	< 111	⋯	< 54	⋯	47	(11)	< 49	⋯	< 24	⋯	29	(8)	< 23	⋯	< 43	⋯
NGC931	< 130	⋯	< 78	⋯	65	(20)	< 112	⋯	< 47	⋯	< 25	⋯	< 29	⋯	< 42	⋯
NGC1056	< 144	⋯	< 196	⋯	< 97	⋯	< 197	⋯	85	(17)	< 51	⋯	< 47	⋯	< 32	⋯
NGC1097	< 235	⋯	< 595	⋯	186	(43)	< 772	⋯	319	(31)	< 503	⋯	374	(36)	< 82	⋯
NGC1125	< 81	⋯	< 79	⋯	< 52	⋯	< 44	⋯	< 22	⋯	< 30	⋯	< 21	⋯	< 52	⋯
NGC1143-4	< 47	⋯	< 160	⋯	< 41	⋯	< 55	⋯	62	(7)	51	(13)	91	(7)	< 45	⋯
M-2-8-39	< 150	⋯	65	(20)	< 81	⋯	82	(26)	< 39	⋯	< 22	⋯	< 35	⋯	20	(6)
NGC1194	< 57	⋯	< 54	⋯	< 50	⋯	< 67	⋯	< 23	⋯	< 40	⋯	< 25	⋯	< 31	⋯
NGC1241	< 171	⋯	< 92	⋯	< 78	⋯	< 144	⋯	< 34	⋯	42	(9)	47	(8)	< 18	⋯
NGC1320	< 96	⋯	< 68	⋯	< 51	⋯	< 83	⋯	< 41	⋯	< 30	⋯	< 27	⋯	< 56	⋯
NGC1365	< 259	⋯	< 1070	⋯	< 351	⋯	< 1203	⋯	382	(49)	< 465	⋯	< 377	⋯	< 342	⋯
NGC1386	< 181	⋯	< 89	⋯	82	(24)	< 75	⋯	82	(21)	96	(19)	< 54	⋯	< 88	⋯
F03450+0055	60	(15)	< 51	⋯	< 62	⋯	< 37	⋯	< 25	⋯	23	(7)	< 26	⋯	< 25	⋯
NGC1566	< 80	⋯	< 85	⋯	< 35	⋯	< 78	⋯	121	(11)	77	(10)	149	(10)	< 22	⋯
F04385-0828	< 90	⋯	66	(19)	< 76	⋯	< 82	⋯	< 34	⋯	55	(15)	< 38	⋯	< 58	⋯
NGC1667	< 148	⋯	< 188	⋯	< 82	⋯	< 192	⋯	< 60	⋯	73	(15)	79	(15)	< 20	⋯
E33-G2	< 103	⋯	< 96	⋯	< 60	⋯	< 70	⋯	< 40	⋯	46	(9)	20	(6)	< 20	⋯
M-5-13-17	< 90	⋯	< 60	⋯	< 51	⋯	< 52	⋯	37	(9)	< 26	⋯	< 22	⋯	< 29	⋯
MRK6	< 77	⋯	< 43	⋯	71	(16)	< 40	⋯	59	(10)	27	(7)	< 35	⋯	< 52	⋯
MRK79	< 105	⋯	< 58	⋯	< 69	⋯	< 62	⋯	61	(17)	< 25	⋯	54	(13)	< 28	⋯
NGC2639	< 103	⋯	< 100	⋯	< 100	⋯	< 121	⋯	< 74	⋯	< 41	⋯	< 25	⋯	17	(5)
MRK704	< 94	⋯	< 54	⋯	< 48	⋯	< 68	⋯	< 39	⋯	< 27	⋯	< 23	⋯	< 26	⋯
NGC2992	< 176	⋯	< 154	⋯	100	(24)	< 129	⋯	108	(13)	< 106	⋯	187	(26)	< 76	⋯
MRK1239	< 86	⋯	< 102	⋯	< 90	⋯	< 39	⋯	< 53	⋯	< 31	⋯	< 35	⋯	< 51	⋯
NGC3079	< 254	⋯	< 612	⋯	666	(45)	< 770	⋯	365	(21)	450	(110)	506	(39)	< 179	⋯
NGC3227	< 93	⋯	< 97	⋯	240	(38)	134	(42)	197	(24)	112	(24)	277	(31)	< 87	⋯
NGC3511	< 166	⋯	< 140	⋯	< 86	⋯	< 126	⋯	< 64	⋯	< 34	⋯	29	(9)	26	(7)
NGC3516	< 100	⋯	< 94	⋯	78	(22)	105	(29)	< 49	⋯	42	(11)	< 31	⋯	< 49	⋯
M+0-29-23	< 71	⋯	< 142	⋯	98	(24)	< 114	⋯	34	(10)	56	(11)	70	(13)	< 52	⋯
NGC3660	108	(28)	< 97	⋯	< 88	⋯	< 106	⋯	< 44	⋯	< 24	⋯	< 27	⋯	19	(4)
NGC3982	< 152	⋯	< 191	⋯	< 92	⋯	< 201	⋯	< 58	⋯	< 46	⋯	< 28	⋯	< 25	⋯
NGC4051	< 64	⋯	< 66	⋯	< 45	⋯	< 89	⋯	123	(18)	< 28	⋯	< 41	⋯	< 77	⋯
UGC7064	< 77	⋯	< 96	⋯	< 100	⋯	< 89	⋯	< 32	⋯	< 30	⋯	< 25	⋯	< 29	⋯
NGC4151	< 228	⋯	< 65	⋯	< 59	⋯	< 233	⋯	< 129	⋯	< 150	⋯	< 178	⋯	200	(60)
MRK766	< 108	⋯	< 89	⋯	40	(9)	< 71	⋯	< 28	⋯	< 49	⋯	< 56	⋯	< 71	⋯
NGC4388	< 199	⋯	57	(17)	121	(25)	< 210	⋯	143	(14)	172	(38)	135	(30)	< 127	⋯
NGC4501	< 121	⋯	< 146	⋯	83	(23)	177	(32)	129	(20)	76	(15)	192	(9)	16	(5)
NGC4579	< 70	⋯	87	(23)	191	(16)	115	(21)	290	(14)	115	(12)	201	(6)	< 12	⋯
NGC4593	< 76	⋯	< 61	⋯	64	(15)	< 81	⋯	55	(16)	< 22	⋯	59	(17)	< 52	⋯

Table 6—Continued

Source ID	S(7)		S(6)		S(5)		S(4)		S(3)		S(2)		S(1)		S(0)	
NGC4594	< 70	⋯	< 53	⋯	< 54	⋯	< 91	⋯	< 26	⋯	< 21	⋯	5	(1)	< 8	⋯
TOL1238-364	< 76	⋯	< 108	⋯	< 48	⋯	< 152	⋯	55	(16)	< 64	⋯	< 46	⋯	< 99	⋯
NGC4602	< 173	⋯	< 66	⋯	74	(24)	< 94	⋯	< 60	⋯	< 25	⋯	33	(7)	23	(6)
M-2-33-34	< 88	⋯	< 49	⋯	< 61	⋯	< 44	⋯	< 22	⋯	< 17	⋯	< 21	⋯	< 44	⋯
NGC4941	108	(11)	72	(7)	77	(8)	51	(8)	45	(10)	22	(6)	< 25	⋯	< 32	⋯
NGC4968	< 135	⋯	< 53	⋯	< 55	⋯	< 80	⋯	< 41	⋯	54	(11)	< 40	⋯	< 45	⋯
NGC5005	187	(52)	< 127	⋯	431	(28)	< 167	⋯	376	(21)	187	(36)	393	(15)	61	(19)
NGC5033	< 87	⋯	< 167	⋯	95	(24)	< 162	⋯	118	(11)	85	(18)	137	(13)	30	(10)
NGC5135	< 138	⋯	< 172	⋯	< 143	⋯	< 186	⋯	116	(19)	< 167	⋯	262	(29)	< 120	⋯
M-6-30-15	< 88	⋯	< 60	⋯	< 46	⋯	< 61	⋯	< 23	⋯	< 19	⋯	< 25	⋯	< 29	⋯
NGC5256	< 121	⋯	< 139	⋯	< 75	⋯	< 94	⋯	96	(12)	90	(25)	87	(14)	< 81	⋯
IC4329A	< 181	⋯	< 106	⋯	< 47	⋯	< 159	⋯	< 64	⋯	< 44	⋯	< 90	⋯	< 91	⋯
NGC5347	< 65	⋯	< 51	⋯	59	(16)	64	(16)	< 38	⋯	< 31	⋯	< 29	⋯	< 37	⋯
NGC5506	< 332	⋯	< 127	⋯	< 58	⋯	< 157	⋯	< 77	⋯	166	(45)	< 55	⋯	< 167	⋯
NGC5548	< 51	⋯	67	(17)	44	(14)	< 70	⋯	71	(17)	44	(10)	44	(14)	< 37	⋯
MRK817	< 155	⋯	< 97	⋯	< 64	⋯	< 56	⋯	< 63	⋯	< 33	⋯	< 32	⋯	< 52	⋯
NGC5929	< 88	⋯	61	(16)	57	(16)	< 85	⋯	74	(11)	34	(7)	61	(6)	< 12	⋯
NGC5953	< 131	⋯	< 329	⋯	< 90	⋯	< 361	⋯	112	(25)	< 125	⋯	141	(31)	< 51	⋯
M-2-40-4	< 95	⋯	< 64	⋯	< 60	⋯	101	(26)	< 32	⋯	62	(13)	< 34	⋯	< 43	⋯
F15480-0344	< 66	⋯	< 74	⋯	52	(7)	< 57	⋯	< 31	⋯	< 16	⋯	46	(11)	29	(9)
NGC6810	< 177	⋯	< 352	⋯	< 146	⋯	< 290	⋯	168	(18)	< 143	⋯	359	(55)	< 178	⋯
NGC6860	< 126	⋯	< 56	⋯	69	(20)	< 44	⋯	< 33	⋯	< 40	⋯	41	(12)	< 21	⋯
NGC6890	< 95	⋯	< 77	⋯	< 62	⋯	< 116	⋯	< 31	⋯	< 32	⋯	46	(13)	< 39	⋯
IC5063	< 95	⋯	< 61	⋯	88	(16)	< 138	⋯	< 67	⋯	< 58	⋯	< 67	⋯	< 129	⋯
UGC11680	< 126	⋯	< 85	⋯	< 90	⋯	< 106	⋯	< 57	⋯	< 18	⋯	23	(7)	< 19	⋯
NGC7130	< 71	⋯	< 111	⋯	< 114	⋯	134	(37)	117	(19)	94	(24)	122	(24)	< 137	⋯
NGC7172	< 80	⋯	< 135	⋯	72	(15)	< 273	⋯	47	(4)	56	(17)	51	(12)	< 36	⋯
NGC7213	< 122	⋯	< 85	⋯	< 71	⋯	< 73	⋯	88	(20)	< 27	⋯	98	(13)	< 30	⋯
NGC7314	77	(12)	44	(6)	62	(7)	42	(12)	26	(4)	18	(3)	15	(4)	< 27	⋯
M-3-58-7	56	(17)	< 61	⋯	< 71	⋯	74	(22)	< 32	⋯	< 27	⋯	< 35	⋯	< 53	⋯
NGC7469	< 149	⋯	< 248	⋯	< 143	⋯	< 119	⋯	252	(31)	184	(36)	189	(60)	< 342	⋯
NGC7496	< 78	⋯	< 109	⋯	99	(26)	99	(25)	< 160	⋯	238	(35)	62	(17)	< 75	⋯
NGC7582	< 228	⋯	< 548	⋯	< 145	⋯	< 495	⋯	242	(31)	350	(100)	310	(60)	< 341	⋯
NGC7590	< 179	⋯	< 128	⋯	< 99	⋯	< 124	⋯	< 59	⋯	< 40	⋯	38	(8)	27	(6)
NGC7603	71	(11)	< 66	⋯	< 55	⋯	< 62	⋯	57	(14)	31	(9)	40	(12)	22	(6)
NGC7674	< 87	⋯	< 78	⋯	74	(22)	< 107	⋯	93	(16)	< 49	⋯	< 64	⋯	< 101	⋯
CGCG381-051	< 75	⋯	< 98	⋯	76	(24)	64	(20)	22	(6)	< 27	⋯	33	(11)	< 31	⋯

Note. — Integrated fluxes are given in units of 10^{-18} W m^{-2}. Uncertainties (1σ) are listed in parentheses. Upper limits are 3σ. The line wavelengths for the S(7) – S(0) series are 5.512, 6.159, 6.859, 8.004, 9.656, 12.329, 17.063, and 28.171 μm, respectively.

Table 7.   H$_2$ EQWs

Source ID	S(7)		S(6)		S(5)		S(4)		S(3)		S(2)		S(1)		S(0)	
MRK335	< 7	⋯	< 10	⋯	< 9	⋯	< 10	⋯	9	(2)	6	(2)	6	(2)	< 15	⋯
MRK938	50	(10)	< 74	⋯	60	(9)	98	(22)	77	(8)	37	(6)	34	(4)	< 11	⋯
E12-G21	12	(3)	< 31	⋯	< 18	⋯	< 24	⋯	14	(4)	< 16	⋯	< 14	⋯	< 19	⋯
MRK348	< 8	⋯	< 10	⋯	8	(2)	< 12	⋯	< 5	⋯	< 5	⋯	< 7	⋯	10	(3)
NGC424	< 3	⋯	< 2	⋯	< 2	⋯	< 7	⋯	< 2	⋯	< 3	⋯	< 2	⋯	< 11	⋯
NGC526A	9	(2)	6	(2)	12	(2)	11	(2)	5	(2)	5	(1)	9	(3)	< 27	⋯
NGC513	< 28	⋯	< 44	⋯	< 26	⋯	< 54	⋯	38	(9)	< 28	⋯	30	(7)	< 23	⋯
F01475-0740	< 35	⋯	< 16	⋯	13	(3)	< 14	⋯	< 6	⋯	8	(2)	< 5	⋯	< 18	⋯
NGC931	< 8	⋯	< 6	⋯	5	(2)	< 10	⋯	< 5	⋯	< 3	⋯	< 5	⋯	< 12	⋯
NGC1056	< 45	⋯	< 70	⋯	< 37	⋯	< 80	⋯	37	(8)	< 27	⋯	< 28	⋯	< 15	⋯
NGC1097	< 16	⋯	< 46	⋯	16	(4)	< 70	⋯	28	(3)	< 61	⋯	44	(4)	< 7	⋯
NGC1125	< 30	⋯	< 35	⋯	< 28	⋯	< 28	⋯	< 19	⋯	< 12	⋯	< 6	⋯	< 13	⋯
NGC1143-4	< 15	⋯	< 58	⋯	< 16	⋯	< 23	⋯	45	(5)	29	(7)	52	(4)	< 20	⋯
M-2-8-39	< 53	⋯	22	(7)	< 26	⋯	26	(8)	< 12	⋯	< 6	⋯	< 11	⋯	17	(5)
NGC1194	< 5	⋯	< 5	⋯	< 5	⋯	< 8	⋯	< 7	⋯	< 8	⋯	< 6	⋯	< 14	⋯
NGC1241	< 90	⋯	< 59	⋯	< 61	⋯	< 133	⋯	< 36	⋯	35	(8)	39	(6)	< 16	⋯
NGC1320	< 10	⋯	< 7	⋯	< 6	⋯	< 10	⋯	< 5	⋯	< 4	⋯	< 4	⋯	< 13	⋯
NGC1365	< 8	⋯	< 35	⋯	< 12	⋯	< 39	⋯	16	(2)	< 18	⋯	< 14	⋯	< 9	⋯
NGC1386	< 14	⋯	< 7	⋯	7	(2)	< 6	⋯	12	(3)	10	(2)	< 7	⋯	< 15	⋯
F03450+0055	7	(2)	< 7	⋯	< 10	⋯	< 7	⋯	< 4	⋯	5	(1)	< 6	⋯	< 13	⋯
NGC1566	< 13	⋯	< 16	⋯	< 7	⋯	< 19	⋯	36	(3)	28	(4)	68	(4)	< 13	⋯
F04385-0828	< 6	⋯	4	(1)	< 5	⋯	< 6	⋯	< 6	⋯	6	(2)	< 5	⋯	< 9	⋯
NGC1667	< 75	⋯	< 117	⋯	< 56	⋯	< 131	⋯	< 41	⋯	53	(11)	65	(12)	< 14	⋯
E33-G2	< 13	⋯	< 13	⋯	< 9	⋯	< 13	⋯	< 7	⋯	10	(2)	6	(2)	< 14	⋯
M-5-13-17	< 24	⋯	< 17	⋯	< 16	⋯	< 17	⋯	13	(3)	< 9	⋯	< 7	⋯	< 14	⋯
MRK6	< 7	⋯	< 5	⋯	10	(2)	< 7	⋯	12	(2)	6	(2)	< 7	⋯	< 22	⋯
MRK79	< 8	⋯	< 5	⋯	< 7	⋯	< 7	⋯	8	(2)	< 4	⋯	10	(3)	< 10	⋯
NGC2639	< 46	⋯	< 66	⋯	< 90	⋯	< 129	⋯	< 84	⋯	< 54	⋯	< 50	⋯	41	(12)
MRK704	< 7	⋯	< 4	⋯	< 4	⋯	< 7	⋯	< 4	⋯	< 4	⋯	< 5	⋯	< 15	⋯
NGC2992	< 16	⋯	< 16	⋯	12	(3)	< 18	⋯	14	(2)	< 13	⋯	24	(3)	< 14	⋯
MRK1239	< 3	⋯	< 4	⋯	< 4	⋯	< 2	⋯	< 3	⋯	< 2	⋯	< 4	⋯	< 15	⋯
NGC3079	< 27	⋯	< 89	⋯	133	(9)	< 184	⋯	216	(12)	100	(25)	135	(10)	< 19	⋯
NGC3227	< 8	⋯	< 9	⋯	23	(4)	14	(4)	22	(3)	13	(3)	29	(3)	< 13	⋯
NGC3511	< 125	⋯	< 127	⋯	< 85	⋯	< 118	⋯	< 60	⋯	< 34	⋯	39	(12)	34	(9)
NGC3516	< 7	⋯	< 7	⋯	7	(2)	11	(3)	< 6	⋯	6	(2)	< 5	⋯	< 15	⋯
M+0-29-23	< 22	⋯	< 46	⋯	32	(8)	< 37	⋯	16	(5)	19	(4)	23	(4)	< 13	⋯
NGC3660	116	(30)	< 119	⋯	< 118	⋯	< 149	⋯	< 53	⋯	< 37	⋯	< 41	⋯	28	(6)
NGC3982	< 94	⋯	< 136	⋯	< 67	⋯	< 132	⋯	< 38	⋯	< 28	⋯	< 17	⋯	< 15	⋯
NGC4051	< 4	⋯	< 5	⋯	< 3	⋯	< 7	⋯	10	(2)	< 3	⋯	< 5	⋯	< 16	⋯
UGC7064	< 30	⋯	< 41	⋯	< 46	⋯	< 45	⋯	< 15	⋯	< 16	⋯	< 12	⋯	< 20	⋯
NGC4151	< 5	⋯	< 2	⋯	< 2	⋯	< 6	⋯	< 3	⋯	< 4	⋯	< 5	⋯	14	(4)
MRK766	< 10	⋯	< 10	⋯	5	(1)	< 11	⋯	< 4	⋯	< 7	⋯	< 7	⋯	< 12	⋯
NGC4388	< 16	⋯	5	(1)	10	(2)	< 18	⋯	24	(2)	18	(4)	12	(3)	< 12	⋯
NGC4501	< 25	⋯	< 41	⋯	32	(9)	88	(16)	102	(16)	75	(15)	338	(15)	39	(12)
NGC4579	< 10	⋯	16	(4)	48	(4)	39	(7)	91	(4)	67	(7)	146	(4)	< 12	⋯
NGC4593	< 5	⋯	< 5	⋯	5	(1)	< 8	⋯	5	(2)	< 3	⋯	10	(3)	< 16	⋯

Table 7—Continued

Source ID	S(7)		S(6)		S(5)		S(4)		S(3)		S(2)		S(1)		S(0)	
NGC4594	< 4	$\cdots$	< 4	$\cdots$	< 6	$\cdots$	< 16	$\cdots$	< 7	$\cdots$	< 11	$\cdots$	5	(2)	< 17	$\cdots$
TOL1238-364	< 10	$\cdots$	< 15	$\cdots$	< 7	$\cdots$	< 21	$\cdots$	8	(2)	< 7	$\cdots$	< 4	$\cdots$	< 11	$\cdots$
NGC4602	< 156	$\cdots$	< 74	$\cdots$	95	(30)	< 120	$\cdots$	< 75	$\cdots$	< 33	$\cdots$	46	(10)	30	(8)
M-2-33-34	< 36	$\cdots$	< 22	$\cdots$	< 29	$\cdots$	< 23	$\cdots$	< 13	$\cdots$	< 11	$\cdots$	< 12	$\cdots$	< 34	$\cdots$
NGC4941	41	(4)	31	(3)	38	(4)	30	(5)	29	(7)	13	(3)	< 13	$\cdots$	< 23	$\cdots$
NGC4968	< 22	$\cdots$	< 9	$\cdots$	< 10	$\cdots$	< 15	$\cdots$	< 7	$\cdots$	8	(2)	< 6	$\cdots$	< 12	$\cdots$
NGC5005	17	(5)	< 14	$\cdots$	59	(4)	< 30	$\cdots$	121	(7)	68	(13)	205	(8)	20	(6)
NGC5033	< 12	$\cdots$	< 29	$\cdots$	19	(5)	< 36	$\cdots$	37	(3)	31	(7)	73	(7)	16	(5)
NGC5135	< 18	$\cdots$	< 24	$\cdots$	< 21	$\cdots$	< 28	$\cdots$	21	(3)	< 26	$\cdots$	31	(3)	< 11	$\cdots$
M-6-30-15	< 6	$\cdots$	< 5	$\cdots$	< 4	$\cdots$	< 7	$\cdots$	< 3	$\cdots$	< 3	$\cdots$	< 4	$\cdots$	< 10	$\cdots$
NGC5256	< 66	$\cdots$	< 82	$\cdots$	< 46	$\cdots$	< 56	$\cdots$	76	(9)	45	(12)	31	(5)	< 18	$\cdots$
IC4329A	< 4	$\cdots$	< 3	$\cdots$	< 2	$\cdots$	< 6	$\cdots$	< 2	$\cdots$	< 2	$\cdots$	< 5	$\cdots$	< 12	$\cdots$
NGC5347	< 13	$\cdots$	< 10	$\cdots$	11	(3)	11	(3)	< 7	$\cdots$	< 5	$\cdots$	< 5	$\cdots$	< 11	$\cdots$
NGC5506	< 5	$\cdots$	< 2	$\cdots$	< 1	$\cdots$	< 4	$\cdots$	< 5	$\cdots$	7	(2)	< 3	$\cdots$	< 12	$\cdots$
NGC5548	< 7	$\cdots$	11	(3)	7	(2)	< 13	$\cdots$	12	(3)	8	(2)	9	(3)	< 16	$\cdots$
MRK817	< 18	$\cdots$	< 13	$\cdots$	< 10	$\cdots$	< 10	$\cdots$	< 9	$\cdots$	< 6	$\cdots$	< 5	$\cdots$	< 12	$\cdots$
NGC5929	< 83	$\cdots$	70	(19)	74	(21)	< 126	$\cdots$	133	(20)	75	(16)	135	(14)	< 23	$\cdots$
NGC5953	< 35	$\cdots$	< 100	$\cdots$	< 28	$\cdots$	< 107	$\cdots$	34	(8)	< 39	$\cdots$	47	(10)	< 12	$\cdots$
M-2-40-4	< 6	$\cdots$	< 4	$\cdots$	< 4	$\cdots$	8	(2)	< 4	$\cdots$	7	(2)	< 6	$\cdots$	< 11	$\cdots$
F15480-0344	< 16	$\cdots$	< 18	$\cdots$	13	(2)	< 15	$\cdots$	< 8	$\cdots$	< 4	$\cdots$	10	(3)	11	(3)
NGC6810	< 19	$\cdots$	< 42	$\cdots$	< 18	$\cdots$	< 35	$\cdots$	19	(2)	< 15	$\cdots$	27	(4)	< 14	$\cdots$
NGC6860	< 13	$\cdots$	< 6	$\cdots$	9	(3)	< 7	$\cdots$	< 6	$\cdots$	< 10	$\cdots$	12	(4)	< 16	$\cdots$
NGC6890	< 19	$\cdots$	< 16	$\cdots$	< 14	$\cdots$	< 28	$\cdots$	< 9	$\cdots$	< 10	$\cdots$	15	(4)	< 17	$\cdots$
IC5063	< 4	$\cdots$	< 3	$\cdots$	4	(1)	< 6	$\cdots$	< 4	$\cdots$	< 3	$\cdots$	< 3	$\cdots$	< 9	$\cdots$
UGC11680	< 42	$\cdots$	< 31	$\cdots$	< 37	$\cdots$	< 51	$\cdots$	< 27	$\cdots$	< 10	$\cdots$	15	(5)	< 21	$\cdots$
NGC7130	< 17	$\cdots$	< 28	$\cdots$	< 29	$\cdots$	34	(9)	27	(4)	16	(4)	16	(3)	< 14	$\cdots$
NGC7172	< 6	$\cdots$	< 14	$\cdots$	9	(2)	< 40	$\cdots$	36	(3)	14	(4)	20	(5)	< 13	$\cdots$
NGC7213	< 10	$\cdots$	< 9	$\cdots$	< 10	$\cdots$	< 14	$\cdots$	12	(3)	< 5	$\cdots$	21	(3)	< 17	$\cdots$
NGC7314	30	(5)	20	(3)	32	(3)	23	(6)	17	(3)	8	(2)	8	(2)	< 20	$\cdots$
M-3-58-7	5	(2)	< 6	$\cdots$	< 9	$\cdots$	11	(3)	< 4	$\cdots$	< 5	$\cdots$	< 6	$\cdots$	< 14	$\cdots$
NGC7469	< 9	$\cdots$	< 15	$\cdots$	< 9	$\cdots$	< 8	$\cdots$	15	(2)	10	(2)	8	(3)	< 14	$\cdots$
NGC7496	< 37	$\cdots$	< 51	$\cdots$	41	(11)	34	(9)	< 52	$\cdots$	65	(10)	12	(3)	< 10	$\cdots$
NGC7582	< 7	$\cdots$	< 20	$\cdots$	< 6	$\cdots$	< 23	$\cdots$	23	(3)	20	(6)	15	(3)	< 11	$\cdots$
NGC7590	< 83	$\cdots$	< 78	$\cdots$	< 73	$\cdots$	< 99	$\cdots$	< 46	$\cdots$	< 36	$\cdots$	45	(9)	30	(7)
NGC7603	4	(1)	< 4	$\cdots$	< 4	$\cdots$	< 6	$\cdots$	7	(2)	6	(2)	13	(4)	18	(5)
NGC7674	< 7	$\cdots$	< 6	$\cdots$	6	(2)	< 10	$\cdots$	10	(2)	< 5	$\cdots$	< 6	$\cdots$	< 15	$\cdots$
CGCG381-051	< 55	$\cdots$	< 67	$\cdots$	48	(15)	38	(12)	9	(2)	< 13	$\cdots$	13	(4)	< 14	$\cdots$

Note. — H_2 equivalent widths are given in units of nm. Uncertainties (1σ) are listed in parentheses. Upper limits are 3σ. The line wavelengths for the S(7) – S(0) series are 5.512, 6.159, 6.859, 8.004, 9.656, 12.329, 17.063, and 28.171 μm, respectively.

Table 8.   Fine Structure Line Fluxes

Source ID	[OIV] 25.91 μm	[SiII] 34.815 μm	[NeII] 12.813 μm	[NeIII] 15.555 μm	[NeV] 14.322 μm	[SIII] 18.713 μm	[SIII] 33.48 μm	[SIV] 10.511 μm	[ArII] 6.985 μm
MRK335	32 (7)	<80 ...	24 (5)	44 (9)	<19 ...	<32 ...	<87 ...	27 (8)	<70 ...
MRK938	<126 ...	<796 ...	563 (25)	<82 ...	<56 ...	52 (15)	<895 ...	<55 ...	209 (30)
E12-G21	202 (13)	169 (52)	140 (19)	61 (8)	52 (9)	90 (9)	<174 ...	47 (12)	<69 ...
MRK348	179 (14)	131 (35)	131 (10)	178 (16)	54 (11)	42 (12)	<110 ...	62 (9)	69 (14)
NGC424	145 (29)	<244 ...	73 (22)	136 (30)	<58 ...	<53 ...	<244 ...	<54 ...	<68 ...
NGC526A	203 (10)	<155 ...	51 (11)	135 (13)	<25 ...	56 (10)	66 (19)	61 (12)	57 (10)
NGC513	110 (8)	308 (36)	237 (15)	93 (9)	24 (8)	100 (8)	217 (38)	<48 ...	<94 ...
F01475-0740	<65 ...	<182 ...	157 (9)	96 (10)	21 (6)	47 (11)	<185 ...	<30 ...	62 (19)
NGC931	365 (23)	<124 ...	67 (12)	141 (17)	78 (15)	<37 ...	167 (48)	156 (20)	<56 ...
NGC1056	52 (10)	715 (67)	503 (20)	127 (22)	<30 ...	218 (14)	490 (32)	<83 ...	94 (30)
NGC1097	<97 ...	2900 (240)	3200 (170)	90 (25)	<183 ...	593 (31)	1030 (250)	<170 ...	1281 (57)
NGC1125	252 (21)	223 (55)	311 (9)	243 (11)	77 (10)	136 (10)	220 (53)	107 (8)	95 (17)
NGC1143-4	74 (11)	614 (78)	499 (14)	110 (9)	26 (7)	267 (8)	454 (75)	30 (9)	216 (16)
M-2-8-39	138 (13)	64 (19)	66 (6)	134 (17)	62 (11)	<36 ...	<48 ...	44 (8)	<90 ...
NGC1194	115 (13)	<63 ...	31 (9)	94 (15)	41 (11)	<41 ...	<90 ...	62 (8)	101 (17)
NGC1241	69 (7)	208 (24)	139 (7)	107 (10)	<19 ...	43 (6)	138 (30)	65 (17)	<80 ...
NGC1320	347 (23)	<127 ...	87 (11)	71 (16)	69 (16)	<46 ...	<134 ...	96 (12)	<49 ...
NGC1365	1000 (160)	6520 (790)	5000 (220)	440 (110)	255 (74)	1669 (85)	2800 (500)	446 (48)	2130 (140)
NGC1386	891 (52)	450 (140)	192 (17)	419 (23)	277 (26)	196 (25)	<199 ...	285 (14)	156 (22)
F03450+0055	<25 ...	<78 ...	<21 ...	37 (11)	<27 ...	<26 ...	<79 ...	<27 ...	<66 ...
NGC1566	78 (8)	194 (18)	168 (9)	86 (7)	<15 ...	64 (5)	100 (16)	30 (6)	61 (14)
F04385-0828	<60 ...	<301 ...	120 (13)	<50 ...	<38 ...	<38 ...	<316 ...	<22 ...	<81 ...
NGC1667	87 (8)	79 (21)	364 (14)	66 (15)	<24 ...	159 (12)	<68 ...	<54 ...	191 (31)
E33-G2	159 (11)	<77 ...	30 (8)	57 (11)	25 (7)	<34 ...	<83 ...	113 (15)	<54 ...
M-5-13-17	130 (12)	131 (24)	119 (7)	71 (9)	<25 ...	<26 ...	85 (25)	34 (10)	<59 ...
MRK6	302 (17)	334 (41)	240 (10)	463 (23)	75 (10)	140 (12)	165 (44)	172 (11)	113 (16)
MRK79	447 (18)	161 (43)	96 (14)	204 (14)	82 (13)	53 (13)	166 (47)	114 (12)	<77 ...
NGC2639	23 (6)	111 (20)	135 (11)	42 (11)	<20 ...	48 (9)	54 (13)	<57 ...	<96 ...
MRK704	102 (11)	53 (14)	<32 ...	75 (12)	<43 ...	<34 ...	<46 ...	<29 ...	<47 ...
NGC2992	1258 (40)	1090 (100)	657 (32)	756 (37)	249 (25)	419 (20)	710 (110)	344 (14)	276 (25)
MRK1239	83 (17)	<157 ...	66 (18)	118 (19)	<37 ...	<50 ...	<171 ...	<42 ...	<102 ...
NGC3079	311 (64)	2620 (260)	1860 (120)	232 (57)	<115 ...	155 (25)	610 (150)	112 (28)	589 (48)
NGC3227	573 (50)	740 (150)	752 (24)	619 (30)	135 (22)	253 (24)	<391 ...	268 (31)	294 (34)
NGC3511	<23 ...	402 (29)	248 (13)	<34 ...	<17 ...	95 (8)	151 (28)	<50 ...	<78 ...

Table 8—Continued

Source ID	[OIV] 25.91 μm	[SiII] 34.815 μm	[NeII] 12.813 μm	[NeIII] 15.555 μm	[NeV] 14.322 μm	[SIII] 18.713 μm	[SIII] 33.48 μm	[SIV] 10.511 μm	[ArII] 6.985 μm
NGC3516	591 (23)	147 (29)	65 (10)	189 (18)	72 (12)	81 (13)	160 (29)	159 (12)	< 72 ...
M+0-29-23	< 39 ...	446 (56)	407 (18)	71 (13)	< 28 ...	109 (12)	< 186 ...	< 43 ...	150 (22)
NGC3660	41 (9)	74 (17)	51 (7)	38 (9)	< 16 ...	< 27 ...	< 62 ...	45 (11)	< 87 ...
NGC3982	39 (8)	531 (34)	301 (16)	67 (15)	< 30 ...	133 (10)	238 (33)	74 (16)	130 (34)
NGC4051	297 (32)	295 (94)	184 (16)	107 (18)	< 28 ...	85 (20)	< 152 ...	64 (16)	88 (20)
UGC7064	117 (13)	< 214 ...	117 (8)	57 (9)	47 (10)	75 (11)	< 220 ...	< 36 ...	< 90 ...
NGC4151	1860 (110)	1230 (300)	1459 (62)	1528 (82)	353 (58)	761 (68)	< 623 ...	892 (58)	441 (42)
MRK766	387 (29)	< 181 ...	210 (15)	231 (37)	121 (24)	98 (24)	265 (66)	92 (14)	48 (8)
NGC4388	3401 (74)	1200 (210)	845 (35)	1201 (83)	482 (32)	526 (26)	730 (150)	695 (35)	270 (23)
NGC4501	30 (5)	185 (16)	104 (13)	87 (8)	< 20 ...	28 (7)	38 (12)	< 55 ...	< 68 ...
NGC4579	68 (5)	371 (24)	196 (12)	99 (4)	< 8 ...	44 (4)	58 (11)	26 (5)	173 (15)
NGC4593	80 (17)	< 117 ...	75 (11)	< 42 ...	< 37 ...	< 32 ...	< 123 ...	< 30 ...	< 68 ...
NGC4594	35 (2)	271 (21)	129 (7)	144 (6)	< 6 ...	56 (4)	94 (23)	< 19 ...	91 (22)
TOL1238-364	< 131 ...	< 438 ...	553 (21)	268 (31)	< 41 ...	170 (23)	< 413 ...	93 (12)	167 (25)
NGC4602	< 16 ...	184 (21)	127 (9)	< 13 ...	< 13 ...	72 (8)	123 (22)	28 (8)	82 (26)
M-2-33-34	692 (32)	352 (24)	138 (7)	320 (12)	131 (9)	137 (9)	233 (27)	218 (8)	75 (19)
NGC4941	203 (12)	180 (25)	160 (9)	202 (8)	43 (8)	93 (9)	< 72 ...	135 (12)	71 (8)
NGC4968	293 (24)	188 (42)	247 (12)	252 (17)	95 (15)	64 (15)	161 (38)	107 (13)	61 (19)
NGC5005	127 (22)	920 (100)	615 (36)	183 (14)	< 39 ...	59 (11)	< 163 ...	< 67 ...	169 (29)
NGC5033	179 (8)	949 (48)	534 (23)	140 (13)	33 (7)	148 (7)	255 (54)	< 45 ...	192 (24)
NGC5135	680 (50)	1450 (170)	1421 (64)	620 (33)	130 (26)	391 (21)	960 (190)	260 (21)	596 (53)
M-6-30-15	123 (15)	< 79 ...	60 (10)	< 34 ...	< 26 ...	< 37 ...	< 87 ...	66 (14)	45 (10)
NGC5256	636 (32)	720 (86)	616 (29)	398 (17)	63 (18)	265 (14)	452 (79)	156 (12)	218 (27)
IC4329A	1233 (71)	302 (93)	219 (33)	512 (51)	365 (46)	< 78 ...	380 (97)	308 (43)	59 (15)
NGC5347	< 50 ...	< 113 ...	71 (13)	< 35 ...	< 23 ...	< 34 ...	< 128 ...	31 (9)	100 (17)
NGC5506	2324 (99)	1170 (170)	826 (53)	1192 (81)	343 (41)	501 (35)	700 (180)	772 (40)	331 (37)
NGC5548	80 (11)	< 129 ...	99 (8)	97 (12)	< 30 ...	48 (11)	137 ...	< 42 ...	< 53 ...
MRK817	< 45 ...	< 114 ...	76 (10)	70 (13)	< 40 ...	< 39 ...	< 128 ...	< 42 ...	< 60 ...
NGC5929	53 (6)	205 (23)	99 (9)	93 (9)	< 17 ...	64 (7)	82 (20)	< 37 ...	68 (17)
NGC5953	233 (18)	1690 (120)	1303 (60)	227 (35)	52 (14)	449 (17)	700 (120)	< 104 ...	347 (33)
M-2-40-4	158 (20)	222 (57)	204 (13)	150 (18)	60 (15)	52 (13)	< 184 ...	< 45 ...	< 63 ...
F15480-0344	426 (17)	< 115 ...	80 (8)	161 (17)	133 (15)	< 37 ...	< 120 ...	96 (12)	< 48 ...
NGC6810	< 148 ...	1620 (200)	1479 (68)	< 119 ...	< 59 ...	567 (32)	810 (190)	< 79 ...	522 (48)
NGC6860	110 (9)	118 (33)	77 (9)	81 (9)	35 (10)	33 (8)	< 100 ...	< 28 ...	< 72 ...

Table 8—Continued

Source ID	[OIV] 25.91 μm	[SiII] 34.815 μm	[NeII] 12.813 μm	[NeIII] 15.555 μm	[NeV] 14.322 μm	[SIII] 18.713 μm	[SIII] 33.48 μm	[SIV] 10.511 μm	[ArII] 6.985 μm
NGC6890	88 (14)	207 (30)	185 (11)	61 (13)	33 (8)	92 (10)	145 (23)	< 56 :	63 (17)
IC5063	904 (90)	< 713 :	213 (34)	620 (46)	< 106 :	155 (43)	< 721 :	529 (34)	78 (16)
UGC11680	23 (6)	< 88 :	55 (7)	55 (9)	< 20 :	< 18 :	< 49 :	< 48 :	< 95 :
NGC7130	124 (37)	890 (140)	1010 (28)	308 (27)	111 (18)	232 (19)	680 (160)	107 (15)	415 (50)
NGC7172	549 (17)	612 (46)	211 (14)	184 (15)	72 (14)	89 (10)	308 (38)	89 (10)	141 (34)
NGC7213	< 33 :	207 (31)	227 (13)	129 (10)	< 23 :	36 (11)	< 99 :	< 51 :	116 (17)
NGC7314	521 (20)	114 (26)	74 (8)	246 (16)	108 (8)	89 (8)	94 (20)	188 (10)	68 (7)
M-3-58-7	< 58 :	< 169 :	94 (9)	73 (13)	57 (13)	< 35 :	< 188 :	39 (10)	74 (23)
NGC7469	< 187 :	1660 (340)	2005 (46)	242 (75)	200 (44)	638 (51)	1590 (360)	172 (26)	824 (61)
NGC7496	< 73 :	< 486 :	424 (32)	34 (11)	< 26 :	232 (15)	377 (96)	48 (15)	215 (22)
NGC7582	2210 (150)	2790 (650)	2840 (130)	1153 (70)	274 (67)	904 (55)	1700 (540)	458 (36)	1057 (62)
NGC7590	39 (6)	492 (20)	174 (10)	59 (12)	< 25 :	107 (9)	242 (23)	< 59 :	< 112 :
NGC7603	21 (6)	130 (32)	127 (9)	70 (11)	< 23 :	< 23 :	64 (17)	< 30 :	< 61 :
NGC7674	492 (40)	< 298 :	287 (15)	380 (24)	181 (22)	175 (21)	< 313 :	156 (15)	179 (26)
CGCG381-051	< 41 :	127 (36)	184 (11)	< 28 :	18 (5)	102 (11)	< 115 :	< 23 :	86 (27)

Note. — Integrated fluxes are given in units of 10^{-18} W m^{-2}. Uncertainties (1σ) are listed in parentheses. Upper limits are 3σ.

Table 9. Fine Structure Line EQWs

Table 9. Fine Structure Line EQWs

Source ID	[OIV] 25.91 μm	[SiII] 34.815 μm	[NeII] 12.813 μm	[NeIII] 15.555 μm	[NeV] 14.322 μm	[SIII] 18.713 μm	[SIII] 33.48 μm	[SIV] 10.511 μm	[ArII] 6.985 μm
MRK335	22 (5)	< 101 ···	7 (2)	15 (3)	< 6	< 12	< 102 ···	5 (2)	< 9 ···
MRK938	< 9 ···	< 46 ···	125 (6)	< 13 ···	< 10	8 (2)	< 53 ···	< 30 ···	83 (12)
E12-G21	170 (11)	158 (49)	68 (9)	36 (5)	28 (5)	64 (6)	< 163 ···	18 (5)	< 18 ···
MRK348	65 (5)	83 (22)	24 (2)	33 (3)	10 (2)	8 (3)	< 64 ···	12 (2)	9 (2)
NGC424	23 (5)	< 70 ···	4 (1)	8 (2)	< 3	< 4 ···	< 65 ···	< 2 ···	< 2 ···
NGC526A	148 (7)	< 290 ···	11 (3)	35 (3)	< 6	18 (3)	108 (31)	10 (2)	9 (2)
NGC513	94 (7)	256 (30)	149 (9)	66 (7)	16 (5)	75 (6)	184 (32)	< 24 ···	< 33 ···
F01475-0740	< 23 ···	< 100 ···	41 (2)	24 (3)	5 (2)	11 (3)	< 96 ···	< 6 ···	17 (5)
NGC931	89 (6)	< 48 ···	8 (2)	20 (2)	10 (2)	< 6 ···	61 (18)	16 (2)	< 4 ···
NGC1056	25 (5)	272 (26)	278 (11)	77 (13)	< 17	127 (8)	192 (12)	< 38 ···	36 (12)
NGC1097	< 8 ···	196 (16)	412 (22)	11 (3)	< 24	65 (3)	72 (17)	< 16 ···	108 (5)
NGC1125	62 (5)	57 (14)	115 (4)	72 (3)	24 (3)	39 (3)	56 (14)	79 (6)	53 (10)
NGC1143-4	33 (5)	228 (29)	270 (7)	58 (5)	13 (4)	147 (5)	176 (29)	22 (7)	84 (6)
M-2-8-39	96 (9)	91 (27)	18 (2)	39 (5)	17 (3)	< 12 ···	< 61 ···	12 (2)	< 28 ···
NGC1194	45 (5)	< 36 ···	5 (2)	20 (3)	7 (2)	< 11 ···	< 50 ···	16 (2)	10 (2)
NGC1241	60 (6)	180 (21)	112 (6)	83 (8)	< 15	36 (5)	120 (26)	66 (17)	< 64 ···
NGC1320	75 (5)	< 39 ···	11 (2)	10 (2)	9 (2)	< 7 ···	< 39 ···	12 (1)	< 5 ···
NGC1365	26 (4)	144 (18)	189 (8)	16 (4)	9 (3)	58 (3)	64 (11)	18 (2)	70 (5)
NGC1386	142 (8)	83 (25)	19 (2)	47 (3)	28 (3)	27 (4)	< 35 ···	39 (2)	12 (2)
F03450+0055	< 11 ···	< 66 ···	< 4 ···	8 (3)	< 6	< 6 ···	< 61 ···	< 4 ···	< 10 ···
NGC1566	45 (5)	115 (11)	63 (4)	36 (3)	< 5	30 (2)	59 (9)	9 (2)	12 (3)
F04385-0828	< 8 ···	< 54 ···	12 (1)	< 5 ···	< 4	< 5 ···	< 55 ···	< 3 ···	< 5 ···
NGC1667	63 (6)	43 (11)	270 (11)	53 (12)	< 19	129 (9)	< 42 ···	< 37 ···	131 (21)
E33-G2	92 (7)	< 76 ···	7 (2)	14 (3)	6 (2)	< 10 ···	< 77 ···	21 (3)	< 8 ···
M-5-13-17	55 (5)	77 (14)	41 (3)	23 (3)	< 8	< 8 ···	48 (14)	11 (3)	< 18 ···
MRK6	110 (6)	192 (24)	53 (2)	100 (5)	16 (2)	29 (3)	90 (24)	32 (2)	16 (2)
MRK79	138 (5)	72 (19)	15 (2)	36 (3)	14 (2)	11 (3)	71 (20)	14 (2)	< 7 ···
NGC2639	54 (13)	239 (43)	189 (15)	76 (19)	< 32	104 (20)	119 (28)	< 66 ···	< 87 ···
MRK704	49 (5)	52 (14)	< 4 ···	13 (2)	< 7	< 8 ···	< 41 ···	< 3 ···	< 4 ···
NGC2992	230 (7)	200 (19)	77 (4)	88 (4)	28 (3)	57 (3)	132 (20)	44 (2)	34 (3)
MRK1239	20 (4)	< 64 ···	5 (2)	12 (2)	< 3	< 6 ···	< 65 ···	< 2 ···	< 4 ···
NGC3079	39 (8)	166 (16)	352 (22)	44 (11)	< 19	44 (7)	42 (11)	61 (15)	120 (10)
NGC3227	76 (7)	112 (23)	85 (3)	65 (3)	14 (2)	26 (3)	< 59 ···	30 (4)	27 (3)
NGC3511	< 31 ···	489 (35)	257 (13)	< 42 ···	< 19	132 (11)	188 (35)	< 48 ···	< 76 ···

Table 9—Continued

Source ID	[OIV] 25.91 μm	[SiII] 34.815 μm	[NeII] 12.813 μm	[NeIII] 15.555 μm	[NeV] 14.322 μm	[SIII] 18.713 μm	[SIII] 33.48 μm	[SIV] 10.511 μm	[ArII] 6.985 μm
NGC3516	165 (6)	58 (11)	10 (2)	32 (3)	12 (2)	14 (2)	61 (11)	21 (2)	< 6 ...
M+0-29-23	< 10 ...	105 (13)	130 (6)	21 (4)	< 8 ...	35 (4)	< 44 ...	< 20 ...	48 (7)
NGC3660	60 (13)	105 (24)	83 (11)	62 (14)	< 27 ...	< 40 ...	< 88 ...	56 (13)	< 118 ...
NGC3982	23 (5)	303 (19)	184 (10)	40 (9)	< 18 ...	78 (6)	139 (19)	47 (10)	94 (25)
NGC4051	56 (6)	79 (25)	18 (2)	12 (2)	< 3 ...	10 (3)	< 39 ...	5 (1)	6 (2)
UGC7064	76 (9)	< 170 ...	61 (4)	28 (5)	24 (5)	38 (6)	< 170 ...	< 17 ...	< 41 ...
NGC4151	108 (6)	119 (29)	38 (2)	42 (2)	9 (2)	23 (2)	< 56 ...	20 (1)	11 (1)
MRK766	62 (5)	< 35 ...	27 (2)	27 (4)	15 (3)	12 (3)	51 (13)	12 (2)	6 (1)
NGC4388	305 (7)	138 (24)	82 (4)	104 (7)	42 (3)	45 (2)	81 (17)	106 (5)	21 (2)
NGC4501	68 (12)	387 (34)	109 (14)	127 (12)	< 24 ...	55 (15)	84 (27)	< 49 ...	< 26 ...
NGC4579	69 (5)	350 (23)	123 (8)	72 (3)	< 5 ...	34 (3)	56 (11)	9 (2)	44 (4)
NGC4593	22 (5)	< 44 ...	10 (2)	< 6 ...	< 5 ...	< 6 ...	< 45 ...	< 2 ...	< 5 ...
NGC4594	70 (5)	471 (36)	81 (4)	144 (6)	< 5 ...	72 (5)	170 (41)	< 5 ...	10 (3)
TOL1238-364	< 13 ...	< 60 ...	59 (2)	24 (3)	< 4 ...	14 (2)	< 55 ...	11 (2)	22 (3)
NGC4602	< 21 ...	249 (29)	173 (12)	< 17 ...	< 18 ...	98 (11)	165 (29)	35 (10)	105 (34)
M-2-33-34	508 (23)	297 (20)	86 (5)	190 (7)	79 (5)	82 (5)	196 (23)	135 (5)	35 (9)
NGC4941	133 (8)	153 (21)	95 (6)	109 (4)	24 (5)	49 (5)	< 59 ...	87 (8)	35 (4)
NGC4968	67 (6)	62 (14)	36 (2)	35 (2)	13 (2)	9 (2)	51 (12)	17 (2)	10 (3)
NGC5005	47 (8)	204 (23)	226 (13)	83 (7)	< 15 ...	31 (6)	< 38 ...	< 24 ...	23 (4)
NGC5033	99 (5)	438 (22)	204 (9)	66 (6)	14 (3)	82 (4)	122 (26)	< 15 ...	38 (5)
NGC5135	61 (5)	115 (14)	207 (9)	76 (4)	17 (4)	43 (2)	78 (16)	48 (4)	85 (8)
M-6-30-15	38 (5)	< 40 ...	9 (1)	< 5 ...	< 4 ...	< 6 ...	< 41 ...	7 (2)	4 (1)
NGC5256	147 (8)	133 (16)	283 (14)	144 (6)	24 (7)	87 (5)	86 (15)	119 (9)	133 (16)
IC4329A	140 (8)	63 (20)	10 (2)	26 (3)	17 (2)	< 4 ...	74 (19)	12 (2)	1 (1)
NGC5347	< 13 ...	< 52 ...	11 (2)	< 5 ...	< 3 ...	< 6 ...	< 54 ...	5 (1)	18 (3)
NGC5506	151 (6)	96 (14)	34 (2)	56 (4)	15 (2)	28 (2)	56 (14)	45 (2)	7 (1)
NGC5548	29 (4)	< 77 ...	19 (2)	20 (3)	< 6 ...	10 (3)	< 78 ...	< 7 ...	< 9 ...
MRK817	< 9 ...	< 31 ...	13 (2)	11 (2)	< 7 ...	< 6 ...	< 33 ...	< 6 ...	< 9 ...
NGC5929	102 (12)	338 (38)	224 (21)	212 (21)	< 40 ...	134 (14)	139 (35)	< 72 ...	89 (23)
NGC5953	56 (4)	344 (25)	417 (19)	76 (12)	17 (5)	139 (5)	149 (26)	< 32 ...	109 (10)
M-2-40-4	36 (5)	61 (16)	25 (2)	23 (3)	8 (2)	9 (2)	< 50 ...	< 5 ...	< 4 ...
F15480-0344	146 (6)	< 56 ...	20 (2)	38 (4)	32 (4)	< 8 ...	< 56 ...	22 (3)	< 12 ...
NGC6810	< 11 ...	130 (16)	151 (7)	< 10 ...	< 5 ...	39 (2)	65 (15)	< 8 ...	64 (6)
NGC6860	69 (6)	122 (34)	19 (2)	22 (3)	9 (3)	11 (3)	< 98 ...	< 5 ...	< 9 ...

Table 9—Continued

Source ID	[OIV] 25.91 μm	[SiII] 34.815 μm	[NeII] 12.813 μm	[NeIII] 15.555 μm	[NeV] 14.322 μm	[SIII] 18.713 μm	[SIII] 33.48 μm	[SIV] 10.511 μm	[ArII] 6.985 μm
NGC6890	36 (6)	95 (14)	57 (3)	19 (4)	10 (3)	30 (3)	67 (11)	< 16 …	13 (4)
IC5063	55 (6)	< 62 …	9 (2)	27 (2)	< 4 …	7 (2)	< 59 …	26 (2)	3 (1)
UGC11680	22 (6)	< 125 …	32 (4)	33 (6)	< 12 …	< 12 …	< 67 …	< 23 …	< 39 …
NGC7130	12 (4)	79 (13)	166 (5)	42 (4)	16 (3)	28 (2)	62 (14)	22 (3)	107 (13)
NGC7172	198 (6)	191 (14)	45 (3)	50 (4)	16 (3)	38 (4)	99 (12)	66 (7)	18 (4)
NGC7213	< 16 …	173 (26)	49 (3)	29 (2)	< 5 …	8 (3)	< 77 …	< 6 …	17 (3)
NGC7314	357 (14)	90 (20)	33 (4)	110 (7)	47 (4)	48 (5)	75 (15)	108 (6)	35 (3)
M-3-58-7	< 13 …	< 51 …	16 (2)	12 (2)	10 (2)	< 6 …	< 55 …	5 (1)	9 (3)
NGC7469	< 7 …	66 (14)	109 (3)	11 (3)	9 (2)	25 (2)	64 (15)	9 (2)	51 (4)
NGC7496	< 10 …	< 62 …	110 (8)	7 (2)	< 6 …	40 (3)	49 (12)	15 (5)	88 (9)
NGC7582	72 (5)	77 (18)	146 (7)	52 (3)	12 (3)	41 (3)	48 (15)	39 (3)	43 (3)
NGC7590	45 (7)	504 (21)	164 (9)	68 (14)	< 26 …	127 (11)	253 (24)	< 46 …	< 83 …
NGC7603	14 (4)	133 (33)	27 (2)	21 (3)	< 6 …	< 8 …	64 (16)	< 3 …	< 5 …
NGC7674	67 (6)	< 53 …	28 (2)	37 (2)	17 (2)	18 (2)	< 54 …	15 (2)	15 (2)
CGCG381-051	< 16 …	71 (20)	96 (6)	< 12 …	8 (2)	37 (4)	< 60 …	< 9 …	54 (17)

Note. — Equivalent widths are given in units of nm. Uncertainties (1σ) are listed in parentheses. Upper limits are 3σ. Uncertainties (1σ) are listed in parentheses. Upper limits are 3σ.

Table 10. Dust Opacities and MIPS Aperture Corrections determined by PAHFIT

Source ID (1)	Model (2)	τ_{10} (3)		Ap. Corr. (4)	
MRK335	Screen	0.10	(0.07)	1.00	$\cdots$
MRK938	Screen	0.91	(0.03)	1.27	(0.02)
E12-G21	Mixed	1.21	(0.26)	1.00	$\cdots$
MRK348	Screen	0.22	(0.08)	1.66	(0.06)
NGC424	$\cdots$	0.00	$\cdots$	1.14	(0.07)
NGC526A	$\cdots$	0.00	$\cdots$	1.81	$\cdots$
NGC513	Screen	0.24	(0.02)	1.23	(0.02)
F01475-0740	Screen	0.09	(0.10)	1.00	$\cdots$
NGC931	$\cdots$	0.00	$\cdots$	1.24	(0.03)
NGC1056	$\cdots$	0.00	$\cdots$	1.38	(0.02)
NGC1097	Screen	0.04	(0.08)	1.81	$\cdots$
NGC1125	Mixed	1.79	(0.53)	1.40	(0.05)
NGC1143-4	Screen	0.70	(0.02)	1.00	$\cdots$
M-2-8-39	Mixed	4.01	(0.52)	1.03	(0.04)
NGC1194	Screen	2.35	(0.06)	1.14	(0.08)
NGC1241	Mixed	0.31	(0.09)	1.81	$\cdots$
NGC1320	Screen	0.69	(0.13)	1.24	(0.05)
NGC1365	Mixed	0.83	(0.07)	1.30	(0.02)
NGC1386	Mixed	9.41	(1.44)	1.23	(0.06)
F03450+0055	Screen	0.58	(0.11)	$\cdots$	$\cdots$
NGC1566	$\cdots$	0.00	$\cdots$	1.42	(0.07)
F04385-0828	Screen	1.67	(0.03)	1.14	(0.03)
NGC1667	Mixed	0.09	(0.08)	1.81	$\cdots$
E33-G2	Screen	0.34	(0.09)	1.46	(0.07)
M-5-13-17	Screen	0.01	(0.04)	1.22	(0.05)
MRK6	$\cdots$	0.00	(0.01)	1.00	$\cdots$
MRK79	Screen	0.41	(0.11)	1.14	(0.04)
NGC2639	$\cdots$	0.00	$\cdots$	1.81	$\cdots$
MRK704	Screen	1.07	(0.08)	1.07	(0.04)
NGC2992	Mixed	0.52	(0.11)	1.62	(0.05)
MRK1239	Screen	0.64	(0.17)	1.29	(0.05)
NGC3079	Mixed	6.19	(0.19)	$\cdots$	$\cdots$
NGC3227	$\cdots$	0.00	(0.05)	1.12	(0.02)
NGC3511	Mixed	0.20	(0.09)	1.81	$\cdots$
NGC3516	$\cdots$	0.00	$\cdots$	1.00	$\cdots$
M+0-29-23	Mixed	0.26	(0.17)	1.21	(0.09)
NGC3660	$\cdots$	0.00	$\cdots$	1.39	(0.11)
NGC3982	Mixed	0.19	(0.07)	1.81	$\cdots$
NGC4051	Mixed	1.33	(0.28)	1.33	(0.06)
UGC7064	$\cdots$	0.00	$\cdots$	1.63	(0.12)
NGC4151	$\cdots$	0.00	$\cdots$	1.01	(0.02)
MRK766	$\cdots$	0.00	$\cdots$	1.26	(0.04)
NGC4388	Mixed	3.32	(0.13)	1.55	(0.02)
NGC4501	Mixed	0.62	(0.10)	1.81	$\cdots$
NGC4579	$\cdots$	0.00	$\cdots$	1.24	(0.02)

Table 10—Continued

Source ID (1)	Model (2)	τ_{10} (3)		Ap. Corr. (4)	
NGC4593	Screen	0.35	(0.21)	1.65	(0.09)
NGC4594	$\cdots$	0.00	$\cdots$	1.00	$\cdots$
NGC4602	$\cdots$	0.00	(0.09)	1.81	$\cdots$
TOL1238-364	Mixed	1.34	(0.14)	1.14	(0.02)
M-2-33-34	Mixed	1.30	(0.07)	1.11	(0.03)
NGC4941	$\cdots$	0.00	$\cdots$	1.00	$\cdots$
NGC4968	Screen	0.17	(0.11)	1.06	(0.05)
NGC5005	Mixed	0.96	(0.06)	1.70	(0.04)
NGC5033	Mixed	0.54	(0.04)	1.00	$\cdots$
NGC5135	$\cdots$	0.00	$\cdots$	1.38	(0.08)
M-6-30-15	Mixed	1.50	(0.32)	1.00	$\cdots$
NGC5256	Mixed	1.17	(0.08)	1.25	(0.03)
IC4329A	$\cdots$	0.00	$\cdots$	1.00	$\cdots$
NGC5347	Screen	1.11	(0.19)	1.45	(0.08)
NGC5506	Screen	2.16	(0.04)	1.20	(0.03)
NGC5548	Screen	0.56	(0.11)	1.00	$\cdots$
MRK817	Screen	0.05	(0.07)	1.25	(0.05)
NGC5929	Mixed	0.08	(0.14)	1.81	$\cdots$
NGC5953	Screen	0.09	(0.02)	$\cdots$	$\cdots$
M-2-40-4	$\cdots$	0.00	$\cdots$	1.00	$\cdots$
F15480-0344	Screen	1.10	(0.09)	1.00	$\cdots$
NGC6810	Screen	0.02	(0.05)	1.31	(0.02)
NGC6860	$\cdots$	0.00	$\cdots$	1.00	$\cdots$
NGC6890	$\cdots$	0.00	$\cdots$	1.34	(0.03)
IC5063	Screen	0.74	(0.09)	1.00	$\cdots$
UGC11680	Mixed	0.30	(0.22)	1.05	(0.06)
NGC7130	Mixed	0.08	(0.04)	1.34	(0.02)
NGC7172	Screen	2.65	(0.04)	1.23	(0.04)
NGC7213	$\cdots$	0.00	$\cdots$	1.03	(0.06)
NGC7314	Screen	1.17	(0.15)	1.81	$\cdots$
M-3-58-7	$\cdots$	0.00	$\cdots$	1.00	$\cdots$
NGC7469	$\cdots$	0.00	$\cdots$	1.26	(0.02)
NGC7496	Mixed	0.24	(0.04)	1.35	(0.03)
NGC7582	Screen	1.39	(0.06)	1.22	(0.03)
NGC7590	$\cdots$	0.00	$\cdots$	1.81	$\cdots$
NGC7603	Screen	0.75	(0.23)	1.00	$\cdots$
NGC7674	Screen	0.97	(0.12)	1.21	(0.04)
CGCG381-051	$\cdots$	0.00	$\cdots$	1.44	(0.05)

Note. — (1) Source ID. (2) Dust extinction model: *Screen* models place all of the obscuring dust between the observer and the infrared continuum sources, and *Mixed* models assume that the obscuring dust is uniformly mixed with the infrared continuum sources. (3) Opacity of the obscuring dust component at 10 μm; this opacity affects all of the continuum model components except for the optically-thin hot dust component.

(4) The aperture correction for the MIPS-SED data; the MIPS-SED data need to be divided by this correction factor to reconcile the model fit with the smaller IRS and IRAC apertures. The correction factor was restricted to the range $1 - 1.81$ during the fitting procedure.

Table 11.   Silicate Strengths

Source ID	S_{10}		S_{18}	
MRK335	0.295	(0.028)	0.089	(0.009)
MRK938	−0.536	(0.046)	−0.268	(0.009)
E12-G21	0.036	(0.050)	−0.001	(0.019)
MRK348	−0.120	(0.022)	0.079	(0.011)
NGC424	0.111	(0.018)	0.085	(0.011)
NGC526A	0.252	(0.031)	0.098	(0.011)
NGC513	0.030	(0.067)	0.089	(0.095)
F01475-0740	0.143	(0.017)	0.163	(0.007)
NGC931	0.013	(0.010)	0.013	(0.007)
NGC1056	0.061	(0.030)	−0.050	(0.006)
NGC1097	0.207	(0.054)	0.015	(0.014)
NGC1125	−0.458	(0.070)	−0.114	(0.016)
NGC1143-4	−0.465	(0.042)	−0.144	(0.009)
M-2-8-39	0.014	(0.021)	0.080	(0.012)
NGC1194	−0.797	(0.010)	−0.145	(0.012)
NGC1241	−0.104	(0.066)	−0.053	(0.018)
NGC1320	−0.020	(0.028)	0.036	(0.010)
NGC1365	−0.169	(0.019)	−0.066	(0.012)
NGC1386	−0.534	(0.023)	−0.079	(0.013)
F03450+0055	0.328	(0.024)	0.068	(0.011)
NGC1566	−0.045	(0.020)	−0.015	(0.006)
F04385-0828	−0.769	(0.017)	−0.102	(0.011)
NGC1667	0.049	(0.058)	−0.091	(0.009)
E33-G2	0.109	(0.028)	0.013	(0.008)
M-5-13-17	0.007	(0.033)	−0.013	(0.013)
MRK6	0.137	(0.015)	0.197	(0.009)
MRK79	0.175	(0.034)	0.052	(0.014)
NGC2639	0.065	(0.088)	−0.002	(0.033)
MRK704	0.082	(0.020)	−0.016	(0.012)
NGC2992	0.042	(0.023)	−0.022	(0.010)
MRK1239	0.238	(0.021)	0.135	(0.014)
NGC3079	−0.923	(0.058)	−0.561	(0.012)
NGC3227	−0.032	(0.027)	0.052	(0.015)
NGC3511	0.015	(0.076)	−0.109	(0.012)
NGC3516	−0.007	(0.012)	0.052	(0.006)
M+0-29-23	−0.366	(0.029)	−0.187	(0.012)
NGC3660	0.315	(0.075)	0.194	(0.042)
NGC3982	−0.065	(0.056)	0.007	(0.014)
NGC4051	0.030	(0.018)	0.049	(0.011)
UGC7064	0.044	(0.040)	0.086	(0.018)
NGC4151	0.117	(0.009)	0.145	(0.016)
MRK766	0.167	(0.024)	0.038	(0.010)
NGC4388	−0.603	(0.015)	−0.089	(0.010)
NGC4501	−0.202	(0.065)	−0.122	(0.016)
NGC4579	0.400	(0.036)	0.105	(0.010)
NGC4593	0.229	(0.074)	0.080	(0.036)

Table 11—Continued

Source ID	S_{10}		S_{18}	
NGC4594	0.347	(0.016)	0.196	(0.013)
TOL1238-364	−0.127	(0.016)	0.033	(0.011)
NGC4602	0.095	(0.088)	−0.049	(0.011)
M-2-33-34	−0.039	(0.018)	−0.020	(0.006)
NGC4941	−0.026	(0.043)	−0.016	(0.015)
NGC4968	−0.071	(0.024)	0.056	(0.008)
NGC5005	−0.320	(0.037)	−0.108	(0.011)
NGC5033	−0.127	(0.026)	−0.108	(0.008)
NGC5135	−0.183	(0.016)	−0.056	(0.009)
M-6-30-15	0.143	(0.021)	0.049	(0.006)
NGC5256	−0.352	(0.070)	−0.137	(0.011)
IC4329A	0.114	(0.017)	0.042	(0.014)
NGC5347	−0.069	(0.021)	0.019	(0.007)
NGC5506	−0.703	(0.034)	−0.046	(0.070)
NGC5548	0.136	(0.021)	0.081	(0.007)
MRK817	0.271	(0.033)	0.071	(0.011)
NGC5929	−0.051	(0.146)	0.013	(0.032)
NGC5953	0.015	(0.027)	−0.079	(0.010)
M-2-40-4	−0.221	(0.014)	0.032	(0.007)
F15480-0344	−0.009	(0.025)	0.095	(0.007)
NGC6810	0.034	(0.025)	0.105	(0.023)
NGC6860	0.171	(0.019)	0.054	(0.007)
NGC6890	−0.037	(0.015)	0.018	(0.009)
IC5063	−0.237	(0.014)	−0.014	(0.010)
UGC11680	0.067	(0.038)	0.087	(0.018)
NGC7130	−0.036	(0.028)	−0.001	(0.010)
NGC7172	−1.679	(0.008)	−0.387	(0.012)
NGC7213	0.587	(0.023)	0.236	(0.007)
NGC7314	−0.205	(0.056)	−0.118	(0.018)
M-3-58-7	0.189	(0.027)	0.021	(0.010)
NGC7469	0.068	(0.018)	0.048	(0.010)
NGC7496	−0.091	(0.037)	−0.024	(0.008)
NGC7582	−0.657	(0.026)	−0.156	(0.010)
NGC7590	0.213	(0.085)	0.086	(0.068)
NGC7603	0.205	(0.020)	0.033	(0.015)
NGC7674	−0.098	(0.019)	0.025	(0.012)
CGCG381-051	0.381	(0.018)	0.126	(0.006)

Note. — Sil 10 μm and 18 μm strengths. Sil absorption is indicated by negative strengths, emission, positive. Formal statistical uncertainties are given in parentheses.

Table 12.   Infrared Continuum Spectral Indices

Source ID	$\alpha(20–30\ \mu m)$		$\alpha(55\text{-}90\ \mu m)$	
MRK335	−1.75	(0.03)	−1.49	(0.29)
MRK938	1.58	(0.02)	−2.03	(0.03)
E12-G21	−0.62	(0.02)	−0.59	(0.10)
MRK348	−1.87	(0.01)	−2.62	(0.23)
NGC424	−2.23	(0.02)	−2.60	(0.11)
NGC526A	−2.91	(0.03)	−1.50	(0.44)
NGC513	−0.40	(0.03)	−0.72	(0.06)
F01475-0740	−1.36	(0.03)	−2.23	(0.19)
NGC931	−1.45	(0.02)	−1.61	(0.07)
NGC1056	0.62	(0.03)	−1.08	(0.06)
NGC1097	0.69	(0.01)	−1.05	(0.02)
NGC1125	0.21	(0.03)	−2.08	(0.06)
NGC1143-4	0.62	(0.01)	−0.60	(0.05)
M-2-8-39	−2.36	(0.02)	−2.80	(0.43)
NGC1194	−1.13	(0.02)	−2.82	(0.20)
NGC1241	0.00	(0.03)	−0.47	(0.06)
NGC1320	−1.06	(0.02)	−1.79	(0.06)
NGC1365	0.59	(0.01)	−1.05	(0.03)
NGC1386	−0.45	(0.02)	−1.52	(0.03)
F03450+0055	−1.89	(0.03)	$\cdots$	$\cdots$
NGC1566	−0.50	(0.02)	−0.29	(0.07)
F04385-0828	−0.50	(0.03)	−2.85	(0.07)
NGC1667	0.42	(0.03)	−0.37	(0.06)
E33-G2	−1.96	(0.02)	−1.39	(0.21)
M-5-13-17	−0.98	(0.03)	−1.30	(0.12)
MRK6	−1.72	(0.02)	−1.95	(0.14)
MRK79	−1.32	(0.02)	−1.54	(0.12)
NGC2639	0.04	(0.06)	0.36	(0.07)
MRK704	−2.29	(0.02)	−3.87	(0.38)
NGC2992	−0.73	(0.03)	−1.19	(0.04)
MRK1239	−1.82	(0.02)	−2.45	(0.11)
NGC3079	2.45	(0.04)	$\cdots$	$\cdots$
NGC3227	−0.83	(0.02)	−1.11	(0.04)
NGC3511	0.24	(0.05)	−0.12	(0.06)
NGC3516	−1.35	(0.02)	−1.97	(0.11)
M+0-29-23	0.41	(0.01)	−0.98	(0.04)
NGC3660	0.11	(0.04)	−0.79	(0.15)
NGC3982	−0.02	(0.04)	−0.59	(0.07)
NGC4051	−1.26	(0.03)	−1.16	(0.08)
UGC7064	−0.75	(0.04)	−1.05	(0.12)
NGC4151	−2.14	(0.02)	−2.50	(0.05)
MRK766	−0.81	(0.02)	−2.03	(0.04)
NGC4388	−0.53	(0.03)	−1.29	(0.09)
NGC4501	−0.28	(0.05)	0.34	(0.08)
NGC4579	−0.67	(0.02)	−0.36	(0.08)
NGC4593	−1.11	(0.02)	−1.33	(0.09)

Table 12—Continued

Source ID	α(20–30 μm)		α(55-90 μm)	
NGC4594	−0.74	(0.06)	−0.12	(0.46)
NGC4602	0.04	(0.05)	−0.19	(0.13)
TOL1238-364	−0.90	(0.03)	−1.51	(0.06)
M-2-33-34	−0.72	(0.04)	−1.30	(0.12)
NGC4941	−0.90	(0.03)	−1.33	(0.14)
NGC4968	−1.47	(0.02)	−1.58	(0.10)
NGC5005	1.45	(0.03)	−0.45	(0.04)
NGC5033	0.10	(0.02)	−0.19	(0.18)
NGC5135	0.44	(0.02)	−0.72	(0.06)
M-6-30-15	−1.74	(0.02)	−1.67	(0.16)
NGC5256	0.85	(0.02)	−1.39	(0.04)
IC4329A	−2.14	(0.02)	−2.70	(0.10)
NGC5347	−1.51	(0.04)	−1.67	(0.12)
NGC5506	−0.67	(0.02)	−2.11	(0.05)
NGC5548	−1.65	(0.03)	−1.88	(0.13)
MRK817	−0.80	(0.02)	−2.51	(0.08)
NGC5929	0.45	(0.07)	−1.26	(0.09)
NGC5953	0.51	(0.03)	$\cdots$	$\cdots$
M-2-40-4	−0.77	(0.01)	−1.28	(0.05)
F15480-0344	−1.21	(0.02)	−1.82	(0.10)
NGC6810	−0.42	(0.02)	−1.07	(0.03)
NGC6860	−2.06	(0.02)	−0.61	(0.13)
NGC6890	−0.66	(0.02)	−0.66	(0.05)
IC5063	−1.01	(0.02)	−2.70	(0.06)
UGC11680	−1.39	(0.03)	−0.59	(0.27)
NGC7130	0.44	(0.02)	−1.24	(0.03)
NGC7172	0.40	(0.02)	−0.65	(0.04)
NGC7213	−2.30	(0.03)	−0.76	(0.10)
NGC7314	−0.77	(0.02)	−0.82	(0.13)
M-3-58-7	−0.87	(0.02)	−1.69	(0.05)
NGC7469	−0.11	(0.01)	−1.55	(0.03)
NGC7496	0.47	(0.02)	−1.57	(0.04)
NGC7582	0.71	(0.02)	−1.38	(0.03)
NGC7590	0.10	(0.03)	−0.34	(0.06)
NGC7603	−1.75	(0.02)	−1.01	(0.16)
NGC7674	−0.94	(0.02)	−1.66	(0.04)
CGCG381-051	−0.77	(0.02)	−1.69	(0.08)

Note. — Continuum spectral indices over the wavelength ranges 20–30 μm and 55-90 μm. Formal statistical uncertainties are provided in parentheses. The convention is $F_\lambda \propto \lambda^\alpha$.
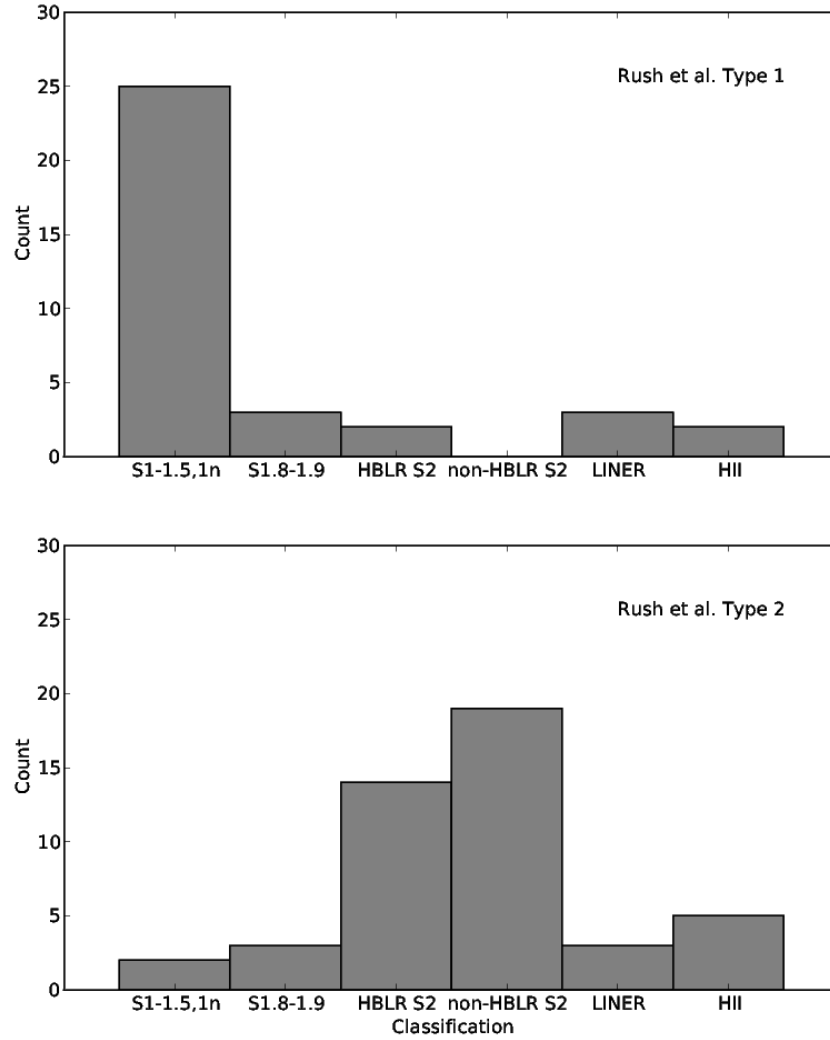
Fig. 1.— A comparison of AGN classifications from Rush et al. (1993) and our revised classifications collected from the literature, Table 1. The top panel illustrates the re-classification of Rush et al. Type 1 AGNs, and the bottom panel similarly shows the re-classification of Type 2 AGNs. Seyfert 2s are split into two groups: (1) HBLR S2s, which are known to harbor an HBLR, and (2) non-HBLR S2s, in which no HBLR has yet been detected.
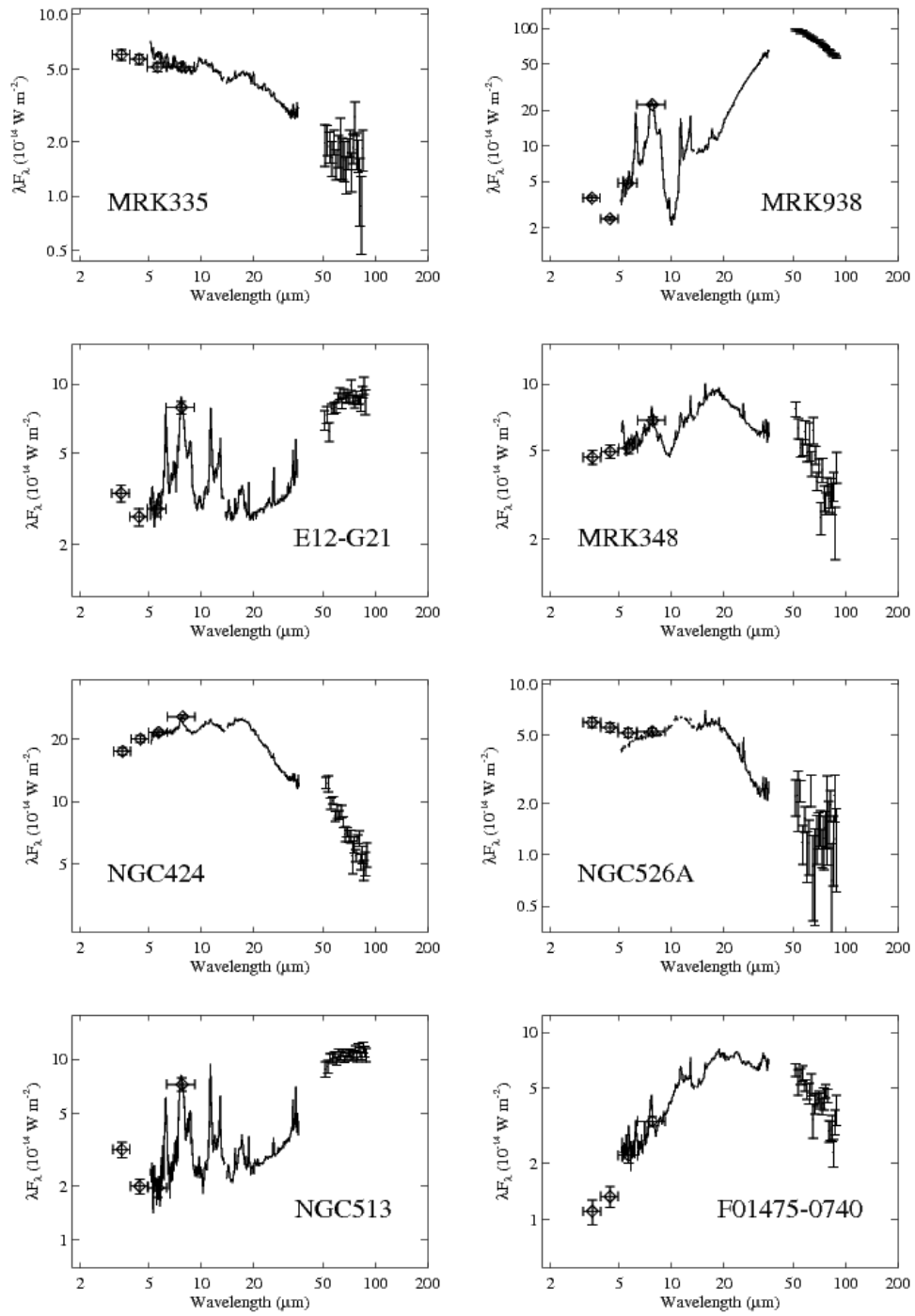
Figure 2
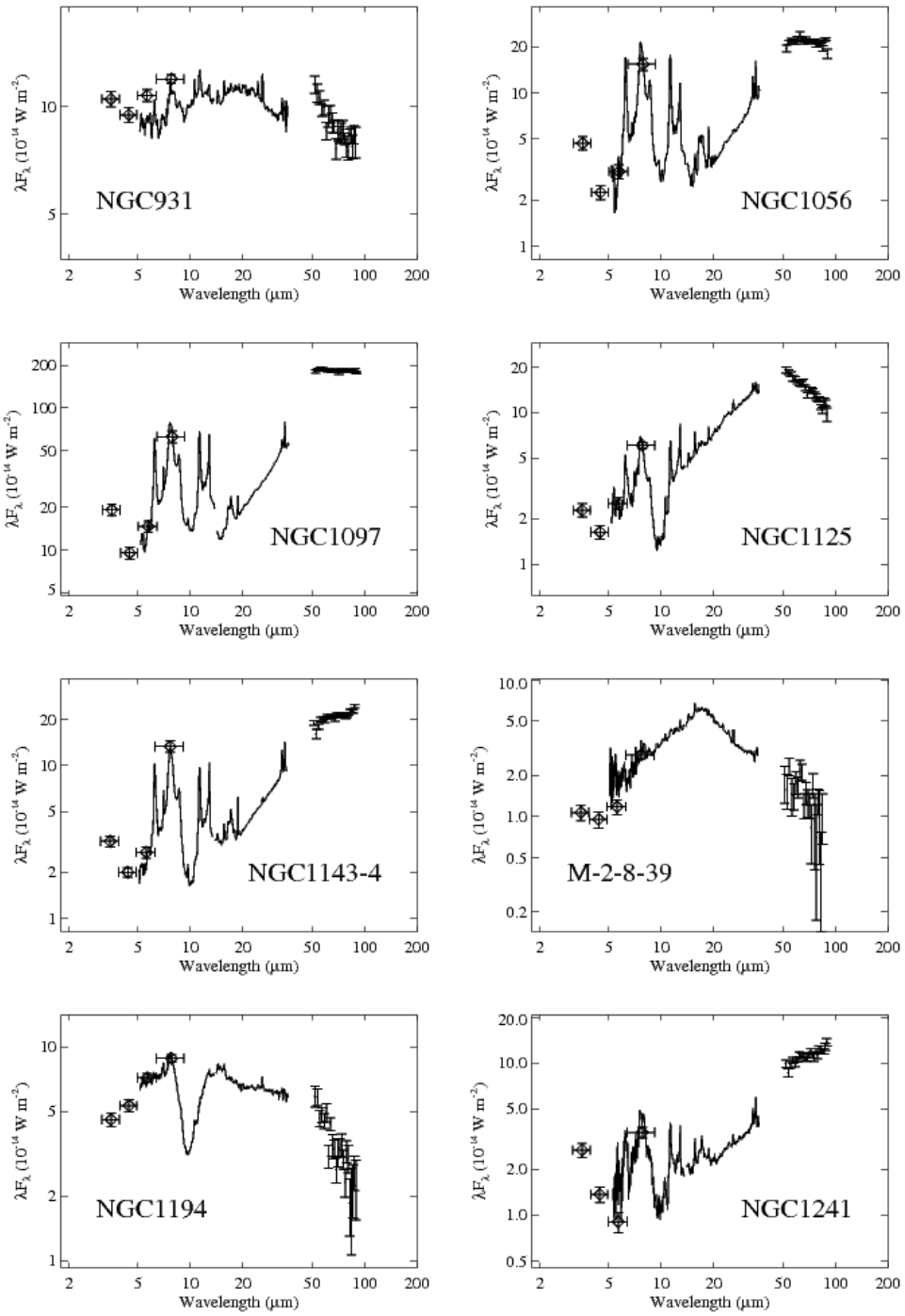
Figure 2
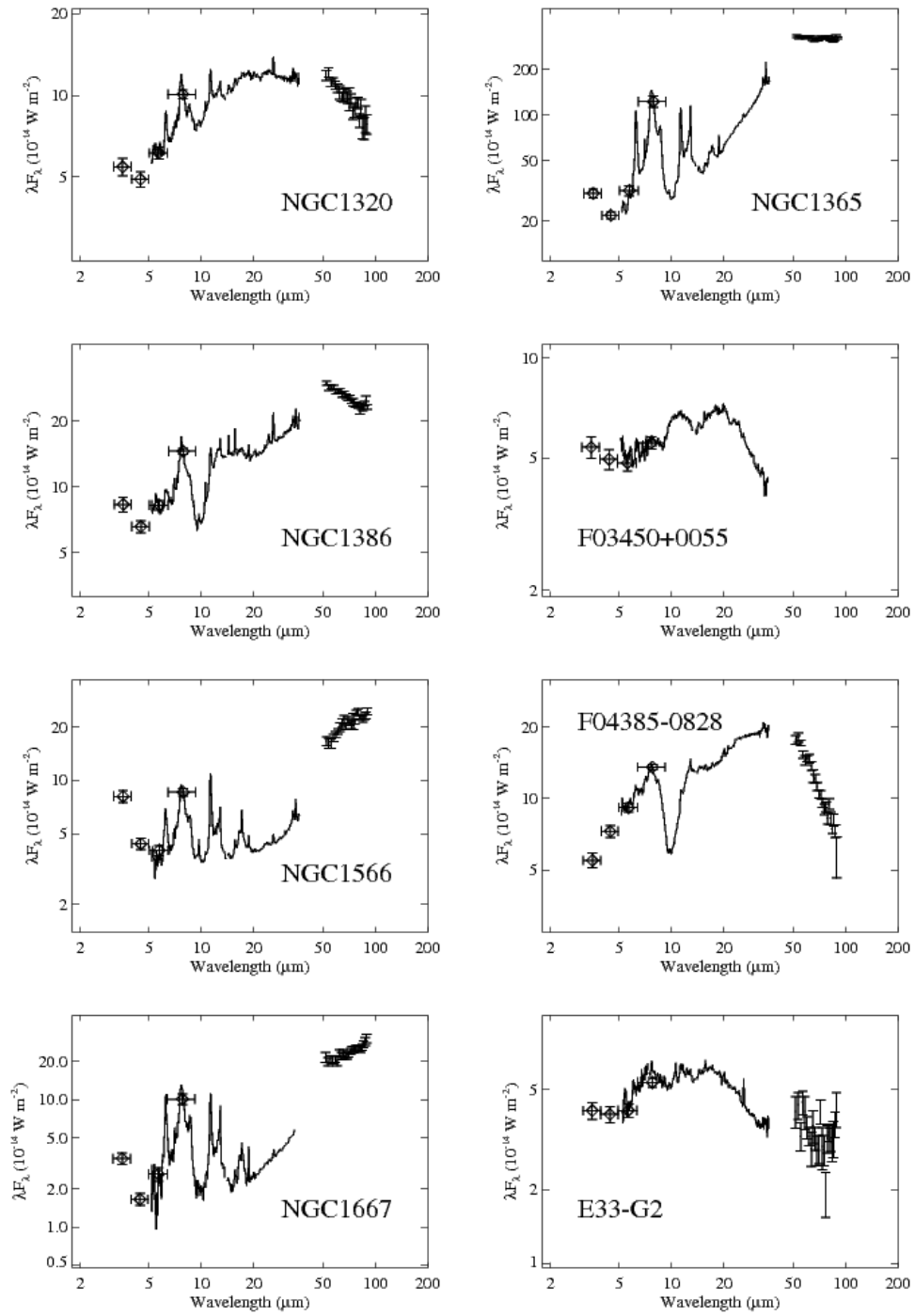
Figure 2
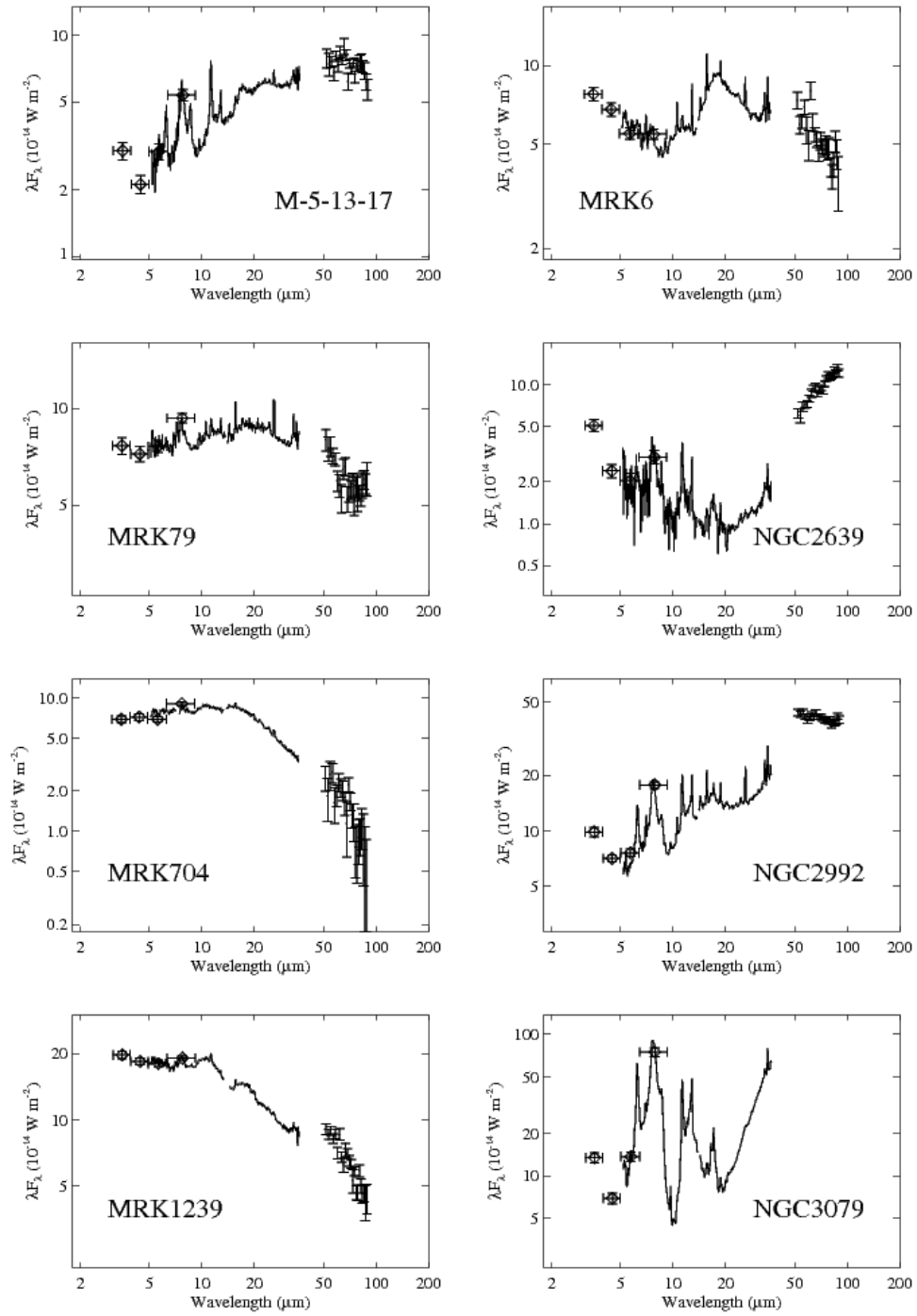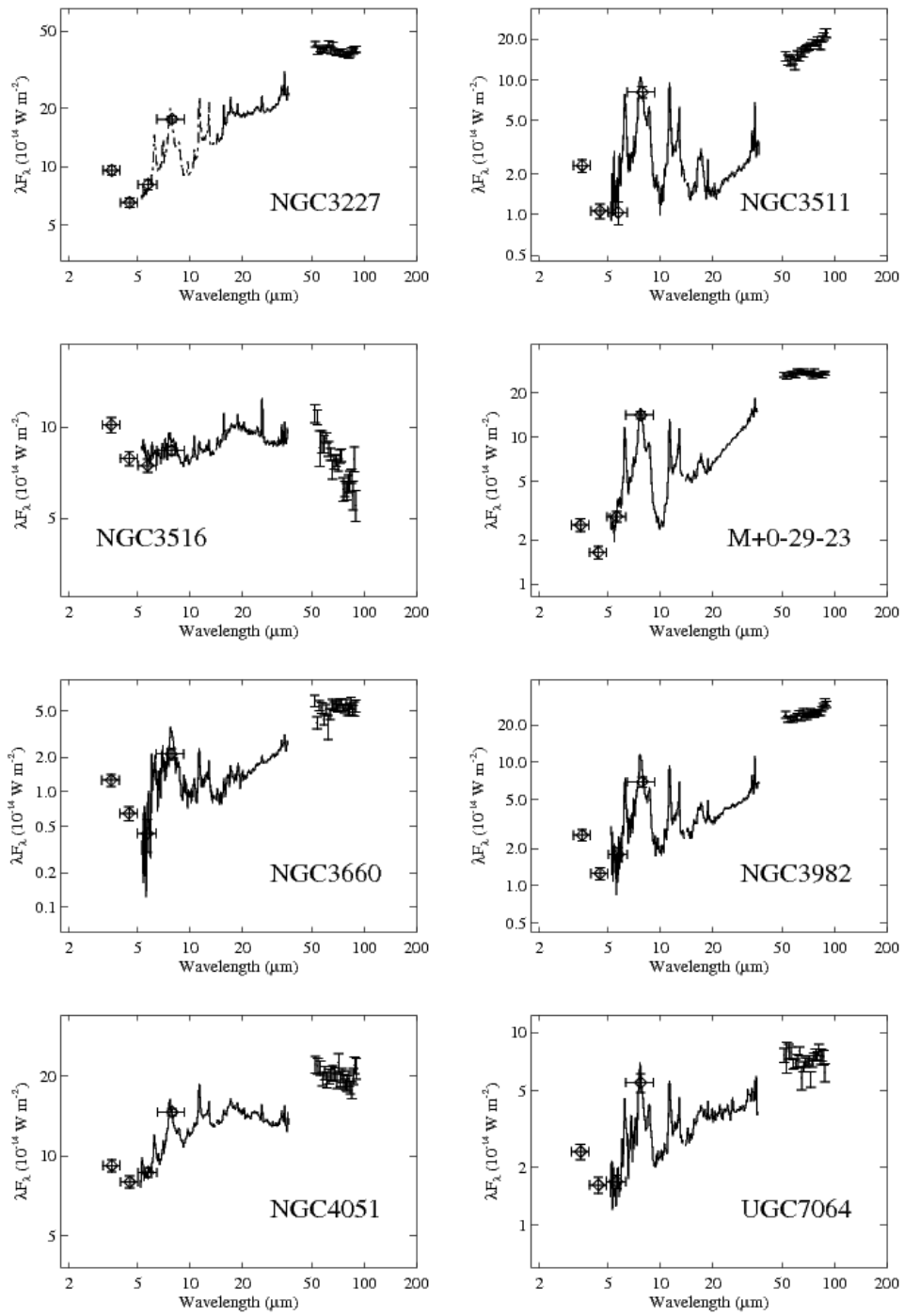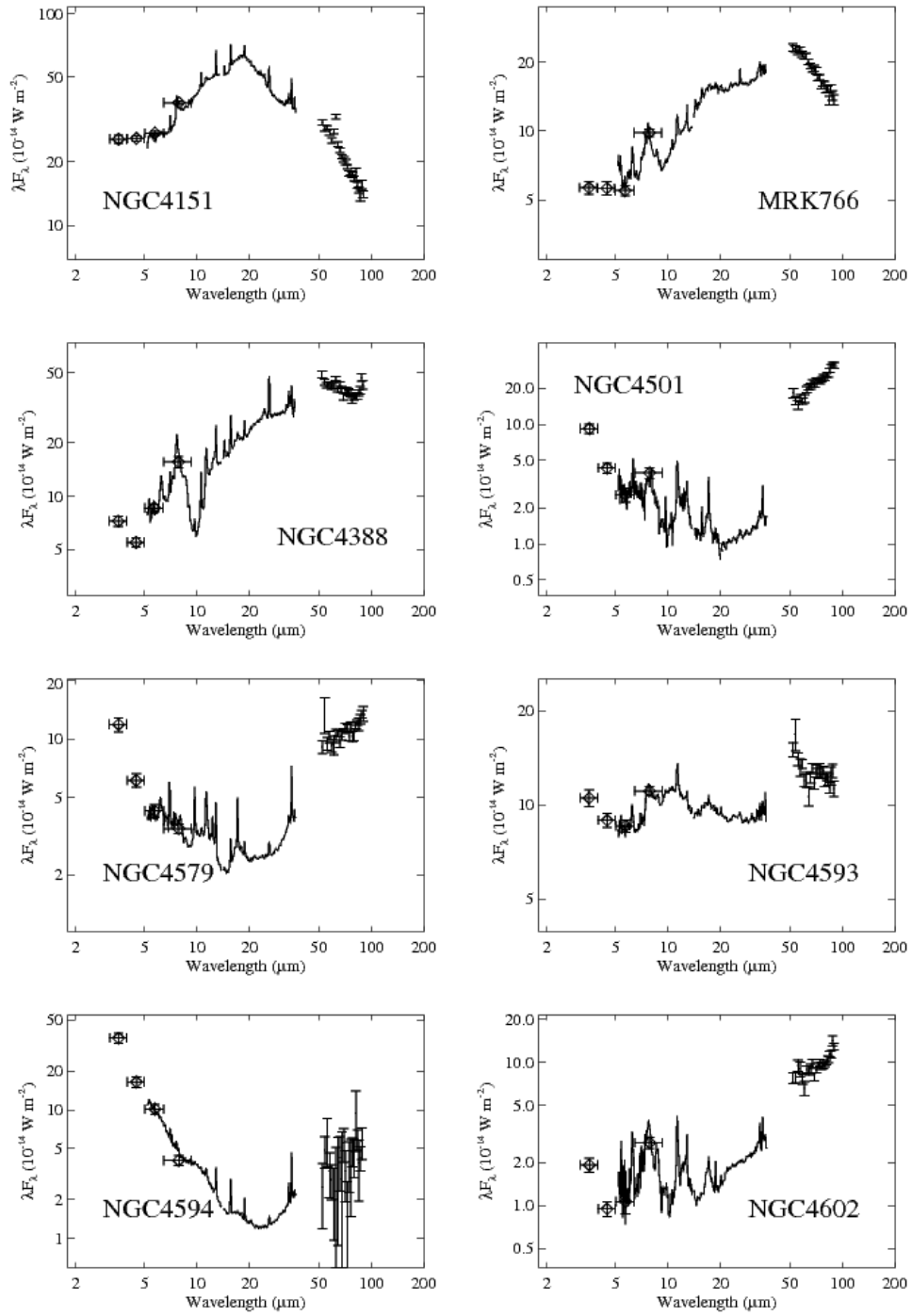
Figure 2
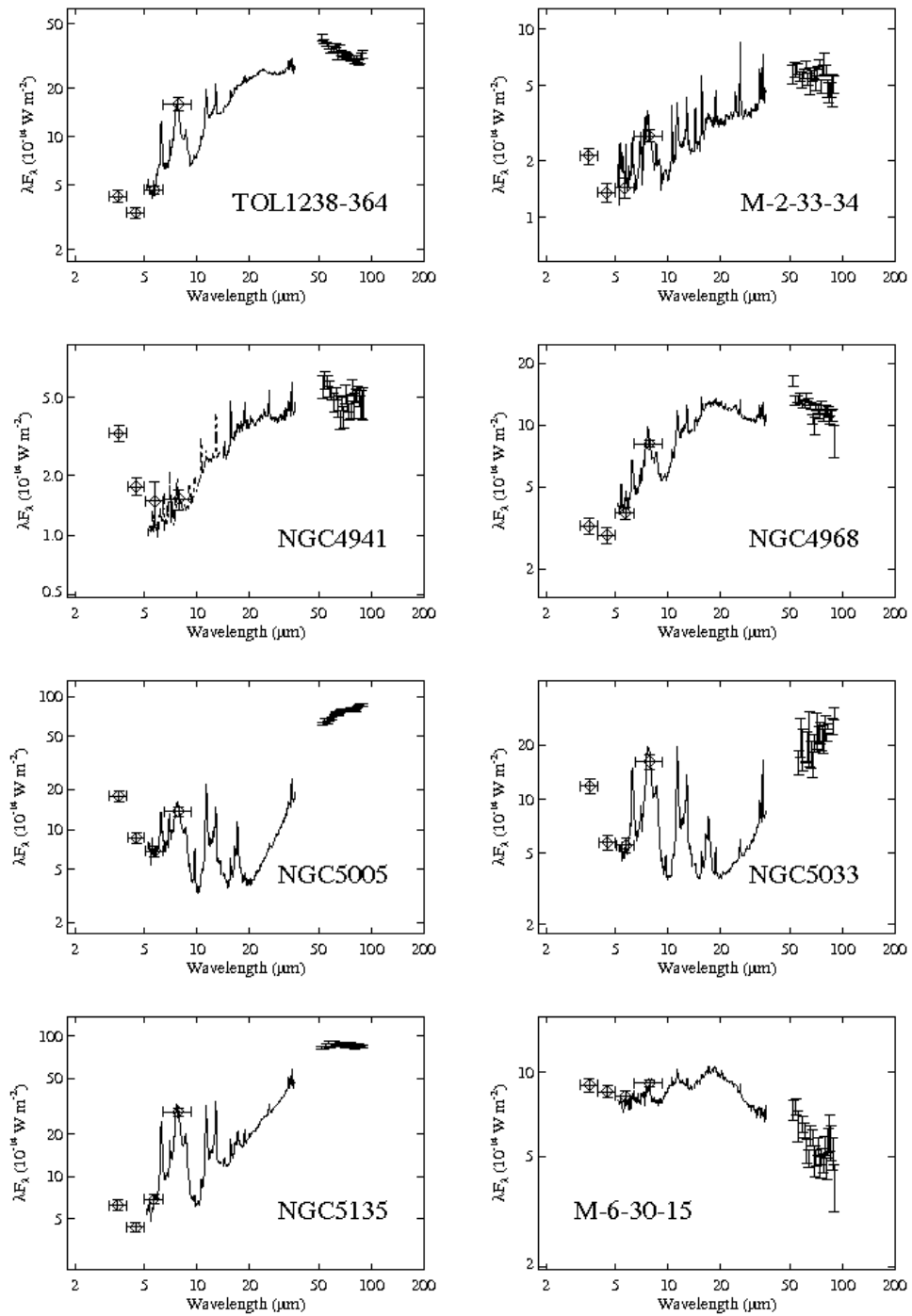
Figure 2
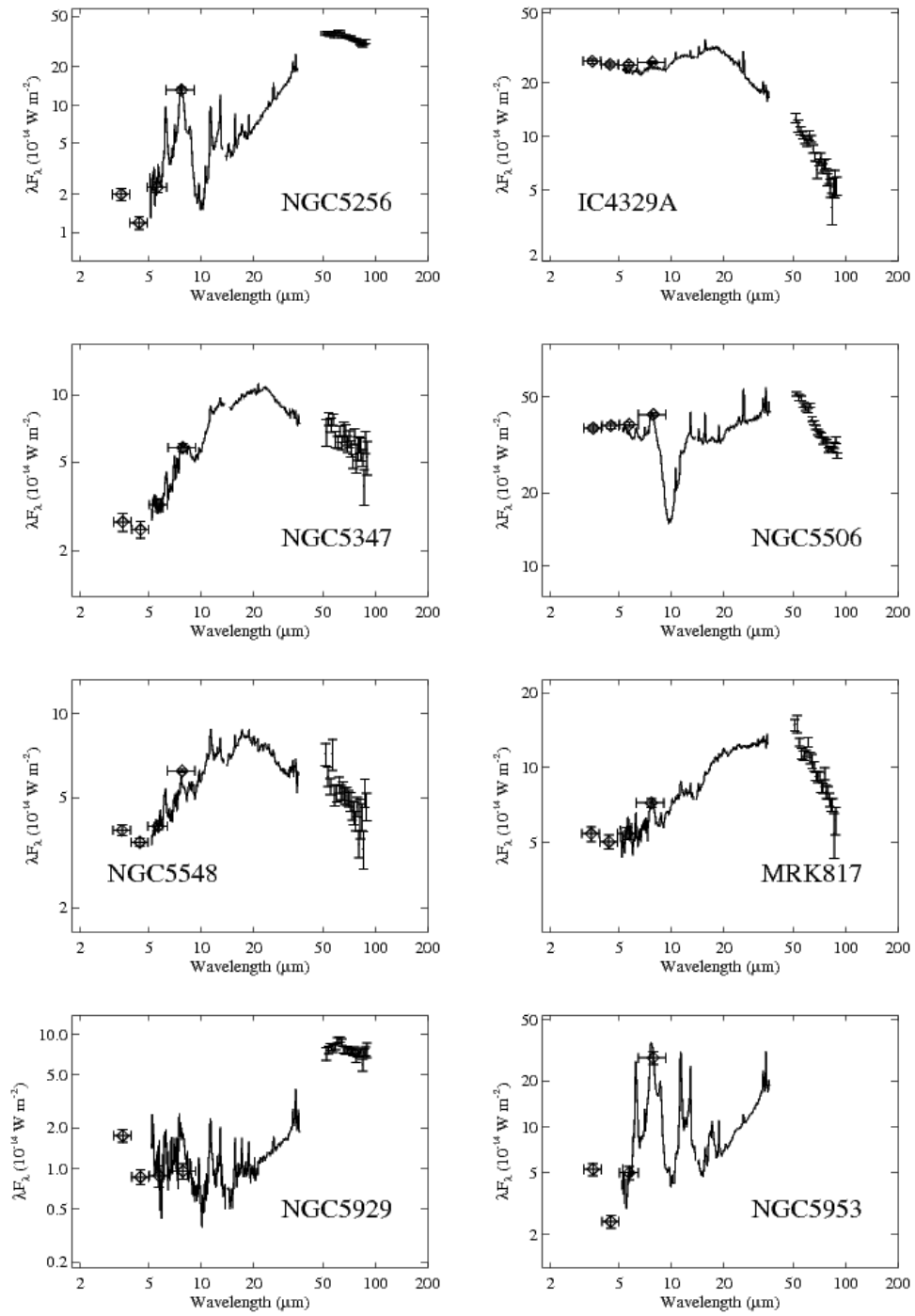
Figure 2
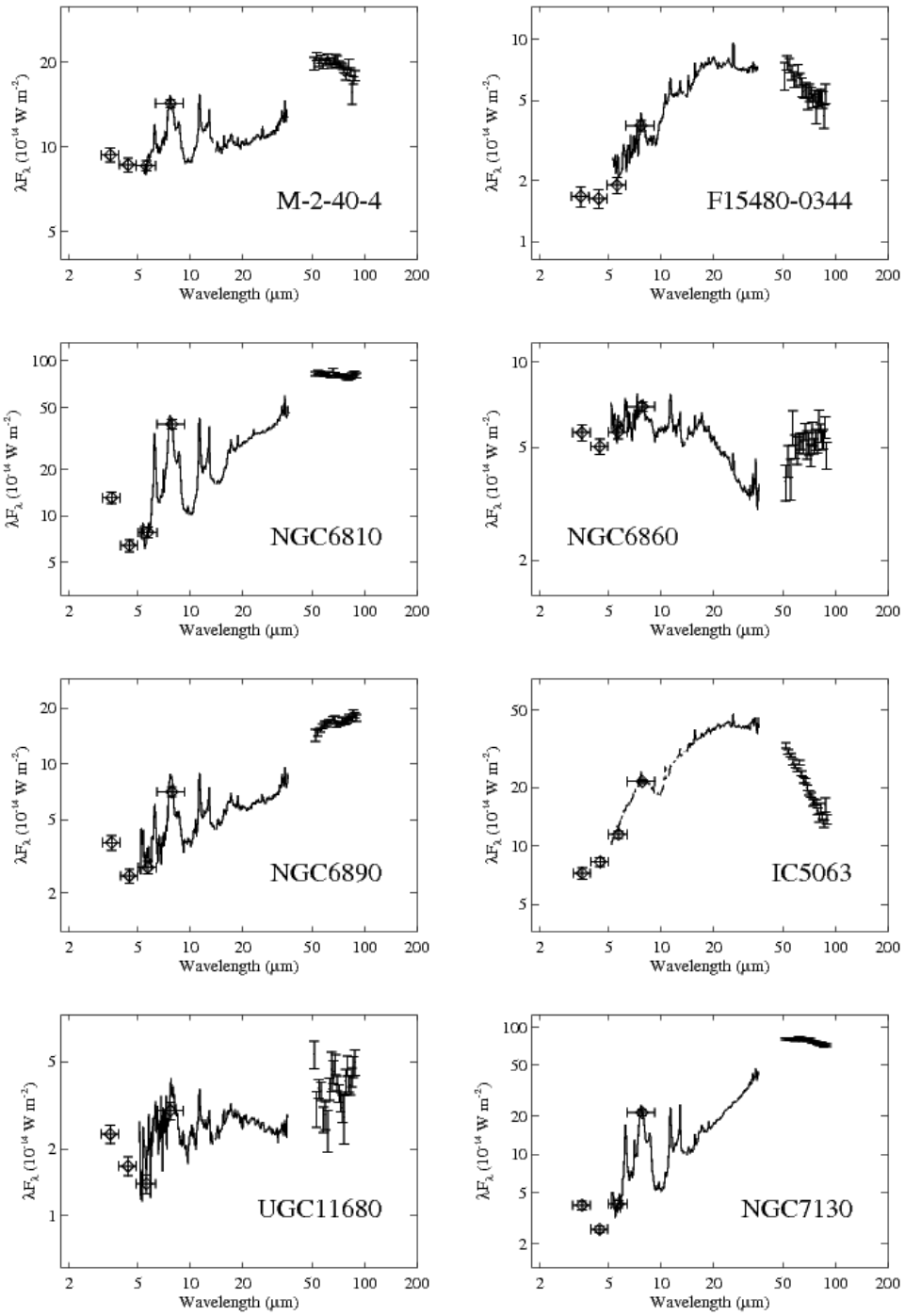
Figure 2
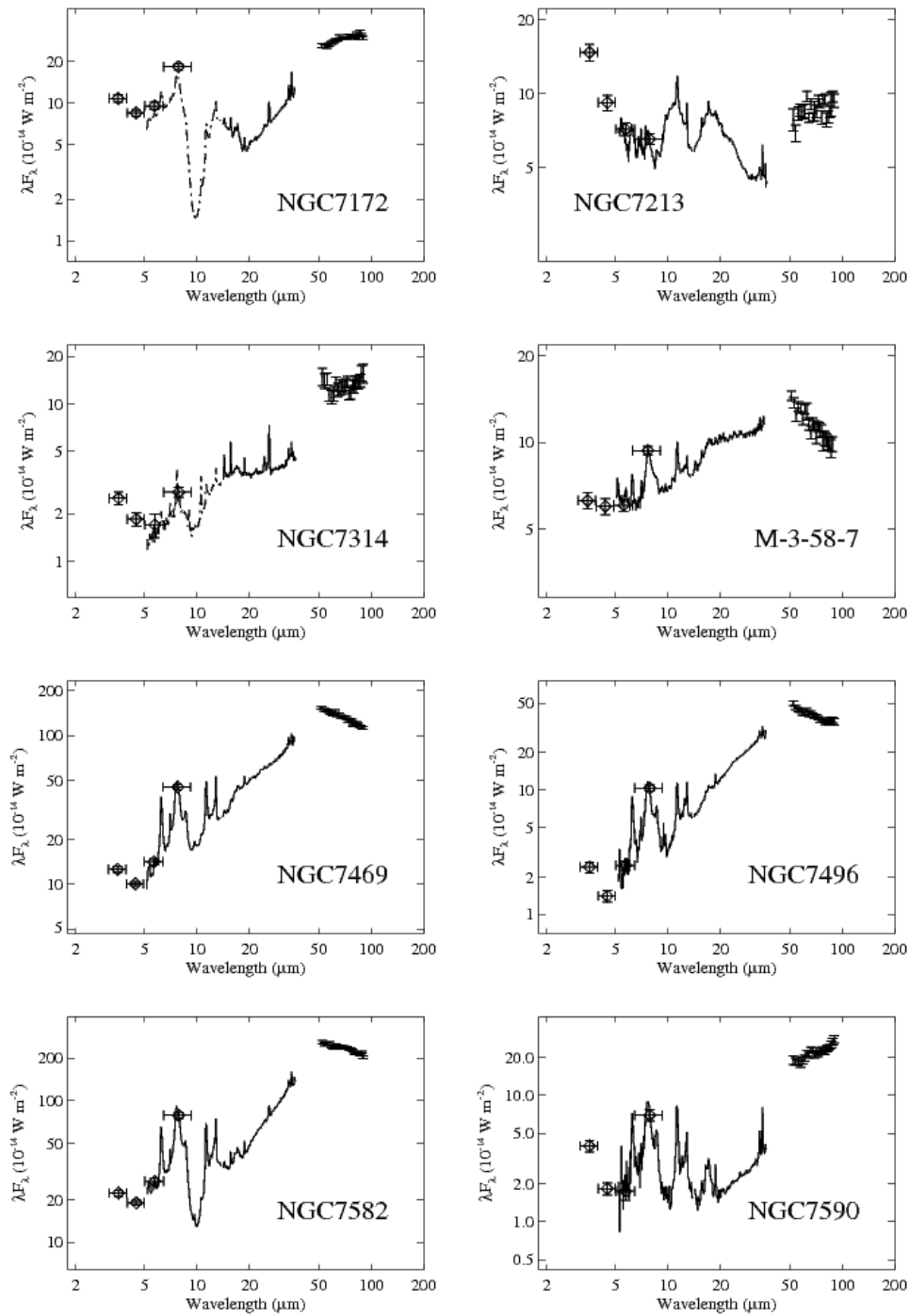
Figure 2

Figure 2

Figure 2
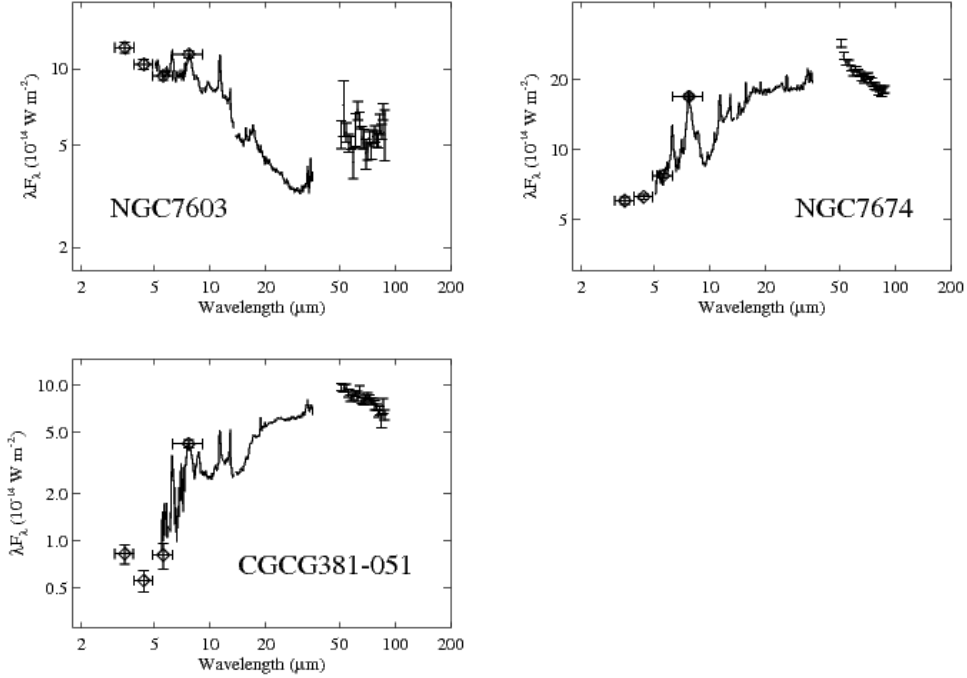
Fig. 2.— *Spitzer* spectrophotometry of the 12 μm AGN sample. The SEDs are plotted as λF_λ vs. rest λ and in order of increasing RA. IRAC data are plotted as diamonds with horizontal errorbars representing the camera bandwidth and vertical errorbars indicating a combination of statistical uncertainties, uncertainty of the extended flux correction, and uncertainty of the color corrections. IRS data are traced by the solid line; each camera and order is plotted independently, hence there are gaps appearing around 15 μm, which separates the SL and LL spectrographs. Scaled, staring-mode IRS data are indicated by dash-dot lines. MIPS SED data are show as vertical error bars, which represent statistical uncertainties of the MIPS-SED photometry, but do not include the systematic 10-15% uncertainty associated with the flux calibration. The IRAC and IRS data were extracted from 20″ diameter synthetic apertures, and the MIPS-SED data were extracted from 30″ aperture along a 20″ wide slit.
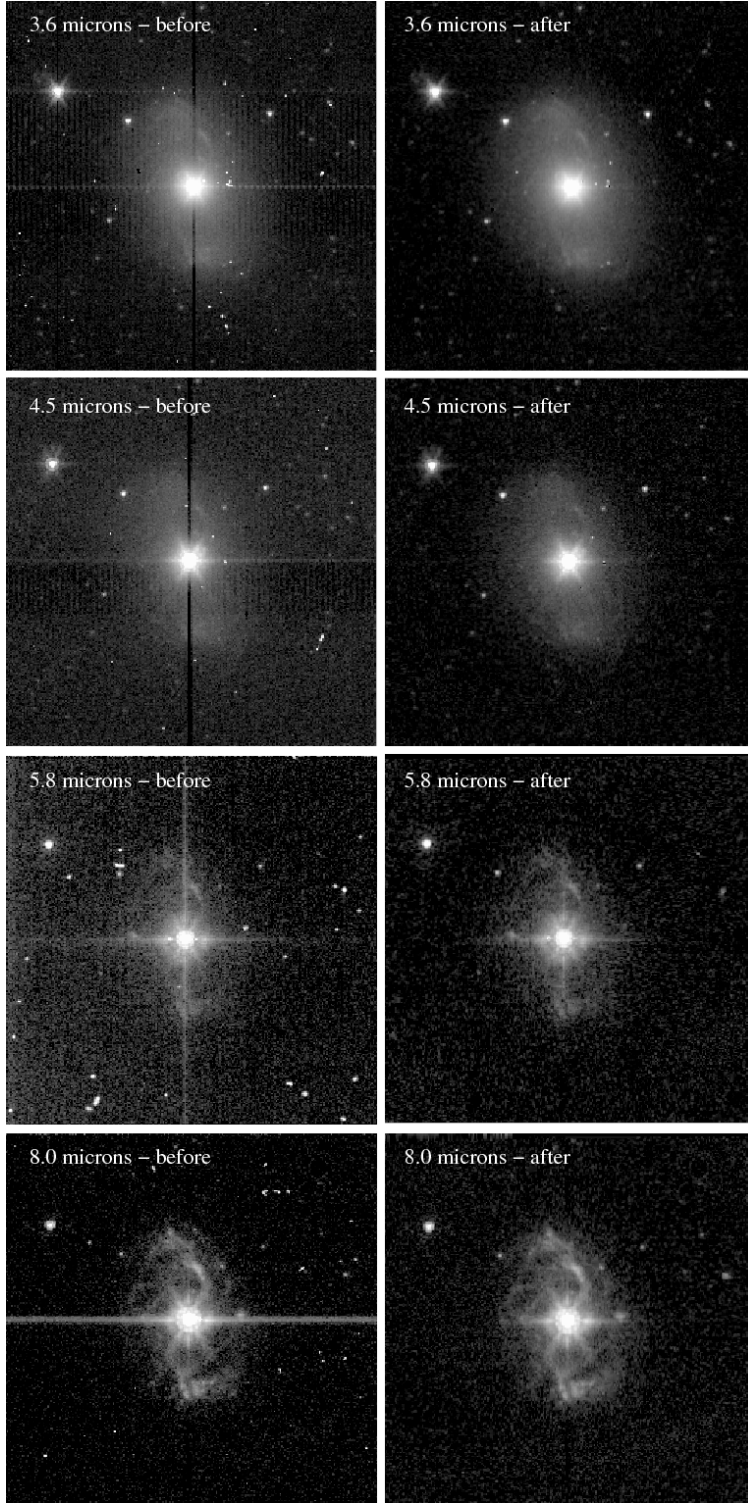
Fig. 3.— IRAC images of NGC 4151, shown to illustrate the results of our post-BCD artifact removal technique. Each row corresponds to a single IRAC detector, stacked in order of increasing wavelength. The left column shows the S14.0 pipeline image, and the right column shows the matching image after artifact removal. The images are displayed with a log stretch from 0 to 1 MJy sr^{-1} for the 3.6 μm and 4.5 μm images and 0 to 20 MJy sr^{-1} for the 5.8 and 8.0 μm images, where zero surface brightness has been adjusted roughly to the image background.
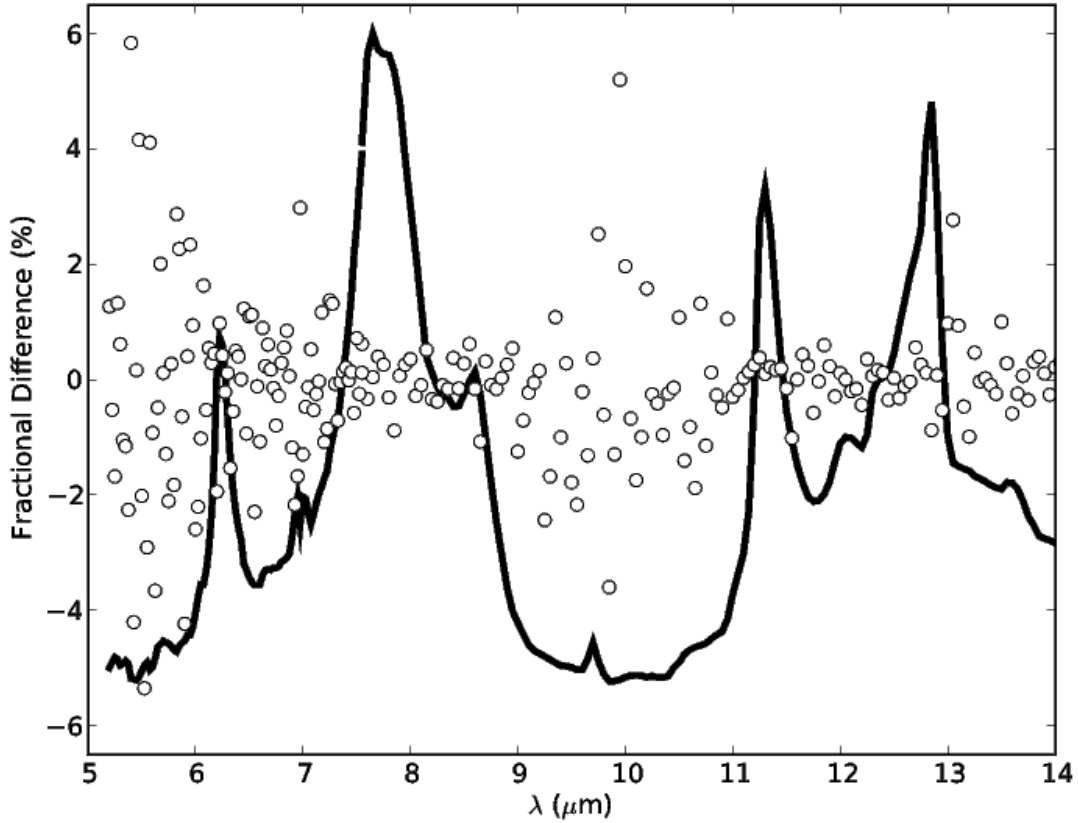
Fig. 4.— An illustration of IRS optimal spectral extraction for NGC 3079. The wavelength axis is in the observed frame. The fractional differences between the optimally-weighted and non-weighted spectra, calculated as a fraction of the optimally-weighted spectrum, are plotted as open circles. The optimally-extracted spectrum, F_ν, has been scaled to fit the plotting range and is shown as a thick line. Even though this is an extended source and further shows extended, strong PAH features, optimal weighting has preserved the shape and strength of the PAH 6.2 μm feature. The relative differences typically fall in the range 2–4%, comparable to the statistical uncertainties of the non-weighted extraction. In this high signal-to-noise case, optimum extraction reduced the statistical uncertainties by $\sim 60\%$.
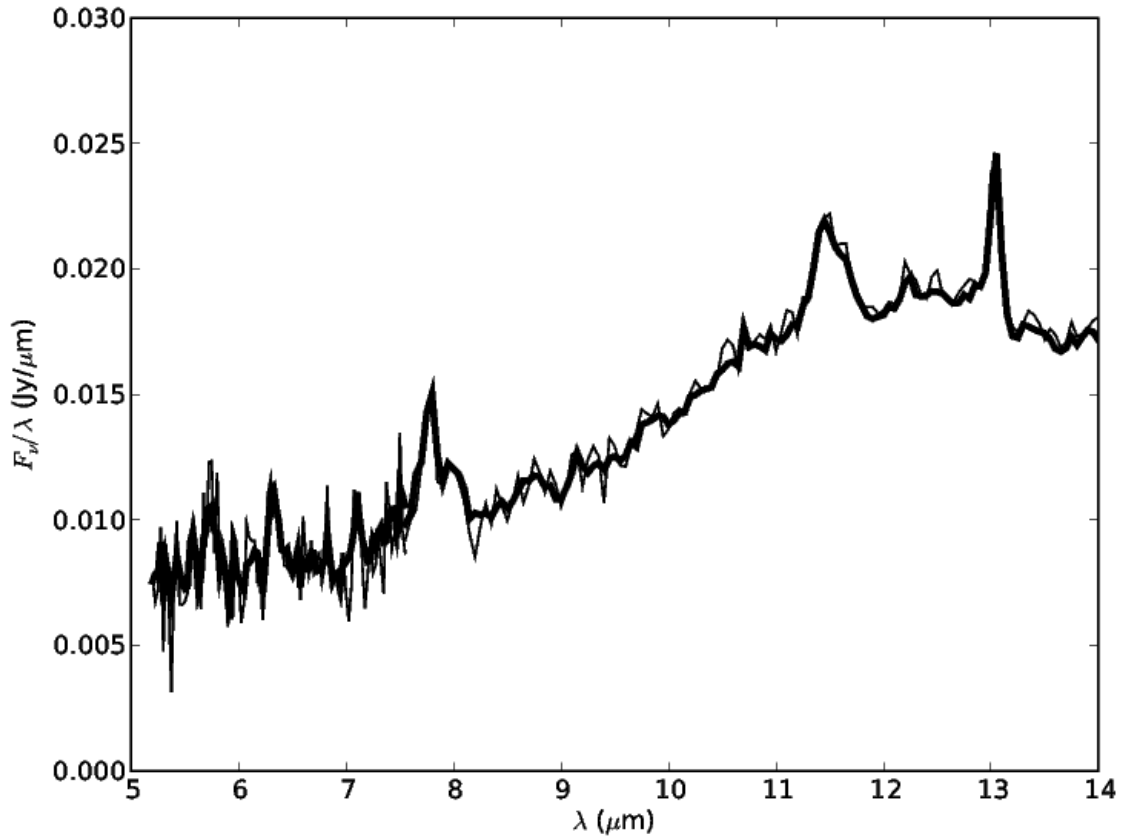
Fig. 5.— An illustration of IRS optimal spectral extraction. The IRS short-low spectrum of F01475-0740 is shown. The wavelength axis is in the observed frame. The optimally-weighted spectrum is plotted as a thick line, and non-weighted spectrum as a thin line. Notice that the continuum and PAH features retain their shape with optimal weighting; however, the formal statistical uncertainties are reduced by a factor of 2–3 over the SL spectral range.
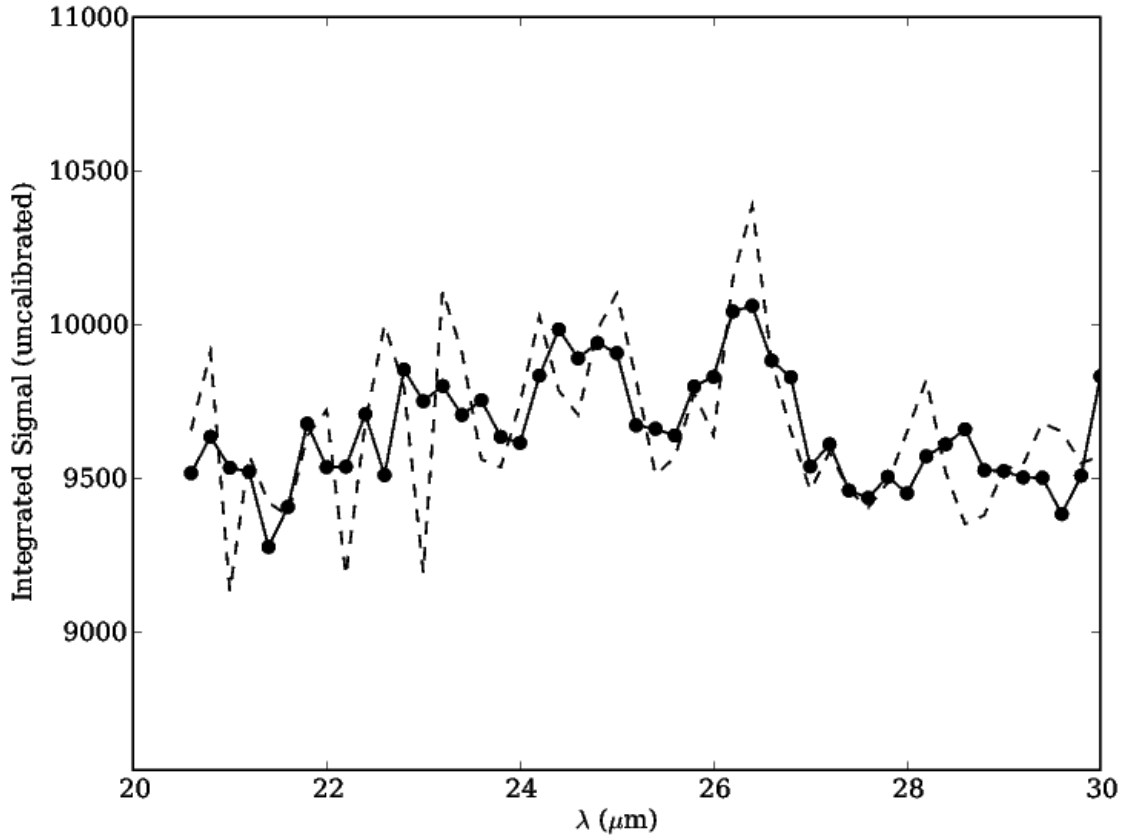
Fig. 6.— An illustration of spectral fringe reduction. Shown is the extracted spectrum of MRK 1239, both with (filled circles connected by solid-lines) and without (dashed-line) fringe reduction. Wavelengths are in the observed frame. The data shown here are not yet flux-calibrated, as fringe mitigation is performed prior to flux calibration in our processing. Note that the fringes were fit to wavelength ranges avoiding spectral lines; the apparent [O IV] $\lambda26$ μm line in the uncorrected data is spurious.
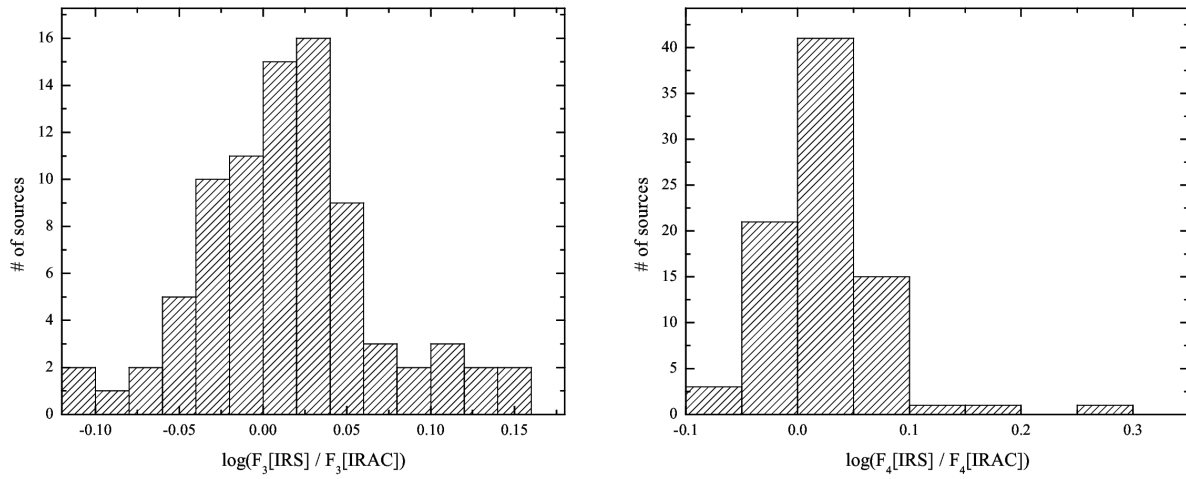
Fig. 7.— Frequency distribution of the flux density ratio $F_\nu(\mathrm{IRS})/F_\nu(\mathrm{IRAC})$ at the overlap wavelengths 5.8 μm (IRAC channel 3 = 5.731 μm) and 8.0 μm (IRAC channel 4 = 7.872 μm).
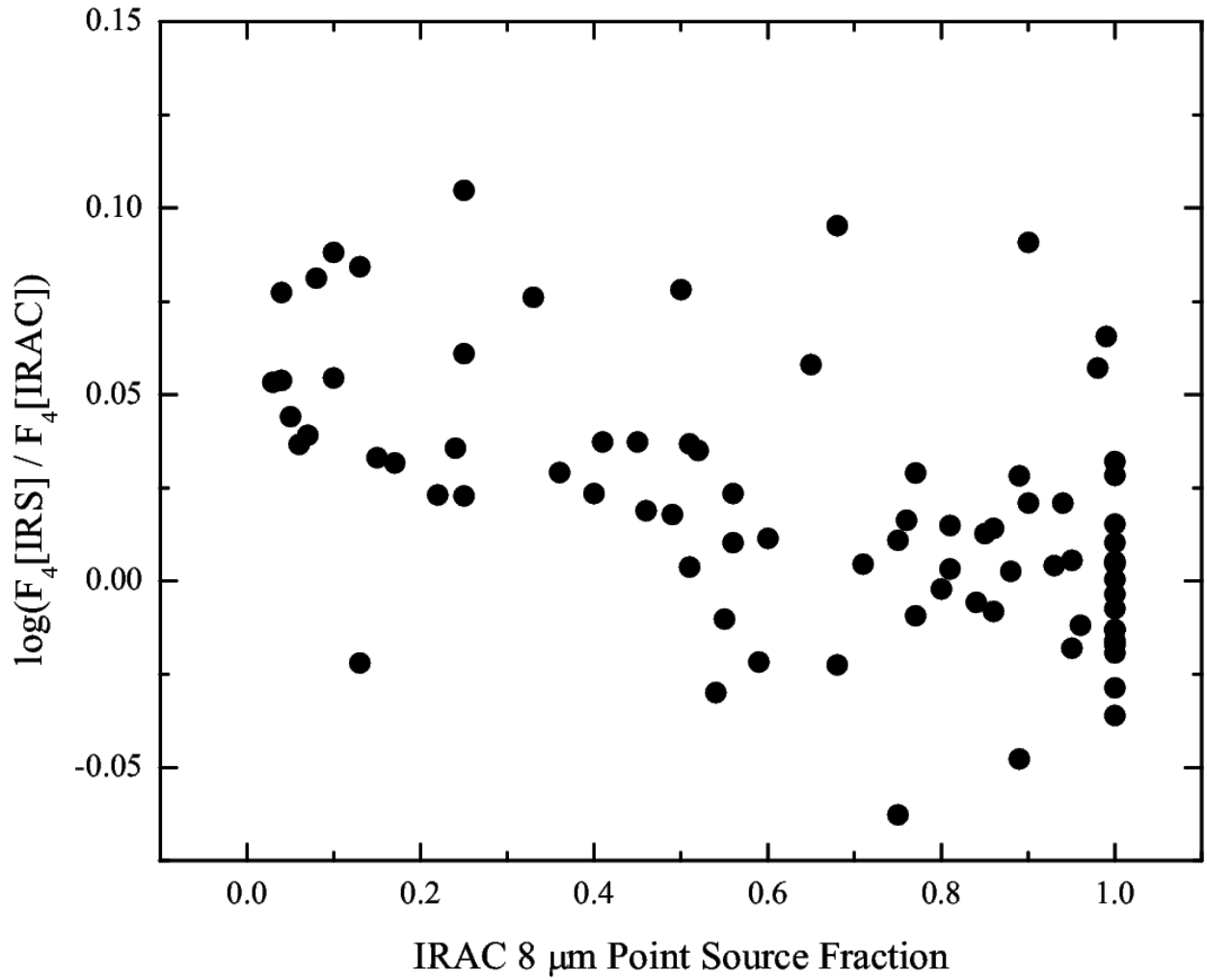
Fig. 8.— IRS / IRAC 8 μm flux ratio vs. IRAC point source fraction. The point source fraction is the ratio of the point source flux determined by wavelet convolution to the total flux in the 20″ synthetic aperture. Here, the subscript "4" refers to IRAC channel 4 = 8 μm.
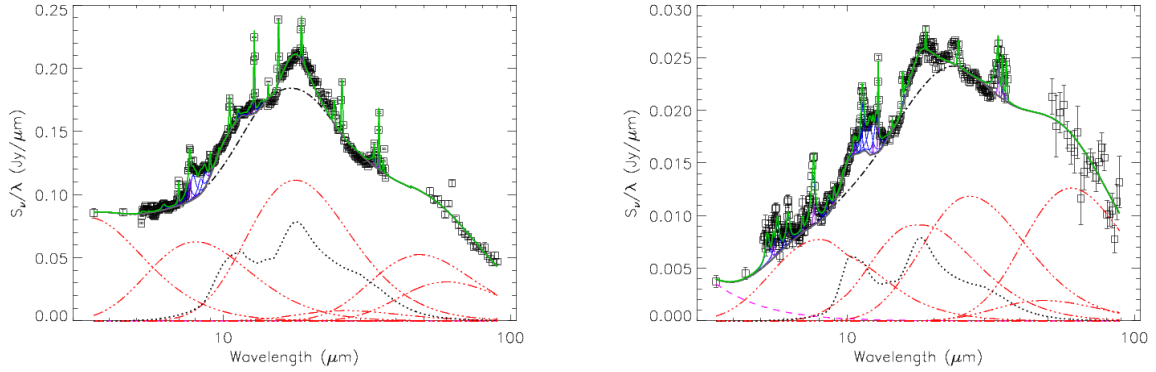
Fig. 9.— Example spectrum decomposition for NGC 4151 (left) and NGC 7213 (right). The vertical axis is in νF_ν units. The measurements are represented by square symbols; the uncertainties are plotted as vertical error-bars and are usually smaller than the symbol size. Continuous lines represent the best fit model (green), underlying dust continuum (gray), and individual PAH features (blue) and emission lines (purple). The broken lines mark the following components: stars (pink dashed), dust continuum (red dash-dot-dot-dot), and optically-thin, warm dust emission (black dotted). The baseline used for Sil index measurements (stars + dust continuum + warm, thin dust continuum) is shown as the black dash-dot-dash line.
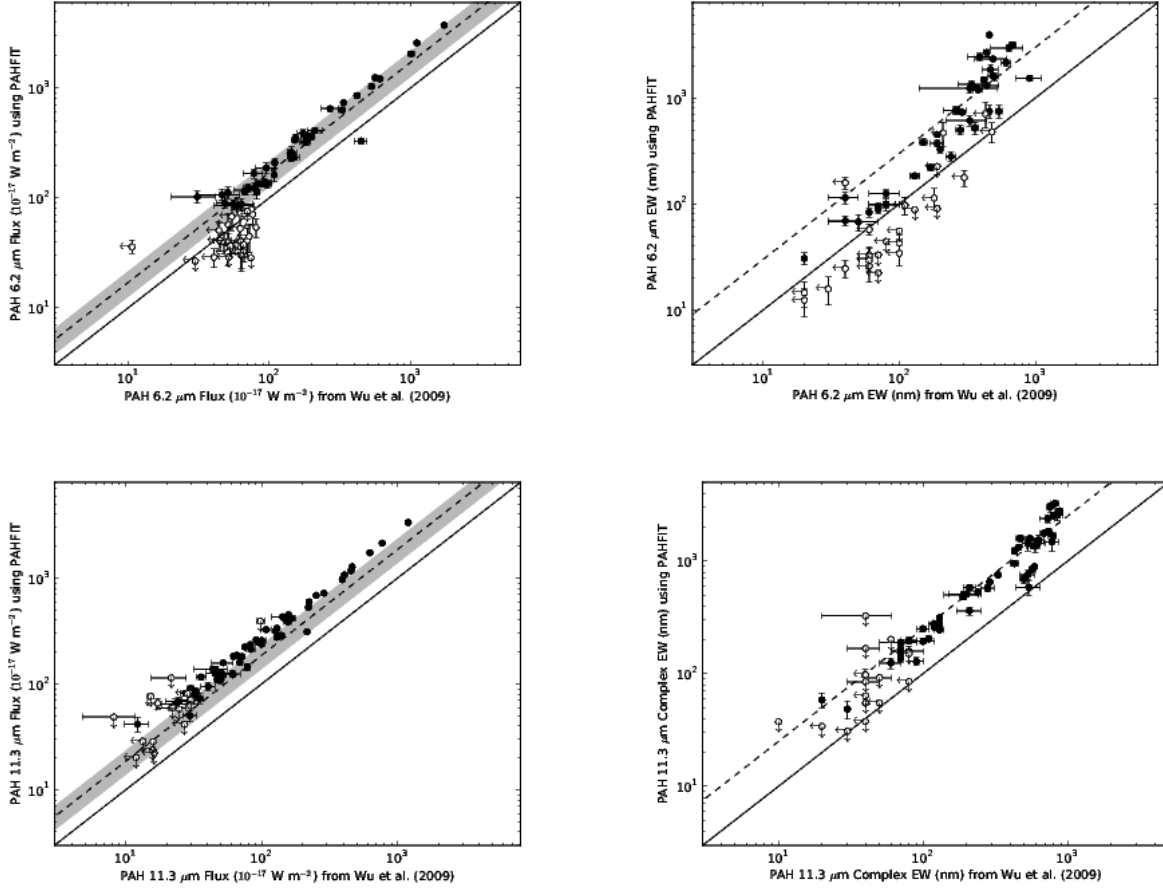
Fig. 10.— Comparison of the PAHFIT spectrum decomposition analysis (*y*-axis on these plots) and the local continuum analysis of Wu et al. (2009) (*x*-axis on these plots). Only data with nearly matching apertures are included in these plots. The individual comparisons are *top left*: PAH 6.2 μm flux, *top right*: PAH 6.2 μm eqw, *bottom left*: flux of the PAH 11.3 μm which includes the 11.22 μm and 11.33 μm PAH features, and *bottom right*: PAH 11.3 μm complex eqw. Data that include upper limits are indicated by open circles, and detections are marked by filled circles. The solid line indicates loci of equivalent measurements. On the flux-flux diagrams, shaded regions bisected by a dashed line mark the average ratio and $\pm 1\,\sigma$ range reported by Smith et al. (2007b) for galaxies in the SINGS sample. On the eqw diagrams, the dashed line illustrates a factor of 3 (6.2 μm) or 2.5 (11.3 μm) enhancement for PAHFIT compared to the spline technique; this line is purely for illustration and is not based on a fit to the data. Notice that the PAHFIT-derived fluxes and eqws are, on average, systematically higher, because PAHFIT removes the contamination of neighboring, weak PAH features.
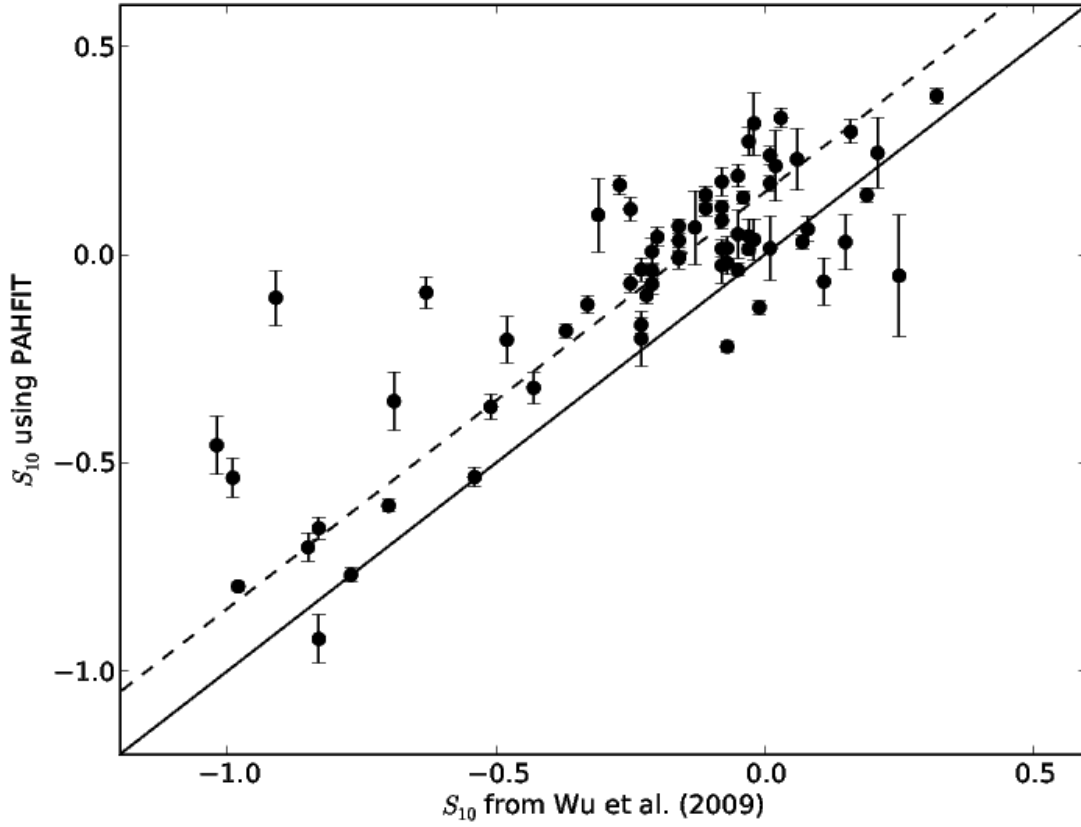
Fig. 11.— Comparison of Sil 10 μm feature strengths based on the PAHFIT spectrum decomposition analysis (y-axis) and the spline continuum approximation (y-axis) used by Wu et al. (2009). The solid line indicates loci of equivalent measurements, and the dashed line illustrates a 0.15 dex enhancement of Sil strengths measured by PAHFIT compared to the spline technique; this line is purely for illustration and is not based on a fit to the data.
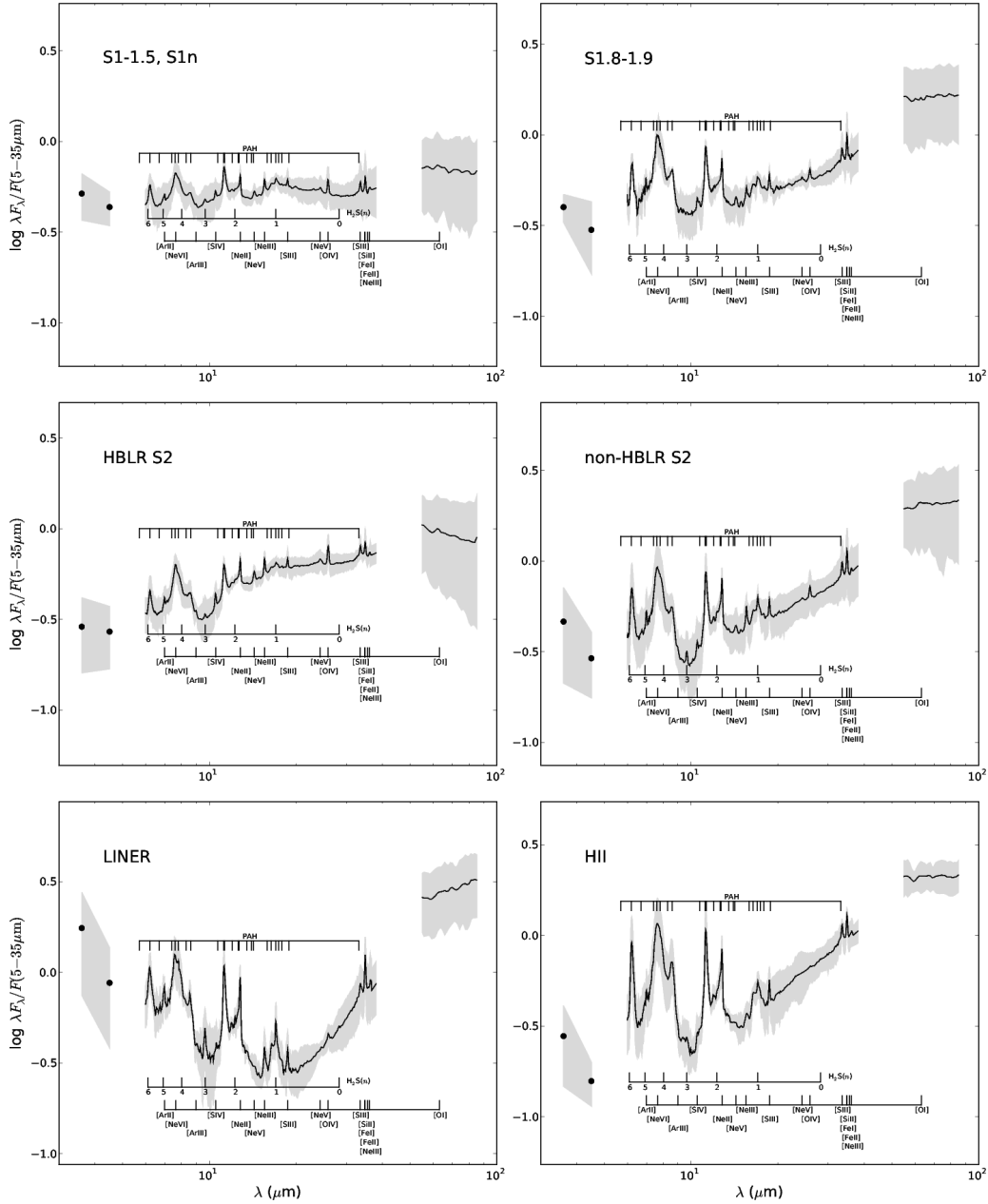
Fig. 12.— SEDs averaged by optical classification. All SEDs were normalized to $F(5\text{–}35\mu m)$ prior to averaging. The gray filled regions indicate the median absolute deviation among objects within that classification bin. PAH, H_2, and fine-structure lines included in the PAHFIT spectral decomposition are annotated.
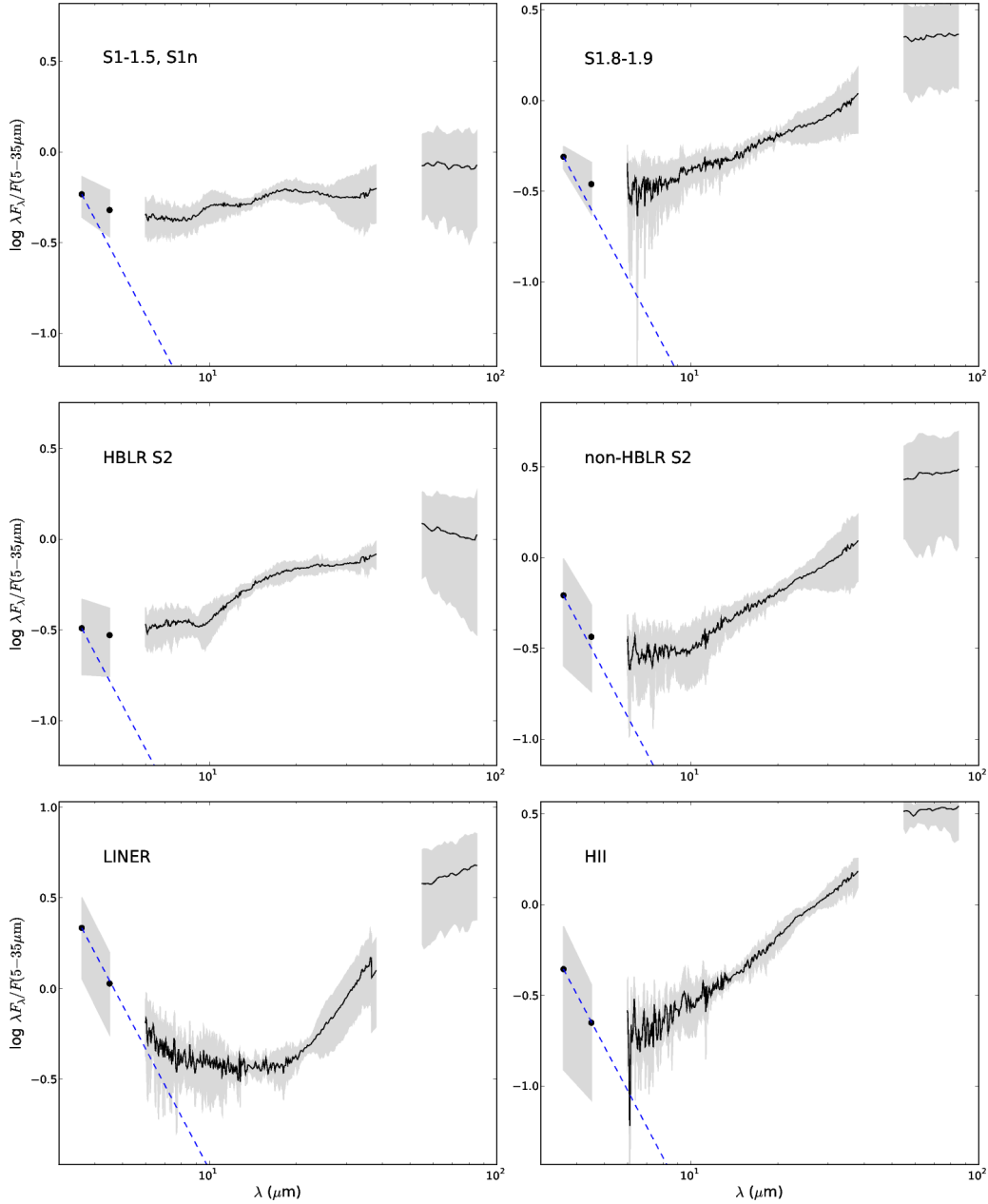
Fig. 13.— PAH, H$_2$, and fine-structure line-subtracted SEDs averaged by optical classification. All SEDs were normalized to $F(5$–35μm) prior to averaging. The gray filled regions indicate the median absolute deviation among objects within that classification bin. The dashed lines trace a Rayleigh-Jeans continuum spectrum, representing an approximate spectrum for stellar photospheres, anchored to 3.6 μm. Sil features appear in emission for the S1-1.5 & S1n class but in absorption in the averaged SEDs both the HBLR S2s (S1h and S1i) and of non-HBLR S2s (S2s where a HBLR has not yet been detected).